MULTI-NODE POWER SYSTEMS PROFILING WITH MODIFIED STATE ESTIMATION

by

David G. Loucks

BSEE, University of Kentucky, 1979

MSEE, University of Pittsburgh, 2002

Submitted to the Graduate Faculty of

the Swanson School of Engineering in partial fulfillment

of the requirements for the degree of

Doctor of Philosophy

University of Pittsburgh

2015

UNIVERSITY OF PITTSBURGH

SWANSON SCHOOL OF ENGINEERING

This dissertation was presented

by

David G. Loucks

It was defended on

November 24, 2015

and approved by

Gregory Reed, Ph.D., Professor, Department of Electrical and Computer Engineering

Zhi-Hong Mao, Ph.D., Associate Professor, Department of Electrical and Computer Engineering

Amro El-Jaroudi, Ph.D., Associate Professor

Department of Electrical and Computer Engineering

Thomas McDermott, Ph.D., Assistant Professor

Department of Electrical and Computer Engineering

David Tipper, Ph.D., Chair, Telecommunications and Networking Program & Associate

Professor, School of Information Sciences

Dissertation Director: Gregory Reed, Ph.D., Professor, Department of Electrical and Computer

Engineering

MULTI-NODE POWER SYSTEMS PROFILING WITH MODIFIED STATE ESTIMATION

David G. Loucks , PhD

University of Pittsburgh, 2015

Electrical equipment poses a danger to maintenance personnel when the equipment must be serviced energized. While de-energized maintenance is preferred, for some tests, doing so will not provide the needed performance data to validate important performance metrics of the equipment. In particular, sites with a high cost of downtime (health care centers, data centers, continuous process manufacturing, etc.) identifying a problem that could affect series integrity of conductors (continuity) of service is critical. The infrared thermal imaging test is a common method of inferring the resistance of a connection by measuring the temperature of a component, and when normalized to current flow, can be used as a proxy for the effective resistance of the current path. Deviations from historical ratios of temperature to current may indicate a change in the junction resistance. The problem is that IR cameras require line-of-sight visibility with the energized electrical component to be tested. Many times due to available fault currents, fault clearing times and/or voltage levels, this cannot be done from a far enough distance to afford the operator safety even when wearing the maximum available PPE (personal protective equipment). The challenge has been how to perform this measurement safely and accurately, but still recognize that capital (for specialized test equipment) and expenses (for labor to perform testing) are frequently limited. Therefore, having a method of performing these tests throughout a facility, ideally performed from a central location while not requiring specialized equipment (leveraging the already installed IEDs [intelligent electronic devices]), would be a valuable solution. This research discovered a solution that reads low-resolution data from legacy IEDs but processes it to improve resolution to a point where ultimately it can be used to measure junction-to-junction impedances to sufficient resolu-

tion to detect failing connections. The research outlines the statistical analysis, filter design and conductor temperature normalization algorithms necessary to achieve this goal.

TABLE OF CONTENTS

LIST OF FIGURES

LIST OF TABLES

NOMENCLATURE

α	Temperature Coefficient $\left(\alpha = \frac{1}{R}\frac{dR}{dT}\right)$, where R is resistance and T is absolute temperature.
ε	Surface emissivity
ε_x	Network latency (random variable)
η	Efficiency of heat sink
σ	Stefan-Boltzmann Constant: 5.6704 x 10^{-8} W m^{-2} K^{-4}
σ_e^2	Variance of noise. Since noise assumed to be wide-sense, stationary white noise with zero mean, average power and variance are the same [71, pg 204].
AWG	American Wire Gauge
CHU	Precision (atomic) time signal broadcast from Canada
COMTRADE	File format defined by IEEE [74] for storing time series data, typically waveforms
CSV	Comma Separated Variable (file format commonly used as an open format to share spreadsheet data)
DCA	Data Collection Arbitrator
DCF-77	Precision (atomic) time signal broadcast from Germany. Term also defines a particular time protocol
ESFI	Electrical Safety Foundation International
FIR	Finite Impulse Response filter
HEAF	High Energy Arc Fault
HERD	Harmonic Energy Ratio Detection (see 6.1.1)
ICMP	Internet Control Message Protocol ("PING" [Packet InterNet Groper] is an example ICMP message)

i.i.d.	Independent, identically distributed random variable (all random signals have same probability, but are uncorrelated with one another)
IIR	Infinite Impulse Response filter
IR	Infrared
IRIG-B	Inter-Range Instrumentation Group time code (pronounced “eye rig bee”)
ISR	Interrupt Service Routine
IED	Intelligent Electronic Device
LPF	Low Pass Filter
LSB	Least Significant Bit
LW	Long wave (radio frequencies less than 300 kHz. LW signals travel via ground wave and therefore have fixed propagation delay)
MV	Medium Voltage (IEEE 141 Table 3 defines voltages within the range of 2400 to 69 000 as medium voltage.)
NEC	National Electrical Code
NFPA	National Fire Protection Association
NTP	Network Time Protocol
PTC	Positive Temperature Coefficient
PPE	Personal Protective Equipment
PTP	Precision Time Protocol (IEEE Std 1588-2008 used in ANSI C37.238.2011 IEEE Standard Profile for Use of IEEE 1588 Precision Time Protocol in Power System Applications)
PXIO	Power Xpert Input Output (I/O module for PXM, defined below)
PXM	Power Xpert Meter (brand name of a particular Eaton IED)
Q	Quality Factor. Measurement of the damping factor of a resonant circuit. In an ideal series RLC circuit $Q = \frac{1}{R}\sqrt{\frac{L}{L}}$, whereas in a parallel RLC system the Q is the reciprocal, $Q = R\sqrt{\frac{C}{L}}$
RTD	Resistance Temperature Detector
S	Set point or Specific Heat of cooling media
SHA	Secure Hash Algorithm (a family of cryptographic functions [SHA-1, SHA-2, etc.] commonly used to encrypt IED data)

SNR	Signal to Noise Ratio
SPD	Surge Protective Device (defined in [49])
SW	Short wave (radio frequencies between approximately 1.8 - 30 MHz. Rely on skywave [ionospheric] reflection and so have stochastic time delay properties)
Stratum	Number defining the quality of a clock's accuracy, drift and noise (ANSI T1.101-1999, Synchronization Interface Standard)
VBA	Visual BASIC (Beginners All-purpose Symbolic Instruction Code) for Applications (Trademark of Microsoft [63])
VSTO	Visual Studio Tools for Office (Microsoft [64])
UL	Underwriters Laboratories [8]
WWV	Precision (atomic) time signal broadcast broadcast from the United States

ACKNOWLEDGMENTS

I have been interested in science my entire life. As an elementary age student I recall deciding that during each of the upcoming summer breaks I would study one branch of science exclusively during that particular summer. My goal was to determine which branch of science I liked best. During one summer break I spent the entire summer studying geology. In other summers, chemistry, astronomy and electricity. It was during the study of electricity between the 5th and 6th grades that I decided to stop my search since I had realized that I wanted to be an electrical engineer!

Planning to be engineer when I entered college, I happened to room with someone who tried to convince me to sell door-to-door during the upcoming break. Such an affront! I was an engineer and would not "stoop so low" (later I learned that *everyone* must learn to sell, whether selling a proposal or project, convincing a company to hire you or convincing your boss you are worth more and should be paid more, etc.... selling skills are important.) When I saw my roommate the following year and learned he had earned ten times what I had made during the summer, I changed my mind and joined him the following year. After selling for the following 3 summers I decided that what I really wanted to do was be an engineer who sells ideas. Westinghouse had a position for me, and I was on my way.

Perhaps because of my interest in all branches of science, I've tended to look at engineering problems from a "systems" or overarching point of view rather than focus on a single domain. This curiosity, I believe, has served me well as I moved with the company to help them identify needs in the industry where my company's strengths might offer a solution.. Eaton gave me the opportunity to continue my education and paid for courses at Drexel University that formed the foundation for my successful passing of the Pennsylvania Professional Engineer (PE) license exam twenty years after completing my BSEE (and likely that long since I had used Laplace transforms!). Later Eaton

endorsed and paid for my Masters of Science degree in Electrical Engineering and now this Ph.D, both from the University of Pittsburgh.

Completing a Ph.D "part time" requires requires nothing less than a complete commitment to the task. The decision to devote the time and effort towards this goal was not taken lightly. This pursuit also was not begun without consulting with, and receiving approval from, my family. The many long hours (sometimes all night or weekend) spent studying, running experiments or writing while I did my best to interleave family time, school, volunteer time at church and not to mention my full-time job at Eaton, were a strain not only to me, but to those who depend on me. I very much want to thank my wife Kathryn and daughter Taylor for the support, prayers and encouragement all during this time. They worked hard to keep me balanced. Special thanks also goes to my mother-in-law, Wava (a retired teacher), for continuing to ask about my progress. Her interest helped keep me on track. I'm convinced the prayers of both she and my father-in-law, John, were instrumental in my achieving this success.

Though mentioned earlier, I want to emphasis my thanks towards my employer, Eaton. A company is made up of individuals, and I want to thank those individuals for helping make my efforts a success. While there are many people within the company that encouraged and helped me in this effort, I wish to thank several people by name as they helped me formulate my dissertation topic or answered questions, which later helped me to develop the solutions that I've been fortunate to develop. In some cases, this help even extended to their recommending me for, or facilitating my ability to obtain, this degree. Specific thanks go out to Lennart Jonsson, Daryll Fogal, Bob Yanniello, Dr. Engelbert Hetzmannseder, Dr. Thomas Schoepf, Luis Pereira, Dr. Xin Zhou, Brandon Ekbert, Nadia Morzowich, Doug Carolan, Dave Tallman, Kevin McLean and Tom Gross. Special thanks to Dan Carnovale for being a friend and adviser and for letting me "borrow" his PSEC lab. A lab so highly instrumented, that my research effort was tremendously simplified because I was able to mine the thousands of data sets he has collected over the many years of running tests. This saved countless hours of not having to set up and repeat those tests. I'm convinced that the readily available data allowed me to discover things, that if it were not for Dan's PSEC lab, would not have been discovered by me during this Ph.D.

And speaking of help, it goes without saying that I could not have reached whatever measure of success I have had in this pursuit without the education I received both at the undergraduate

level from the University of Kentucky and now at the Masters and Ph.D level at the University of Pittsburgh. I mentioned earlier that a company is made up of individuals – so is a university. Without the professors and committee members from whom I took classes or from whom I was fortunate enough to receive guidance, I would not be writing this dissertation. Thanks go out especially to Dr. Gregory Reed, Dr. Amro El-Jaroudi, Dr. Mahmoud El Nokali, Dr. Zhi-Hong Mao, Dr. Thomas McDermott, Dr. David Tipper, Dr. William Stanchina and Dr. Luis Chaparro.

Most importantly, I recognize that anything I have or have been able to do or accomplish has not been due to my own effort. I know that any abilities I have are gifts and I acknowledge that with my deepest thanks. With this success comes a recognition that I must use these abilities I've gained to share with and help others – "Each of you should use whatever gift you have received to serve others ([16, 1 Pet 4:10])." Thank you Lord for helping me every step of the way.

1.0 INTRODUCTION

Working on energized electrical equipment can be dangerous[12]. According to the US Electrical Safety Foundation International (ESFI), over 2000 US workers are admitted to burn centers for treatment of severe arc flash burns each year[35] as a result of injuries received when working on electrical equipment. In addition, to these injuries, another 2000 workers (i.e. 4000 total) workers miss work due to some type of non-fatal electrical injury[36] received on the job.

Burns occur from arc flash events as a result of electrical system insulation systems failing and sufficient fault current flowing through air between energized conductors (i.e. separate phases of a 3-phase system) or between an energized conductor and ground to create a high temperature ionized plasma.. Sometimes known as high energy arcing fault (HEAF)[19], incident energy released during the fault[86] can vaporize conductor metal and eject this plasma vapor at temperatures in excess of the boiling point of any known material[53, 57], and do so at ejection rates exceeding the speed of sound and at pressure levels sufficient to destroy electrical equipment[54]. For this arc to occur there must be an ionized path through air. This ionization may occur due to poor series electrical conductivity between connections causing arcing. As this arcing continues, a plasma cloud builds up around the conductor that may grow to encompass an adjacent energized conductor or ground. Once breached, this relatively low impedance plasma arc path now permits a large amount of current to flow which in turn increases the Lorenz forces[57] on this arc pushing the arc away from the source. The arc stops when it reaches a boundary (insulation), where the heating increases substantially[54]. One example of a root cause of a documented HEAF event was a poor connection between switchgear power breakers bus stabs and the corresponding bus bars in which the breaker connected (following a rack in operation)[19]. The extreme danger when working on

energized electrical equipment certainly points to mandating that maintenance personnel not approach energized electrical equipment. One solution would be to perform maintenance on only de-energized equipment, but this is not always possible. For example,

- Infrared scanning of electrical conductors is used to locate loose connections (known as "hot-spots") requires that sufficient current be flowing through the conductor being scanned to duplicate the heating during normal operation. A de-energized conductor would not generate heat and therefore any high resistance connection could not be seen. Test sets can be connected to simulate this current, but as discussed later, the effects will not exactly duplicate the "in service" operation.
- Partial dissassembly may be required to access or remote equipment for test. This can induce mechanical changes (movement, vibration) that can change the characteristics of bolted or spring loaded (stab) connections.
- Other metrics that require not only voltage, but also nominal current include measurements of voltage drop, magnetic field strength, sound levels and vibration. Measurements of these signals are meaningless unless the components are energized.

Note that frequently, switchgear used in mission critical facilities [26, 2, 73] may include the ability to remove equipment from energized electrical equipment. So while some components may be removable and permit bench testing, this type of testing could potentially mask problems that could only be observed from the device being installed and operating.

This is because for components that support removal, bench testing of these components does not demonstrate functionality duplicating when they were installed in the original system. The act of moving, unplugging, jostling, sliding contacts to remove or replace, which must burnish the surface and so remove oxidation or other mechanical action, can all change the performance of the component. Additionally, removing and restoring current results in changes to magnetic and thermal stress due to the removal and restoral of power. Practical high-current test sets us lower voltages to limit the kVA requirements, but lower voltages may not break through contact oxides and not mimic actual in-circuit performance when operating at much higher voltages [81].

All these effects can result in changes to measured performance metrics. It should be noted that a system could be designed to provide continuous measurement of series resistance by mimicking

the functionality of the IR imaging test by interrogating locally mounted temperature sensors or even cameras. This solution would require installing temperature sensors or cameras at appropriate locations to measure junction temperature. These sensors could be in the form of resistance temperature detectors (RTDs), thermocouples (T/Cs), thermistors or IR pyrometers. Each sensor requires an appropriate interface to instrumentation. These interfaces could include an analog input module connected to a suitable data acquisition device. For more sophisticated temperature sensors (such as permanently mounted IR cameras), a more sophisticated serial interface is required. The difficulty of installing such a system is discussed in detail in this document, but for metal enclosed equipment, a large number of sensors would need to be installed to provide adequate fault locating performance. Also, for temperature sensors that must physically touch the component being measured, sufficient galvanic isolation for the A/D inputs to withstand not only nominal voltage levels, but transients must be provided.

Since insulation levels in equipment in industrial and commercial distribution equipment are typically 5 to 12 times nominal[26], A/D transient voltage withstand would need to be equally robust. The concern, of course, is that the complexity of such an implementation can quickly escalate to the point where the of number monitored points (sensors, A/D inputs, loggers, power supplies, etc.) results in a monitoring system that is less reliable than the underlying electrical distribution system being monitored! Even if care were taken to add sufficient margin through the selection of oversized components, the adding of extensive monitoring adds costs and acts as a disincentive for a user to purchase the required protection.

To address these problems, this research demonstrates a solution that works by using only electrical signals that would normally be available to legacy IEDs, overcoming the known problems common to conventional temperature sensing. It will also show how prediction of impending failures by measuring very small changes in circuit impedance can be accomplished.

1.1 DISSERTATION ORIGINAL CONTRIBUTIONS

This research presents several new ideas centered around detecting impending failures in electrical junctions. While there are many methods (this document provides a survey of those methods), the

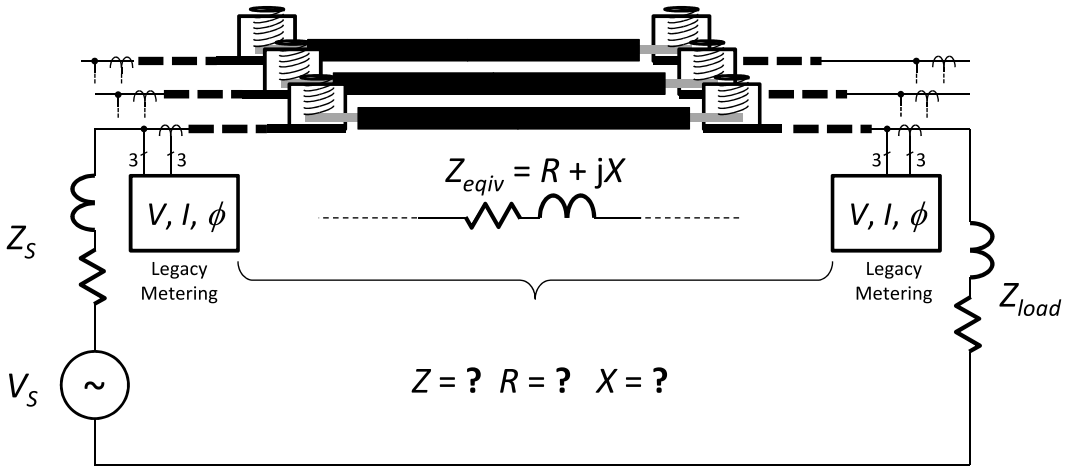

Figure 1: Central problem to solve is how to provide accurate measurement of Z, R, and X while using only legacy (low-resolution) metering and protective devices

goal of this research was to provide higher accuracy but with the overriding restraint that existing metering and protective devices would be used to provide any data required. This reduces the cost of implementation as no additional field devices are needed. All processing is performed offline, in potentially inexpensive computational engines. As the cost of computing continues to fall, the promise of a cost effective detection system only becomes more feasible.

As will be discussed, only permitting existing IED data to be used was a substantial constraint as these devices do not provide, as far as this research has shown, sufficient resolution, nor appropriate filtering to extract the patterns and features necessary to detect degradation in a junction. A degrading junction may only change the resistance by a few tens of micro-ohms, which for a circuit with a few hundred amperes of current flowing or less results in changes in voltage drop of only a few millivolts.

The research presented here solved this problem by introducing several new data analysis and filtering methods. One of the filters, derived from the Kalman filter, was extended even further beyond what appears to be present in the literature. Somewhat surprisingly, this research also uncovered a new filter method that provide even better resolution, providing both better stability and response time – usually competing features, with the trade-off of slightly less accuracy.

However, as will be discussed, knowing the absolute *magnitude* of impedance, resistance or reactance is only of secondary importance compared with knowing how much *change* the signal has experienced over time. For this, this new filter is ideally suited.

Another problem addressed and solved is the problem that the small resistance changes due to failing junctions can be masked by the normal conductor temperature changes, whether due to ambient or from current flow. Since commonly used conductors (copper and aluminum) exhibit a positive temperature coefficient so even nominal load changes on a circuit can result in a change in resistance so large that it is greater than many multiples of the change in resistance measured in a failing junction. The development of techniques to identify and separately filter this effect was critical. An interesting solution was found that used data found in National Fire Protection Association (NFPA) [7] data in a new way.

During the research, many waveforms were captured, each requiring analysis. To speed the process, a special program was written (Appendix B). It was during the analysis of the waveforms that a particular, an apparently previously undiscovered method was discovered that allowed detecting the location of faults using a simple waveform wave shape analysis (Appendix A). This finding formed the basis for a separate journal article.

Finally, another key discovery revolved around accurate measurement of the phase angle of the conductor. For many power distribution systems, inductive reactance predominates over resistance as the primary component of impedance. When a junction begins to fail, real energy is dissipated as heat as the degradation increases the circuit resistance. While accurately measuring small changes in impedance across a conductor many times is good enough, having the additional ability to discern whether the impedance change is due to resistance or reactance provides better localization of faults and as well as better discrimination against false positives. But, as mentioned earlier, the overriding caveat is that any such method must only use data from existing metering devices which may have poor timing accuracy so obtaining synchrophasor-like accuracy, while needed was a challenge. This research outlined a novel method that eliminates the critical timing requirement for measuring the phase shift between distributed IEDs. Instead, X/R ratio (power factor) of circuit is estimated by measured attenuation by power system harmonics pre- and post-events.

In closing, after spending about a year writing data analysis programs and using those programs to examine the data collected by legacy IEDs, I am even more convinced that this research has

merely scratched surface of the types of analysis are possible. First, for purposes of brevity, not all of the findings from that research have been included in this document. Secondly, not all of the findings have been independently validated, so are subject to change. But what is clear is that in the past the data that has been discarded as noise has turned out to provide rich insight into "hidden" data available within the time series data collected by legacy IEDs.

I outline some of that proposed continuing research in chapter 6, but even that only touches on the possibilities. Some of the data plots I collected confounded my understanding of, and drove me to, discovering new relationships within the data that I've not seen documented elsewhere.

1.2 DISSERTATION OUTLINE

This document is divided into six chapters and two appendices.

Chapter 1 summarizes the original contributions discovered as a result of this research.

Chapter 2 begins with a review of the present state-of-the-art methods for detecting anomalies within measured and derived electrical distribution system signals ($V, I, \phi, Z, PF, W, vars$, etc.) and lists the particular limitations and difficulties in collecting data at a sufficient resolution and accuracy to be useful when calculating conductor or junction impedances. This chapter subdivides this discussion into methods of measuring conductor temperature, impedance and timing (phase).

Chapter 3 introduces the concept of multivariate analysis (measurement of signal of interest and comparing that to secondary byproduct signals and examining the correlation). In particular, the concept of using harmonic content to excite the conductor at several frequencies and then using Fourier and rms decomposition as a novel method of determining actual resistance and reactance at each frequency is presented. This discussion of accurate measurement of phase angles is covered further in Chapter 5.

Chapter 4 covers oversampling and designing various filters types as two methods of extracting additional information from the computed values of impedance and phase angle (which leads, therefore, to resistance and reactance measurements). It is in this chapter when the concept of the median / mode filter is presented and its performance is compared with a variety of other filters. This section also builds on the methods introduced in Chapter 2 describing ways of estimating

conductor temperature. Chapter 4 also introduces an improved method of normalizing conductor resistance based on knowledge of the secondary effect of varying current flows causing sympathetic heating. The method draws on a special "reverse analysis" of data derived from National Fire Protection Association [11] test data.

Chapter 5 discusses how accurate comparison of measured versus modeled phase angle for *RLC* circuits is complicated since many idealized models do not include resistance (or reactance) in the conductors connecting the reactive elements. As discussed in this section, this causes errors when attempting to derive and accurately model actual $R + jX$ values for a circuit. Incorrect estimates also affects derived measurements of Q, resonant frequencies and power factor. This section derives the correct compensation factors that allows simulated systems to match bench test models. Normally such high accuracy would not be needed, but since the entire focus of this research has been on extracting more resolution from measured signals, any factors that could decrease this resolution (by adding unexplained deviations) must be analytically determined.

Chapter 6 touches on potential extensions and implications of the findings in this research. Specifically, using a variation of the methods described in the earlier chapters (namely, the method of measuring very small values of Z, R, and X very precisely), chapter 6 extends the idea by proposing that if a small value could be computed accurately, then the reciprocal of a small value could also be computed accurately. This variation, then, looks to solve for the reciprocal of these values, in effect accurately measuring changes in very large values. Such a condition might occur within degrading insulation, surge protective devices or lightning arresters or bushings implying that the methods outlined here could be used to detect that those impending failures too. Preliminary bench test data included in this chapter agree with these assumptions.

The research concludes with two appendices. The first is a more detailed discussion of one of the practical applications that came about as a result of the ability to measure accurately small impedance values – locating faults. While in large part, this dissertation focuses on detection of small *additional* impedances in *series* with normal load currents, the reader quickly sees that having an accurate method of measuring small impedances in *parallel* with the load would be useful too. A low impedance path in parallel to the load is considered a fault. This detection method is similar to distance relaying methods with the difference that the algorithm is much simpler and easier to implement, especially when used in mesh, loop or micro-grid (local generation) systems.

The last appendix provides technical details and program code explaining how the IEEE COMTRADE file format [74] can be decoded. Many of the experiments listed in this dissertation were monitored by power quality meters that captured waveform data in the COMTRADE file format. While commercial programs are available that can open and manipulate COMTRADE files and then export to XLS or CSV file formats, having a custom built program that could read COMTRADE files directly into Excel (that was already pre-programmed with desired equations to manipulate that data) saved some time. In the interest of sharing this work with others, this appendix also includes a reference to an external site where the working application (including unlocked assess to view complete program code) can be downloaded.

2.0 ANOMALY DETECTION METHODS

Signals typically retrieved from electrical distribution systems and equipment include current, voltage, phase angle, real and reactive power, distortion, acoustic signature, temperature, partial discharge, breaker position (open, close, test, connected, disconnected), fault clearing time, oscillographic analysis of current, cumulative arcing current energy $\left(I^2t\right)$ and others. To determine if these signals are abnormal, tests are performed within the devices collecting the data including metering units, protective relaying or other processing equipment. Depending on the needs of the system, the detection and the processing of the signals may be separated by some distance. This can introduce the additional factor where the measurements from the different locations will not be collected with known time offsets. This time jitter introduces phase offsets and increases error and noise when attempting to measure small deviations in the signal over time. While none of these problems are not unknown in the industry, there are several unsolved problems when attempting to surmise the relative "health" of an electrical connection using signals available from commonly available electrical metering and protective relaying equipment.

- Limited Feature Extraction Algorithms

Feature extraction algorithms, or those that would be required to detect changes in nominal series impedance, are not available in protective devices, at least to the level of resolution required.. Distance relays that do measure impedance are available, but these devices are designed to detect distances to faults, not distance to (or even presence of) a degrading series junction varying by micro-ohms.

- Resolution / Accuracy Limitations

Measured results from failing equipment shows that characteristic resistance of a failing junction typically used in circuits rated from 200 to 2000 amperes varies by as little as 10^{-4} to $10^{-5}\Omega$.

These small changes must be measured in a system where round-trip impedances are measured in the order of$10^{-1}$to $10^{2}\Omega$ range are typical for 480V to 15 kV class circuits, respectively. Detecting such a change means detecting a change six orders of magnitude below nominal value. This place an extraordinary burden on the sensing equipment regarding resolution, linearity and accuracy.

- Temperature

Common conductive materials (copper, aluminum, silver, etc.) used in electrical distribution systems exhibit a positive temperature coefficient (e.g.$PTC_{Cu} \approx 3.9 \cdot 10^{-3}/^{o}C$). For even short conductors, this can cause significant error in the measured signals. For sufficiently long conductors or over a sufficiently wide temperature range, the change in conductor resistance due to normally occurring PTC effects can be equal to or greater than the resistance changes due to a contact or junction degradation.

- Other System Noise and Non-Linearity

Power systems are expected to include switching loads and sources, transients, harmonics, voltage regulation (taps changers, capacitor banks) and other non-linear events. Any feature extraction algorithm must be able to operate in this non-linear environment.

2.1 PRESENT DETECTION METHOD LIMITATIONS

It is possible that these problems have not been solved to date because the IED vendors have not provided the tools (in the form of signal processing tool kits) sufficient to extract the required data from the measured signals. While extensive tools are available, frequently the tools provided are limited to simple alarming and filtering. Also, as discussed earlier, many of the tools are designed to *remove* noise and not process the noise itself for data. Some of those tools are summarized here.

- Limit Test Tool

$$e = x(t) - S \tag{2.1}$$

$$\text{if } |e| > \text{A then } Alarm = TRUE \tag{2.2}$$

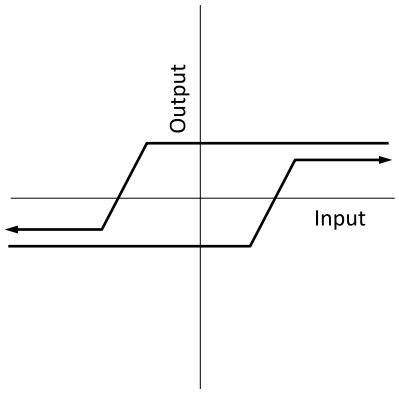

Figure 2: Alarm trigger hysteresis curve

The signal monitored is subtracted from a previously chosen limit value. Alarm state changes when the magnitude of this difference exceeds a fixed or dynamically calculated alarm set point. IED vendors typically include dead band (hysteresis) set points to limit retriggering due to a signal oscillating near the alarm set point.

What is not included is a function to statistically analyze the high frequency oscillations relative to the set point to derive sub-bit insight. The number of times, when and by how much the trigger points are exceeded, etc. provides valuable statistical data regarding the state of the system. A technique will be proposed to correct this oversight.

- Rate of Change / Slope

$$\text{if } \left|\frac{dx(t)}{dt}\right| > A \text{ then } Alarm = TRUE \text{ where } \left|\frac{dx(t_1)}{dt}\right| \approx \frac{x(t_1 - t_0)}{t_1 - t_0} \tag{2.3}$$

In a typical discrete time implementation, the time rate of change of a signal is monitored and if it exceeds a limit value an alarm is triggered. Common implementations are sine-wave tracking algorithms that signal when $\frac{dV(t)}{dt}$ or $\frac{dI(t)}{dt}$ exceeds a particular limit based on location within the sine wave.

- Spectral Analysis / Harmonic Content

A commonly available technique to analyze power system data is to perform a spectral estimation on the underlying signal(s). Fourier transforms (or other more modern spectral estimation techniques [88]) are performed to extract and separate the superposition of signal and noise (or signal

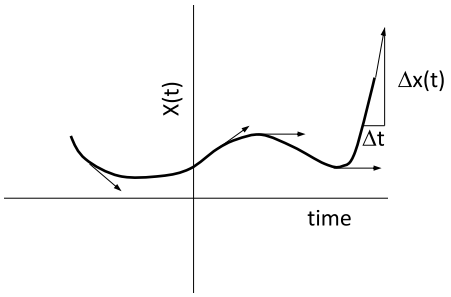

Figure 3: Alarm trigger rate-of-change curve

against other signals). One source of error with these techniques stems from IEDs using digitally sampled signals. As such, the practicalities of causal systems and sampling theory states that the calculated Fourier coefficients will not perfectly represent the underlying signal since infinite samples of data are not available. Practically, the algorithm will apply a particular window around the data prior to computing the Fourier transform.

$$X_k = \sum_{n=-\infty}^{\infty} x_n \cdot w[n-m]\, e^{-j2\pi kn/N} = \sum_{n=0}^{N-1} x_n \cdot e^{-j2\pi kn/N} \tag{2.4}$$

Each Fourier coefficient is compared to an expected value and alarmed if that value is exceeded.

$$\text{if } X_k > A \text{ then } Alarm = TRUE \tag{2.5}$$

One technique for providing more insight into the coefficients returned from a windowed / tapered discrete-time Fourier transform is to compute the relative ratio of these coefficients over time. By comparing these coefficients to each each other, the absolute magnitude of each coefficient (which will be in error) is not as important as monitoring the change of a coefficient over time. The presumption is that if the underlying system is known, then this parametric technique can be used to detect anomalous behavior.

$$\text{if } \frac{X_k}{X_{k-1}} > A_1 \frac{X_k}{X_{k-2}} > \ldots A_N \frac{X_k}{X_{k-N}} > A \text{ then Alarm} = \text{TRUE} \tag{2.6}$$

$$\text{if } \left| \frac{dX_n(t)}{dt} \right| > A \text{ then Alarm} = \text{TRUE} \tag{2.7}$$

Typically IEDs do apply limit and rate of change tests to the calculated coefficient values. For example, certain types of ratio tests are applied in harmonic restraint relays such as during transformer inrush. The current wave shape during inrush is asymmetrical due to dc offset and includes 2nd and 4th harmonic Fourier coefficients. Since these harmonics can be detected, and since they are indicative of transformer inrush, the IED can intelligently allow the circuit breaker to remain closed, even though the computed rms current (including those harmonic currents) is above the trip set point.

Another example involves accurately compensating for zero sequence harmonic currents. This type of harmonics, which are commonly created by non-linear loads when connected single phase (line-to-neutral), could cause an IED to nuisance trip on ground over-current since any zero sequence sensing scheme without harmonic restraint would interpret those currents as due to a ground fault. Triplen harmonics contribute to zero-sequence (ground) current and so can cause a nuisance trip on systems with single-phase non-linear loads (such as any rectified or switched mode power supplies commonly found in computers or other electronic devices.). A more appropriately programmed IED would chose to ignore (filter) any zero sequence harmonic currents or it may compared a ratio those higher frequency zero sequence current to the fundamental and ignored if below a particular limit.

- Time / Duration / State

$$\text{if } |x(t) \cdot S| > |x(t-k)| \text{ then Alarm} = \text{TRUE} \tag{2.8}$$

Any signal (or more accurately, any filtered signal) can be trended and compared with the same signal at a different time. This method is used to derive "normalized" operating bands. While most of our power systems are considered to be parametric (i.e. signals are caused from defined system properties), these systems all experience switching events which create non-linear forcing functions. These forcing functions can excite unknown resonances within the system.

Consider the electric arc, commonly produced from mechanical switching of an energized inductive circuit, which produces a characteristically wide band, largely uncorrelated forcing function. With this broadband noise including frequencies measured (and potentially exceeding) tens

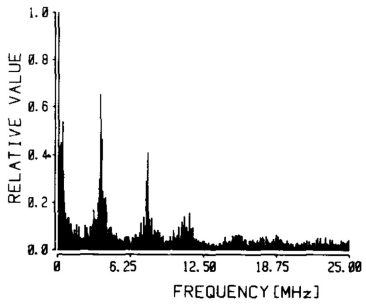

Figure 4: Spectrum of arcing frequencies Source: [66]

of megahertz [66], resonance points can be excited far above power system frequencies. In Figure 4 the author [66] notes that three prominent resonance points at 3.9, 7.8 and 11.7 MHz correspond to the resonance of the cables. A resonance points, higher than normal voltages can develop, potentially damaging equipment.

Since these frequencies exceed common excitation available due to nominal power system fundamental or typical harmonics (i.e. < 40th) produced by solid-state switching, a richer data set can be returned from a mechanically, rather than electronically switched system. By comparing these harmonic values to values entered by a knowledgeable user, the system could generate an alarm. Note that changes in either resonance frequency or the Q of a circuit is also indicative of a change in the system characteristics. Trending can be applied to any (filtered) measured or derived value.

As mentioned earlier, a more advanced trending technique is to trend ratios of harmonics over time to derive changes in system behavior. For example, the ratios of Fourier coefficients (equations 2.4 and 2.6) computed from an 24-pulse inverter can be compared at different times and at different load levels. Changes in the ratio of the harmonics would indicate changes within the inverter switching semiconductors, line reactors, parallel loads (which act as harmonic sources or sinks) or changes to the interconnecting conductors. Equation 2.9 shows one method for comput-

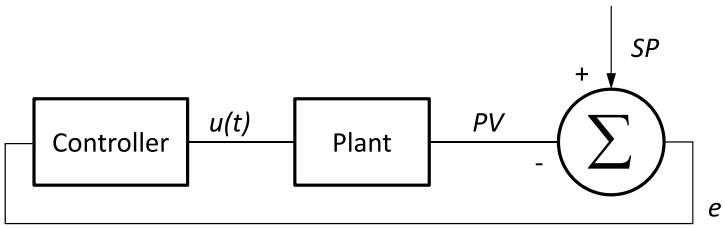

Figure 5: Conventional closed loop control model

ing the absolute value of the ratio of the same set of harmonics (Fourier coefficients) computed at two different times.

$$\text{if } \left| \frac{X_k(t)}{X_{k-1}(t)} \cdot S \right| > \left| \frac{X_k(t-k)}{X_{k-1}(t-k)} \cdot S \right| \text{ then Alarm} = \text{TRUE, where } S < 1 \tag{2.9}$$

Equation 2.10 calculates an alarm if the rate of change of the ratio of the Fourier coefficients exceeds a previously established limit. Once this is calculated, and IED may may low-pass filter this ratio depending on the system phenomena being studied (i.e. uncorrelated system noise creating large instantaneous deviations, so filter to remove this noise).

$$\text{if } \frac{d\left|\frac{X_k(t)}{X_{k-1}(t)}\right|}{dt} \cdot S > \frac{d\left|\frac{X_k(t-k)}{X_{k-1}(t-k)}\right|}{dt} \text{ then Alarm} = \text{TRUE, where } S < 1 \tag{2.10}$$

In general, any measured or calculated value can be compared with the same value at a different time.

$$e = |x(t) - x(t-k)| \tag{2.11}$$

Note the similarity between equation (13) and the standard control system definition of an error signal (equation 2.12and figure 5):

$$e = SP - PV \tag{2.12}$$

Since the human eye and brain are powerful signal processors themselves, a common visualization technique for error signals is to plot them in 2, 3 or more dimensional plots. Figure 6 shows

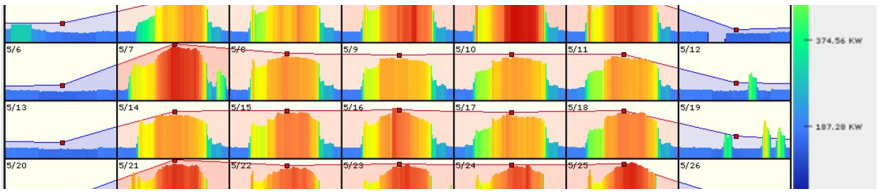

Figure 6: Histogram - Percentage of Full Scale

a three dimensional plot (x-axis time, y-axis value, and color calculated deviation) that correlates a metric to a particular time of day. In repeatable processes (knowledge workers in office building, manufacturing plant floor, HVAC correlated to weather), such diagrams can flag deviations.

While useful, 6shows only the moment by moment percent of full scale.of the signal without any insight into if that signal level is considered abnormal.

A more useful diagram is shown in 2.1 on the next page. In this diagram, color codes correspond to dynamically derived rather than fixed limits. Color is based on the magnitude of deviation from a nominal (average) for a particular 15-minute time slide within a particular day and for a particular day of the week. It is important to recognize that each of these alarm methods can be used with either actual measured signals or derived values. For example the reddish-pink color shown on 4/20 in figure 2.1 on the following page indicates that even though the magnitude of the values are low, they are abnormal due to when then are occurring. Derived values can also include data from two or more signals, what is known as multivariate analysis.

$$e = |f(x_1,\ldots,x_n,t)\cdot S| - |f(x_1,\ldots,x_n,t-k)\cdot S| \tag{2.13}$$

Each of these methods is suitable for either parametric (known process) or non-parametric (unknown underlying process). Since the physics of an electrical distribution system are usually well understood, parametric and "parametric-like" techniques are used to extract the maximum possible signal to noise ratio. During non-linear events (switching, magnetic saturation), other methods are used. A key part of the analysis discussed later is how to examine the trended value and determine which algorithm is to be applied for a particular segment of time.

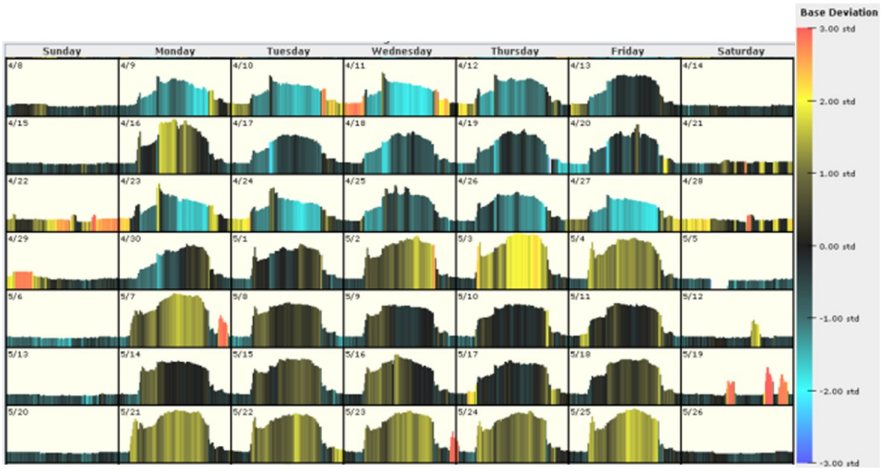

Figure 7: Histogram - Normalized

2.2 REVIEW OF DIFFICULTY IN COLLECTING ACCURATE BUS OR DEVICE TEMPERATURE DATA

Electrical devices are connected with conductors. Each conductor has a resistance and reactance that can be related to geometry of the conductor, position with regards other metallic objects and with itself, composition of the conductor, temperature, contamination, frequency of the current flowing as well as certain other factors. Secondary effects such as changes in current can affect conductor temperature creating a feedback mechanism that modifies the conductor resistance, and therefore the current flow and ultimately the temperature. This relationship between conductor resistance and temperature can be either positive or negative but it is usually a known physical property and can be parameterized and modeled to an arbitrary level of precision (based on time provided) using information learned by comparing calculated impedance as a function of current flow and ambient temperature. Electrical current flowing through the non-zero resistance of the conductor will generate I^2R losses as heat.

This heat increases the conductor temperature and changes its resistance. Over common operating ranges, this relationship between conductor resistance, temperature and current could be modeled mathematically simply as:

$$R \propto f(T) \propto f(f(I)) \tag{2.14}$$

where:

R	resistance
T	temperature
I	current

A complicating factor when using temperature to infer resistance in a conductor is that there are many factors that contribute to conductor temperature. The internal temperature of the conductor follows the first law of thermodynamics (internal energy equals power input minus work done). The calculation of the power input due to current flow across a resistance is straight forward.

$$\dot{Q} = P_i = I^2 R \tag{2.15}$$

Because this heating raises the temperature of the conductor above that of its surroundings, the conductors are cooled as defined by heat transfer equations. As that energy transfers, work is performed on the surroundings and the conductor internal energy (and therefore temperature) is reduced. The magnitude of the temperature change is based on the difference between the energy input, Q_{in} and the energy lost due to cooling, $Q_{cooling}$.

$$\dot{Q}_{net} = \dot{Q}_{in} - \dot{Q}_{cooling} \tag{2.16}$$

Ignoring vaporization (phase change) effects, energy lost from cooling can be divided into three types of cooling:

$$\dot{Q}_{cooling} = \dot{Q}_c + \dot{Q}_v + \dot{Q}_r \tag{2.17}$$

Where:

Q_c	Conduction cooling

Q_v Convection cooling

Q_r Radiation cooling

For a single point, conduction, or the heat lost flowing through the conductor from an area of high temperature to an area of lower temperature is defined as:

$$\dot{Q}_c = \frac{k}{x} \cdot A\,(T_h - T_c) \tag{2.18}$$

Where:

k Thermal conductivity of surface area between two objects

X Thickness of insulating material of surface area between two objects

A Surface area of two objects touching one another

T_h Temperature of higher temp object

T_c Temperature of cooler temp object

Over a surface, conduction can be more accurately modeled using a surface integral.

$$\frac{\partial Q}{\partial t} = -k \oint_S \overrightarrow{\nabla} T \cdot \overrightarrow{dA} \tag{2.19}$$

Where:

$\frac{\partial Q}{\partial t}$ Heat transferred from the object

k Thermal conductivity of material(s) (W $\mathrm{m}^{-1}\mathrm{K}^{-1}$) Note that k is placed outside integral. This is based on the assumption that thermal conductivity is constant across the surface. This may not be true, in which case k would be replace with $k(A)$ and would be moved within the surface integral equation.

∇ Temperature gradient (K m^{-1})

$\overrightarrow{dA}$ Surface area over which the conduction takes place (m^2)

A practical implementation of this partial differential equation uses a finite element model calculated using equation 2.18, where both object (T_h) and ambient (T_c) temperature modeled at each point on a surface are used. Equally well understood, convection occurs when an electrical device heats a fluid (e.g. air) to a temperature warmer than its surroundings. This heated fluid has a lower density than the fluid more distant from the heated conductor. The warmer, lower density fluid

(e.g. warm air) rises above the cooler, denser fluid. Cooler fluid flows in as a replacement, creating the convective air flows. The complexity of the fluid dynamics mathematics varies depending on whether the replacement fluid flows slowly enough to remain laminar or results in turbulent flow.

In the simpler, laminar case, convective heat transfer is mathematically derived from the ideal gas law and the result is shown in equation 2.20:

$$\dot{Q}_v = S\eta F\left(T_h - T_c\right) \tag{2.20}$$

Where:

S	Specific Heat of cooling media
η	Efficiency of heat sink
F	Flow rate of cooling fluid

Unfortunately, in the more typical case (because forced air cooling is commonly used in electrical equipment), turbulent flow and a gases' compressibility make equation 2.20 inaccurate in predicting convective heat transfers. The more precise solution is found from creating equations that conserve mass, momentum and energy as the cooling media travels across the heated component. Since the method described in this paper of determining the expected temperature of electrical equipment uses a different technique, the details of the method based on conservation of mass, etc. will not be covered here. In fact, the complexity of conservation equations are even further complicated since heat transfer via radiation must be included. Cooling due to radiation needs to be factored, since the energy lost through radiation is non-trivial at typical electrical equipment and conductor temperatures. The simplified equation for heat transfer via radiation between an area of high temperature to low temperature is shown in Equation 2.21.

$$\dot{Q}_v = A\sigma\varepsilon\left(T_h^4 - T_c^4\right) \tag{2.21}$$

Where:

A	Surface area of heated part
σ	Stefan-Boltzmann Constant: 5.6704 x 10^{-8} W m^{-2} K^{-4}
ε	Surface emissivity (0-1)
T	T_h – high temperature object, T_c – low temperature

As with conductive and convective heat transfer, a more accurate model applies a surface integral equation, since the temperature gradient between any two points likely not be the same. Regardless of the method used to compute the cooling due to conduction, convection or radiation, the first law of thermodynamics states that a point is reached where, for constant power input, the temperature will stabilize. When the temperature of an electrical device temperature stabilizes, the cumulative value of net energy ($\dot{Q}_{net}$) over a time window T must, by definition, equal 0.

$$\int_{t=0}^{t=T} \dot{Q}_{net} dt = 0 \tag{2.22}$$

From Equation (24), then:

$$ave\left(\dot{Q}_{in}\right) = ave\left(\dot{Q}_{cooling}\right) \tag{2.23}$$

Substituting Equation 2.15 on page 18 for the LH side and Equations 2.18 on page 19, 2.20 on the previous page and 2.21 on the preceding page for the RH side :

$$ave\left(I^2R\right) = ave\left(\frac{k}{x} \cdot A\left(T_h - T_c\right) + S\eta F\left(T_h - T_c\right) + A\sigma\varepsilon\left(T_h^4 - T_c^4\right)\right) \tag{2.24}$$

If the conductor is warmer than the surroundings, then it will be assumed that the current flow through the resistance of the conductor will produce the heat energy that warms this conductor above the ambient. Re-writing Equation 2.24 to solve for this value of R yields equation 2.25:

$$R = \frac{ave\left(\frac{k}{x} \cdot A\left(T_h - T_c\right) + S\eta F\left(T_h - T_c\right) + A\sigma\varepsilon\left(T_h^4 - T_c^4\right)\right)}{ave\left(I^2\right)} \tag{2.25}$$

Because at the temperatures common in electrical systems, the inclusion of the $\dot{Q}_r$ (radiation heat transfer) term is necessary. However this term introduces a 4th power into the equation for R, requiring that a quartic equation be solved.. While numerical analysis would solve such an equation, there are other issues. One issue involves the precise determination of T_c.

2.2.1 Review of Difficulty in Collecting Ambient Temperature Accurately

Many times $T_c$is considered as the ambient temperature, but a question could be asked "which ambient?" Some might assume it is the ambient temperature surrounding the electrical equipment.

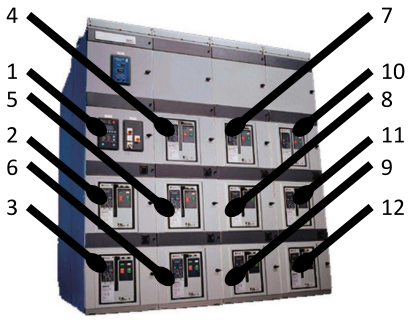

Figure 8: Ambient temperature sensors placement

This may not be appropriate, since conductor proximity to other current carrying conductors in 3-phase systems increases local "ambient" temperature due to current flow within those adjacent conductors. This micro-environment will be warmer than "outside" ambient, raising T_c. If using Equation (2.25) to solve for R, such an assumption will reduces the calculated value of R by increasing the magnitude of the numerator. If a system is built to measure and alarm on over temperature due to excessive resistance, then it is important to measure "ambient" temperature sensor accurately. The question is, then, where should such a sensor (or sensors) be installed?

Consider the simplified model of electrical switchgear shown in Figure 8. Multiple temperature sensors monitoring temperature of pressure junctions (hot spots) on 3-phase bus at multiple locations within the switchgear are required since such equipment includes many connections. Since Equation (2.25) predicts that an accurate measurement of R will only be possible with an accurate measurement of $T_c$and since $T_c$can vary with location within the switchgear, a prudent solution seems to mandate installing multiple ambient temperature sensors within the gear as shown by the dots marked "1" through "12"

Adding so many sensors adds cost and complexity, not to mention the computational complexity of computing Equation (2.25) location-by-location (e.g. finite element). Due to the complexity, cost and inaccuracy of this method, another solution would be preferred.

Table 1: Typically unknown or hard to determine parameters when solving heat flow problems involving electrical conductors

k	Thermal conductivity of surface area between two objects
X	Thickness of insulating material of surface area between two objects
A	Surface area of two objects touch one another
η	Efficiency of heat sink
F	Flow rate of cooling fluid
ε	Surface emissivity (0-1)

2.2.2 Conductor Temperature Compensation / Linearization

The calculation of conductor resistance shown in Equation (2.25) includes an I^2 term in the denominator, making it appear that the measured resistance is inversely proportional to the square of the current flowing. But this is not entirely correct, since the heating caused by this current flow raises the temperature of the conductor thus causing a secondary effect of increasing T_h which affects the calculation of the numerator. Actual installations must factor this relationship, but as noted in earlier discussions, it is not always desirable to solve the quartic equation to find this relationship.

Again referring to Equation (2.25) it is noted that several of the coefficients needed to solve for the cooling are difficult to measure precisely. These coefficients include those values shown in Table 1:

As was pointed out earlier, more accurate methods would solve integrals or surface integral equations. The point here is that rather than attempting to obtain these difficult-to-acquire values and then solve the necessary equations, it will be far easier (and likely more accurate) to collect temperature and current (amperes) data and perform a numerical analysis of the actual installation and use this data to work backwards to solve for the coefficients. In effect, becoming a state estimation where the internal states (data is used to model the plant. For an example, begin by collecting temperature and current data from an example system. This data are summarized in Table 2.

Table 2: Raw Data - Temperature Normalization

Amps	Ambient Temperature	Bus Temperature	Temp Rise
816	29	41	12
817	27	39	12
830	28	42	14
870	25	48	23
915	30	60	30

Where, looking at equation (2.25):

t_c "Ambient Temp"

t_h "Bus Temp"

i "1 min ave Amps"

$t_h - t_c$ $= \Delta t =$ "Rise"

Plotting the result of the difference between the bus and ambient temperature ("rise" or ΔT) with current flowing in the conductor, results in the plot shown in Figure 9.

Using least-squares curve fitting, a relationship between current flow and conductor temperature rise was calculated and is shown in Equation (27).

$$ave\,(T_h - T_c) = 161.84 \cdot ln\,(ave\,(I)) - 1073.2 \tag{2.26}$$

Equation (2.26) is then rewritten as:

$$ave\,(\Delta T) = K \cdot ln\,(ave\,(I)) - C \tag{2.27}$$

or

$$ave\,(\Delta T) \propto ln\,(ave\,(I)) \tag{2.28}$$

This equation predicts that the average temperature rise of the conductor will be proportional to the natural logarithm of the average rms current flow in the conductor. While this is a very useful

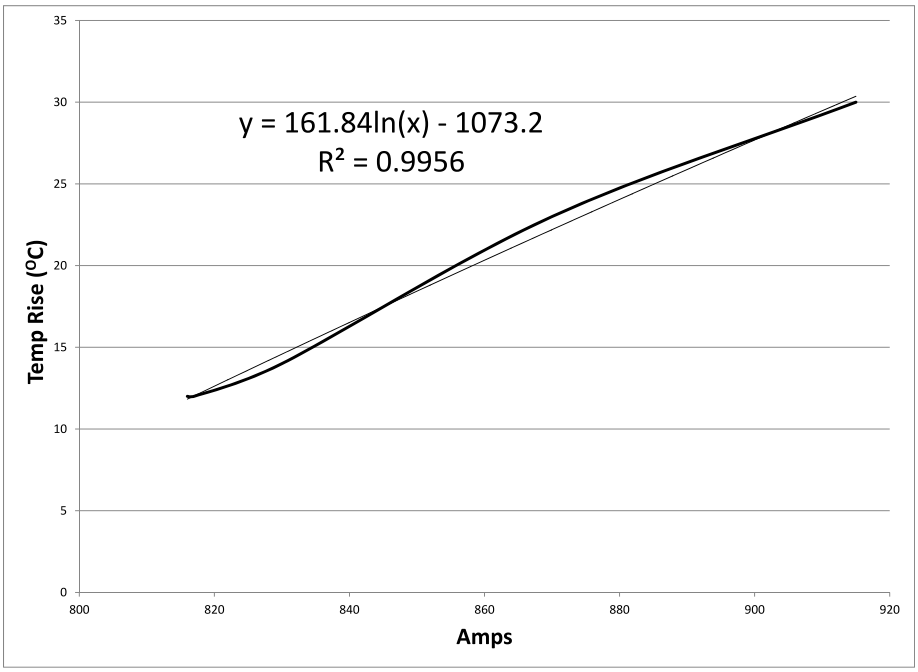

Figure 9: Temperature rise vs load current

insight, how can Equation (2.28) be used to quantify conductor resistance changes, such as would occur with deteriorating circuit breaker or load tap changer contacts?

The solution begins from recognizing that energy produced is related to current, since,

$$P = I^2 R \tag{2.29}$$

$$I = \sqrt{\frac{P}{R}} \tag{2.30}$$

Equation (2.30) is then substituted into Equation (2.28):

$$ave\,(\Delta T) \propto ln\left(ave\left(\sqrt{\frac{P}{R}}\right)\right) \tag{2.31}$$

Equation (2.31) predicts that for this application, when normalized to constant power, and over a somewhat narrow range of temperatures, the average change in the conductor temperature is proportional to the natural logarithm of the square root of the reciprocal of the resistance. Additional

complicating factors include the fact that conductors used in electrical equipment (e.g. copper, aluminum) exhibit a positive temperature coefficient. Therefore as conductor temperature increases, conductor resistance increases. As a result of this interaction, this equation cannot be used as a simple algebraic method to predict conductor temperatures based solely on changes in conductor resistance.

The take-away from this analysis is that subtle changes in resistance are very difficult to predict using temperature alone as a proxy. Since actual heating of a conductor is more strongly affected by changes in current flow as well as changes in resistance, properly normalizing any temperature reading based on current is critical.

Likewise, the closed loop feedback nature between current, resistance and temperature means that Equation (2.31) is non-linear and recursive (increase in R causes increase in T which causes an increase in R). One method would be to include the complete heat balance equation (2.24) since this recursive heating loop does eventually reach an upper temperature limit where heat input equals cooling. Such complexity should be avoided, since as was mentioned at the beginning of this section, many of the parameters of the heat transfer equations are not known precisely. By recognizing the complexity of the solution of these problems, it is fulfilling to be able to present a solution to this problem, especially a solution that does not require the accurate collection of those heat transfer coefficients or even of temperature.

2.3 DIFFICULTY IN ACCURATELY MEASURING IMPEDANCE

2.3.1 Offline Injection

Using milli- and micro-ohmmeters to measure junction and contact degradation has been common for many years. ([21, 85, 69]). The traditional method uses 4-wires (see figures 10 and 11), with two wires connecting the circuit under test to a low impedance source which injects a known current. The second pair of wires measure the voltage drop developed across the item under test. As alluded to in the abstract, offline injection may not be preferred since removing load current can change the temperature of the conductors or contacts. This changes their resistance, and in

the case of junctions, can change rates of oxide formation and, as a consequence, the junction resistance ([81]). Likewise, if mechanical operations such as disconnection or moving of items are performed, these can add vibration, change the pressure of the connection, or abrade (scuff) the surfaces, further changing their characteristics.

While these and other (listed later) limitations are known to exist, the offline current injection (milli- or micro-ohmmeter) method remains a popular method of performing non-destructive testing of an electrical connection. This dissertation will describe a different method of measuring impedance that uses nominal load current and therefore does not require any dissassembly or test bench work. However, prior to that discussion, the two types of offline current injection (direct and alternating current) are reviewed..

2.3.1.1 Direct Current (dc) Injection As with the conventional bench or tool box 2-wire ohmmeter, 4-wire milli- and micro-ohmmeter use direct current as the source current and measure dc voltage drop across the item under test. Also, dc testers tend to be low power, relying instead on sensitive voltage measuring capability. The consequence of low power is the tester sources current through a very low resistance resulting in a low output voltage.

As s result, low current doesn't heat the conductor or junction to similar temperatures, changing the bench-measured performance from perhaps the actual in-circuit performance. Also, a lower than nominal test voltage may be insufficient to break through oxide coatings, and likewise result in the test equipment reporting invalid resistances. So while, for many circuits, direct current will not accurately model the current applied to the circuit, using direct current instead of higher power ac current has the advantage of simplifying the measurement of conductor resistance. With direct current measurements, resistance can be computed directly from the current and voltage drop. No phase angle measurements are needed to resolve R as there is no jX in the measured Z. Since R increases as the connection degrades, measuring R alone provides additional sensitivity. A typical dc 4-wire test system is shown in figure 10.

2.3.1.2 Alternating Current (ac) Injection Because of the recognized limitations of low-power testing, mains powered alternating current test sets are available. Higher power ratings enabled by the connection to mains power allow the conductor and junction to operate at higher

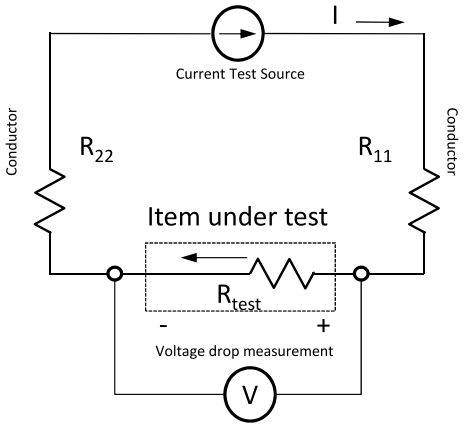

Figure 10: Offline dc current injection resistance test

current levels (although perhaps not at full or fault rated current). Also ac testing more accurately models actual circuit conditions by inducing the alternating magnetic fields that may interact with nearby conductors, inducing eddy currents with the resultant parasitic heating and vibration. Parasitic heating may increase the ambient temperature while vibration may change contact properties, both real-world situations. However, since contact and pressure connection degradation affects resistance, not inductance or capacitance, ac testing requires that the data be processed to extract resistance. This ratio of R as a function of Z or X varies with type of equipment, ranging from the value of R being only a small a fraction of the magnitude of X to being the primary component of Z([1, 4, 3]).

Separate of the discussion of whether direct or alternating test current should be used, ([81]) outlined many problems when attempting to perform offline current injection through a set of pressure connections. The paper specifically mentioned key problems when measuring the resistance of Ag-W contacts commonly used in circuit breakers. These problems include:

- Millivolt drop values change, with initial values tending to be transient in nature

- Surface oxides formed and required a certain magnitude of voltage to break through and obtain a reading (confirming earlier comment about problems of low-voltage testing)

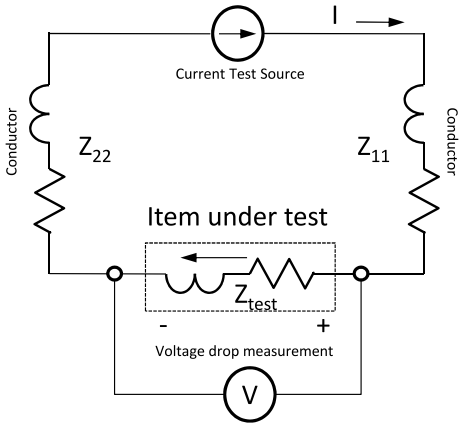

Figure 11: Offline ac current injection impedance test

- Millivolt drop measurements varied significantly with the measurement current used

- Measurement time, also, affected measured contact resistance due to heating causing secondary effects (silver softening and oxide phase transitions)

The recommendations from ([81]) was that any tests be performed only after the breaker has reached steady-state conditions at rated load. For this reason, it would seem that using nominal load current would be preferable when attempting to measure the resistance of pressure connections such as circuit breaker contacts, but only if this current maintained some steady state value.

While the problems of using offline testing are clear, one benefit of using fixed test currents (either ac or dc) is the ability to maintain a constant conductor temperature. When the conductor current changes, it has been shown (section 2.2.2) that the temperature change can be a non-linear function related to the current and of the underlying resistance of the conductor (which is, recursively, changing with conductor temperature). With an understanding of this problem, it becomes clear one of the major concerns of using nominal load current is the variability of the load current causing variable heating. While a practical and easily implemented solution to this linearization problem will be shown in section 4.1.4, attention is now turned to other difficulties when attempting to use nominal load current with legacy metering to determine conductor resistance.

2.3.2 Impedance Derivation Using Nominal Load Currents

2.3.2.1 Issues / Challenges When first asked how a breaker or load tap changer contact resistance could be measured with nominal load current, most would answer that by measuring current and voltage, Ohm's Law could be applied.

$$Z = \left(\frac{V_{rms}}{I_{rms}} \right) \tag{2.32}$$

Since degrading pressure connections show increased losses by virtue of increased temperature rise, it is realized that this energy must be dissipating across a resistance, not an inductance. If an alternating current were used instead of direct current, then the additional step of calculating the phase angle between the voltage and current would be performed to solve for this resistance across the contacts:

$$R = Z \cdot cos\phi \tag{2.33}$$

Where:

ϕ Phase angle between V and I

In fact, as discussed earlier (2.3.1) resistance testing using current injection is a normal maintenance procedure. When devices are de-energized from the circuit and a calibrated (typically very low) voltage with a current from a commensurately low source impedance is injected across the shorted contacts or connection, the resultant small voltage drop divided by the current does indeed provide impedance.

A suitable test set up is as shown in Figure 12, but the reader quickly notices that such a metering configuration would not be typical in a pre-installed electrical distribution system. The circuit breaker contact (or load tap changer contact) would be the point in the diagram marked ①.

Besides the non-standard connection of voltage metering, another potential disadvantage of such a connection is the need to connect a temporary current source across the contact. This, along with the likely need to de-energize the system, makes a permanently mounted continuous resistance / impedance monitoring solution in this configuration less useful.. One question that might be raised (when looking to remove the current source shown in figure 12), is "why not use

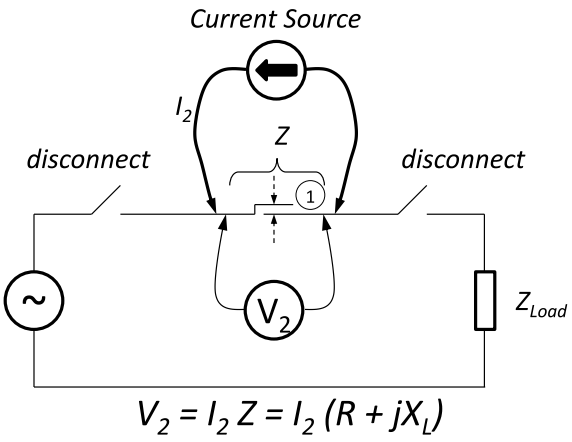

Figure 12: Current injection method of determining conductor resistance

normal circuit power to create the voltage drop?" Even better, perhaps, "why not use the existing metering common to electrical systems to measure voltage, current and phase angle so as to provide contact resistance?"

2.3.3 Challenges with Typical Placement of Existing Metering

First, since "typical" voltmeters are not connected across a set of breaker contacts, it is evident that a single voltage measuring device would not provide the needed voltage drop measurement capability. Also, as mentioned under section 2.3.1.2, since resistance, not impedance is the signal of interest, the additional step of measuring phase angle between the measured voltage and current would also be needed.

Since existing meters are wired to measure load current, such a set up could be shown as in figure 13.

Note that this calculated value of resistance, R, shown in Figure 13 would actually include both the resistance of the circuit breaker or load tap changer (shown as point ① in the Figure) as well as the resistance of any downstream (but not upstream) load, R_{load} and interconnecting conductors

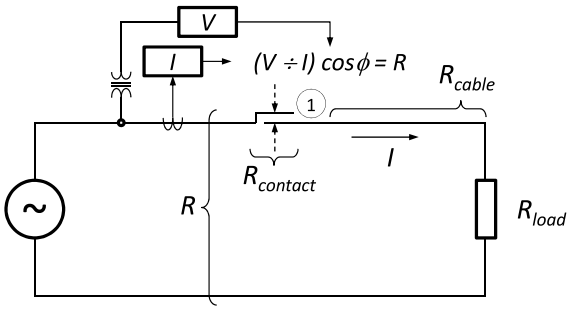

Figure 13: Single meter impedance measurement

R_{cable}. Using the metered values of V and I, the measured values of Z could be found:

$$\frac{V}{I}\cos\phi = Z\cos\phi = R_{contact} + R_{cable} + R_{load} \tag{2.34}$$

$$R_{contact} = \frac{V}{I}\cos\phi - R_{cable} - R_{load} \tag{2.35}$$

Since the resistance of just the circuit breaker or load tap changer $(R_{contact})$ is the value of interest, it is necessary to subtract, R_{load} and R_{cable} from R. One straightforward method of accomplishing this is to install a second voltage sensor downstream to calculate the value $R_{load} + R_{cable}$ (figure 14). The contact resistance $R_{contact}$ will simply be the difference between the calculated value of R_1 and R_2.

$$\frac{V_1}{I}\cos\phi_1 = R_1 = R_{contact} + R_{cable} + R_{load} \tag{2.36}$$

$$\frac{V_2}{I}\cos\phi_2 = R_2 = R_{cable} + R_{load} \tag{2.37}$$

$$R_1 = R_{contact} + R_2 \tag{2.38}$$

$$R_{contact} = R_1 - R_2 = \frac{V_1}{I}\cos\phi_1 - \frac{V_2}{I}\cos\phi_2 = \frac{1}{I}(V_1\cos\phi_1 - V_2\cos\phi_2) \tag{2.39}$$

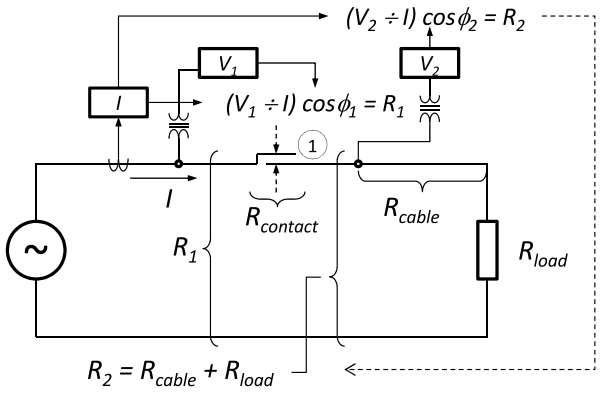

Figure 14: Dual meter impedance measurement

Metering and protective devices installed in legacy systems will almost never be configured to measure the voltage drop across a termination (refer to diagram A in figure 15 and recall discussions of meter placement in section 2.3.3). If such a metering arrangement was available, Z_S could be calculated directly from more likely metering arrangement found in legacy systems would be as shown in diagram B and C (figure 15).

From diagram A in figure 15:

$$Z_{Sa} = \frac{V_{1a} - V_{2a}}{I_{1a}} \tag{2.40}$$

From diagram B:

$$Z_{Sb} + Z_{cable} = \frac{V_{1b} - V_{2b}}{I_{1b}} \tag{2.41}$$

From diagram C, the values on either side of the transformer T_1 must be converted to a common base. In this case the upstream side is assumed to be the base and the downstream values will be modified to reflect a common base as as shown in figure 16

$$V_P = V_S \frac{n_P}{n_S} \tag{2.42}$$

$$I_P = I_S \frac{n_S}{n_P} \tag{2.43}$$

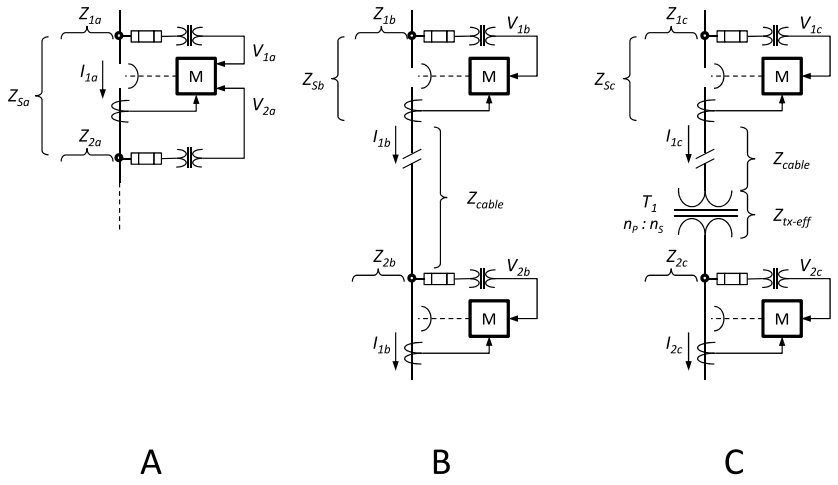

Figure 15: A- Desired metering to measure termination voltage drop. B - More common metering arrangement. C - Another common IED metering arrangement

$$Z_{Sc} + Z_{cable} = \frac{V_{1c} - V_{2c}\left(\frac{n_P}{n_S}\right)}{I_{1c}} \tag{2.44}$$

In actual installations equation 2.44 will be modified to compensation for the capacitive leakage current (since $I_{1c} \approx I_{2c}\frac{n_S}{n_P}$), resulting in equation 2.45.

$$Z_{Sc} + Z_{cable} = Z_{1c} - Z_{2c(eff)} = \frac{V_{1c}}{I_{1c}} - \frac{V_{2c}\left(\frac{n_P}{n_S}\right)}{I_{2c}\left(\frac{n_S}{n_P}\right)} \tag{2.45}$$

While the technique is clear, in actual systems the impedance shown as Z_S may include more than just the circuit breaker impedance. As practical installations include additional junctions between the locations where the voltage sensors are connected and the location where the device under test (contacts) are physically positioned. Figure 2.3.3 shows a typical load current path through a MV vacuum circuit breaker.

Of particular importance, is the location of the line and load side draw-out stab connections (shown at top and bottom left in figures 2.3.3 and 18). There are two main reasons for a focus on stab connection health. The first is that they may experience wear during even normal operation. The reason is that to facilitate easy insertion and removal of the circuit breaker, spring loaded stabs

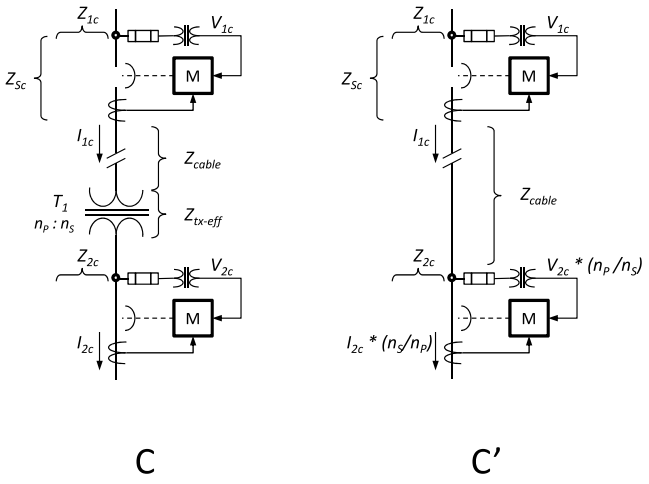

Figure 16: Converting to common base

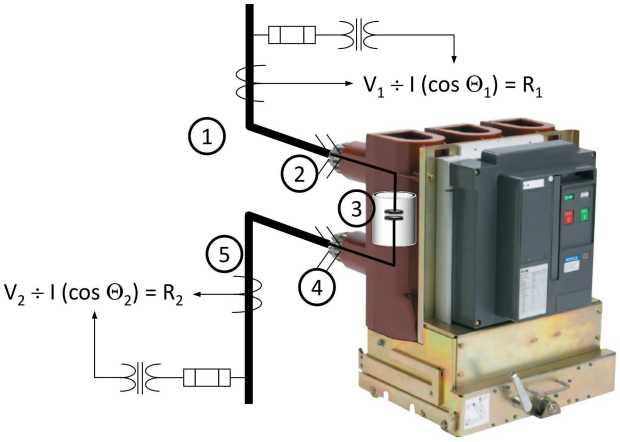

Figure 17: Potential "hot spot" locations along MV circuit breaker current path

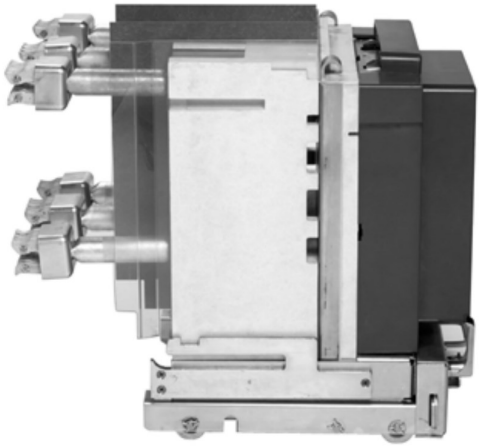

Figure 18: Side view of 15 kV class, 600A vacuum circuit breaker, with pole insulation removed. Line (top) and load (bottom) stabs are shown exposed at the left.

are fashioned at the end of bus bars that connect to stationary bus. Being spring loaded "pressure junctions" similar to breaker or load tap changer contacts, spring pressure will reduce as more material is abraded. More material is abraded with each operation. A common failure mode is for stabs to become worn or loose as a result of repeated racking operations. They could also be damaged due to environmental contaminants such as gas, chemicals, dust, insect nests (attracting dirt and other abrasive debris) or moisture or experience accelerated wear by being racked in a dirty/gritty environment. With a circuit breaker rarely tripping, the internal contacts can remain in pristine condition for extended periods. However, the number of insertions and withdrawal racking operations is limited, with some manufacturers only guaranteeing their products for 250 racking operations ([27]).

The second reason is that with the breaker inserted, the visibility of these stabs to either visual inspection or infrared thermography (IR imaging) is occluded by the breaker itself. In many types of switchgear, offline inspection is impeded as even with the circuit breaker is removed, the stab connection point in the switchgear is covered by a sliding window (shutter). Manually opening the window would be a delicate operation since the space between the front of the shutter to energized bus (potentially MV) may only be a few centimeters.

It would, therefore, be useful to determine if one or more of these spring loaded pressure connections were loose, corroded, pitted (due to arcing) or abraded during normal operation. A solution proposed here is to install a system similar to that shown in figure 14 to constantly monitor the $R_{contact}$ value and alert on excessive increase.

Notice that even if the metering system shown in figure 15, diagram A were applied to the circuit breaker shown in figure 2.3.3, what was called $R_{contact}$ in figure 14 actually encompasses more than just $R_{contact}$. Instead the metering system will calculate $R_1$and R_2, with the difference being the resistance between points ① and ⑤ shown in figure 2.3.3. Since that difference $(R_1 - R_2)$ on that same figure includes the resistance of both the incoming and outgoing stabs, plus the interconnecting conductors inside the breaker plus the resistance of the vacuum interrupter itself, this placement means that unless some other steps are taken, the measurement of $R_1 - R_2$ will detect that the problem exists somewhere between those two sensors, but not exactly how far from either. While this complicates the precise localization of the increasing resistance, having a system that can even report these additional resistances of these critical parts of the circuit breaker could be considered important anyway, since this method is able to detect changes in resistance in an area that is normally obstructed from view (visual or IR).

Another point to mention is that since these are 3-phase circuits, if the system were balanced (as most systems attempt, at least to some extent, achieve) each phase is nominally carrying similar (balanced) magnitude load currents. As such the calculated voltage drop (and therefore the calculated $R_1 - R_2$) will be similar between phases under normal conditions.

While environmental conditions would be expected to affect each phase equally, in practical systems the phase-to-phase effects vary. Consider how the Arrhenius effect greatly accelerates oxidation based on modest temperature differences (with the common simplification that the rate of chemical reactions doubles for every 10 ^oC or K increase [62]). This predicts that small differences in temperature can result in significant changes in oxide formation. Also, statistically, the likelihood of the same failure occurring on each connection at precisely the same time is smaller than the likelihood of a failure occurring on one at a time. Should a failure occur, it is more likely that a single junction fails rather than all three failing simultaneously. Therefore in 3-phase systems, additional error detection can be offered by performing a 2-out-of-3 voting of impedance deviation.

In other words, if one of the three phases shows an increasing resistance,while the other two phases do not, that is further indication that a problem exists on that one phase. Note that if all three do increase at the same time (after factoring out current and its commensurate affect on temperature and therefore resistance), the remaining condition is ambient. This manner, the monitoring system can also act as sort of an RTD based temperature monitoring system where the power conductors themselves report the system ambient.

2.3.4 Calculating Required Resolution from Legacy Metering

Up to this point, the discussion has only mentioned meter location and simple Ohm's law calculations, with perhaps an inferred assumption that if the meters were in the right location, resistance could be measured and problems detected.. Unfortunately another problem occurs when actual legacy metering is used to obtain these voltage and current values. When experiments were performed to capture and use the data from conventional metering devices typically used with switchgear, several problems were discovered.

The first problem is the issue of obtaining sufficient measurement resolution, repeatability and inherent accuracy. Consider the following example:

- 13.2 kV, 200A circuit with "normal" contact resistance of 100 $\mu\Omega$ per phase (see figure 2.3.3)
- Voltage metering capable of resolving any voltage from 0 – 14.4 kV
- Current metering capable of resolving any current from 0 – 300 A

The analysis begins by examining the voltage drop and power loss across a resistance of 100 $\mu\Omega$ while 200 amperes flows:

$$V = IR = 200 \cdot 100 \cdot 10^{-6} = 0.02 \text{ Volts} \tag{2.46}$$

$$P = I^2R = 200^2 \cdot 100 \cdot 10^{-6} = 4 \text{ Watts} \tag{2.47}$$

Degradation of a lug or stab occurs when increased resistance results in higher than normal losses and temperatures that exceed equipment rating. For most enclosed electrical equipment,

standards (such as UL 489 ([46]), 891 ([48]), 1066 ([51]), and 1558 ([47]) for low voltage equipment) place absolute temperature limits on any conductor, circuit breaker lug or transition point inside the electrical equipment). As a connection degrades, less-metal to metal junctions are present as oxides and contamination form (which have poor resistivity than the underlying metal) or just the lower pressures across the connection reduces the surface area actually touch each conductor (see figure 19).

These conditions raise the resistance of the connection which increases power losses. While the overall connection temperature increases, at the microscopic level, the fewer touching "peaks" now pass all the current, causing even higher temperatures. When those higher temperatures reach the boiling point of the material, the gas vapor begins conducting the current. This this very high temperature plasma burns and pits the metal, and (as was discussed with the Arrhenius equation) dramatically increases the rate of oxidation of the surrounding connection. Not only that, but these higher power losses increases the junction temperature and can cause the UL temperature limits to be exceeded. This will be discussed in more detail later, but for now assume that the desire is to be able to detect a connection that increases in resistance by 300% of nominal. From that value, a new voltage drop can be calculated.

$$V = (3 \cdot 0.02) = 0.06 \text{ Volts} \tag{2.48}$$

$$\Delta V = 0.06 - 0.02 = 0.04 \text{ Volts} \tag{2.49}$$

Further, the assumption will be made that due to noise and sampling errors (typically A/D resolution will be specified at no better than a particular percentage of reading or of full scale ± 1 LSB), the voltage and current measuring system must have greater resolution than the smallest detectable change, otherwise a dithering of the LSB could be due to an actual signal change or simply due to noise. Assume that this sensing system has double the sampling resolution required to read the smallest signal change of interest. In other words, to accurately read a 0.04 V change, hardware is needed that can accurately measure at least a 0.02 V change. By dividing this resolution (0.02

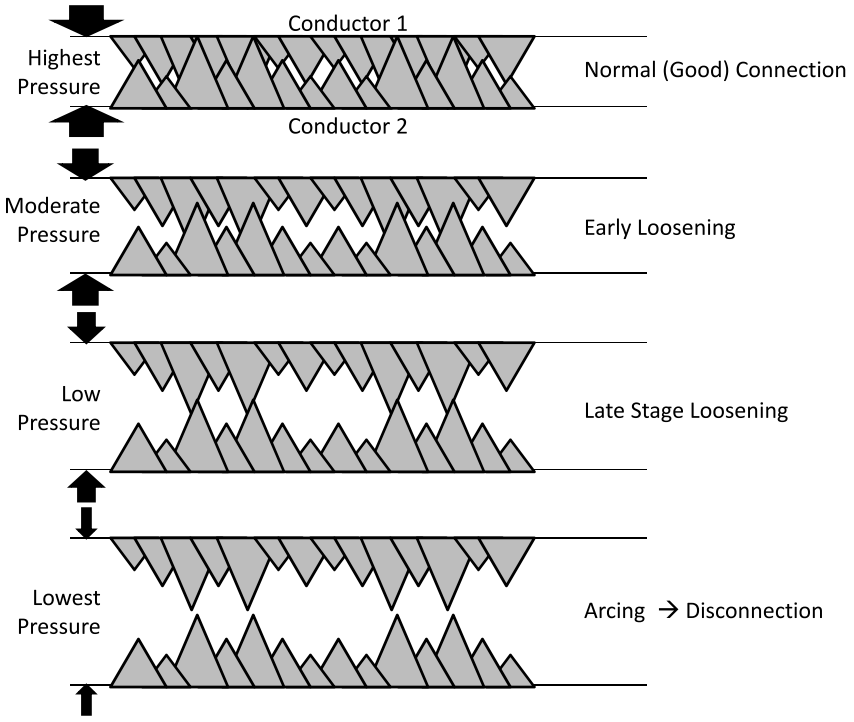

Figure 19: At a microscopic level, surface roughness of two conductors restricts surface area that actually touch between conductors unless sufficient pressure is applied to compress the peaks to allow a greater number of "points" on each surface to touch.

V) into the voltage range (14 000), the number of A/D sampling intervals is obtained that will be required to resolve this smallest unit of interest.

$$\text{Intervals} = \left(\frac{Count_{max} - Count_{min}}{\Delta V/2}\right) = \left(\frac{14400-0}{0.02}\right) = 720000 \tag{2.50}$$

Converting this value (720 000) into the equivalent number of binary bits, begins by solving equations (2.51) through (2.50) for the value of n.

$$2^n = 720000 \tag{2.51}$$

$$log_2(2^n) = n = log_2(720000) \tag{2.52}$$

$$n = \frac{log_{10}(720000)}{log_{10}2} = 19.46 \tag{2.53}$$

According to Equation (2.53) the required A/D resolution must be at least 20-bits. Legacy metering devices (protective relay, IEDs, etc.) may have only provided 10- or 12-bit resolution (or even 8-bit). Higher resolution metering could be installed, however burdening the project costs by installing this level of resolution may not be justified. And consider that as the systems increases in size, several of these higher resolution devices would be needed. And even if these were installed, equations (2.46) through (2.53), predict that more than 20-bits of resolution would be necessary only for smaller changes (~300%) or with at least 200A flowing across a $100\mu\Omega$. In the example below, decreasing the nominal current in half (to 100A) and the percent increase in resistance likewise in half (200%) intuitively requires 4 times the resolution. Equations 2.54 through 2.60 confirms that the required bit count increases from 20 to 22.

$$V = IR = 100 \cdot 100 \cdot 10^{-6} = 0.01 \text{ Volts} \tag{2.54}$$

$$V = (2 \cdot 0.01) = 0.02 Volts \tag{2.55}$$

$$\Delta V = 0.02 - 0.01 = 0.01 \text{ Volts} \tag{2.56}$$

$$\text{Intervals} = \left(\frac{Count_{max} - Count_{min}}{\Delta V/2}\right) = \left(\frac{14400-0}{0.005}\right) = 2880000 \tag{2.57}$$

$$2^n = 2880000 \tag{2.58}$$

$$log_2\left(2^n\right) = n = log_2\left(2880000\right) \tag{2.59}$$

$$n = \frac{log_{10}\left(2880000\right)}{log_{10}2} = 21.45 \tag{2.60}$$

While the resolution must be sufficient to resolve these small changes in voltage drop, this is not the only concern. Consider the meters shown in figure 14 and described in equation 2.35. In these designs, the calculation of the difference in the voltage (and potentially current per figure 15, diagram C) between the "upstream" and "downstream" metering devices only makes sense if the meters capture data at precisely same time. If measurements are taken independently without regard for any time synchronization and too much time elapses between readings, or if the readings are captured at what is believe to be the same time but the time stamp are inaccurate, voltage drop calculation will be flawed since loads may have switched and the previous V_1/I_1 (which measured impedance from that point downstream to the load) while have changed to some completely different ratio. If that completely different ratio (Z_1) is subtracted with another ratio (Z), the samples from each are mismatched and uncorrelated. The problem is worsened the further the two meter's time clocks are allowed to drift one relative to another.

2.3.5 Obtaining Accurately Time Stamped Data

Coordination of the simultaneous capture of data can be accomplished either from a centrally managed station transmitting a "capture now" command sent as a one-to-many broadcast, or alternatively triggered at the IEDs at on a prearranged time. In other words, the IEDs would have a stored program that tells them to capture data a pre-arranged times. Any time drift between clocks causes samples to be misaligned resulting in additional noise. Figure 20 shows how the instantaneous calculated value of resistance R becomes much more uncertain. Interestingly though, the

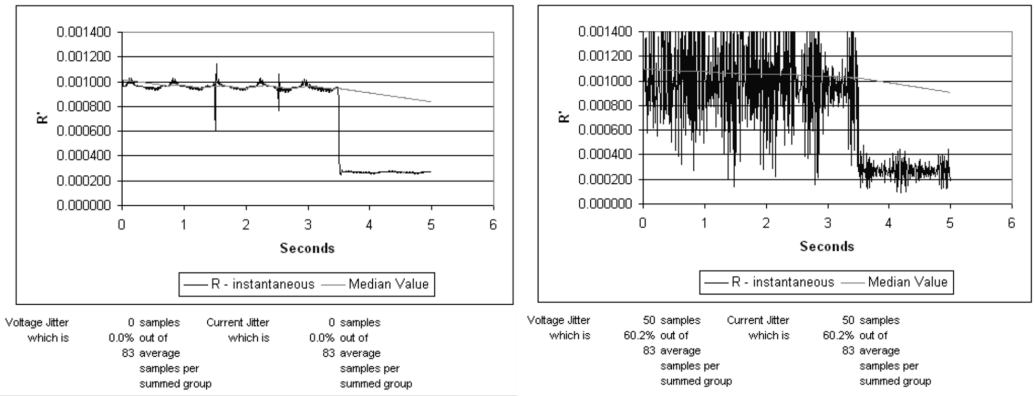

Figure 20: Random time stamp timing differences of the measured values. Left graph shows median / mode filter with accurate time stamping. Right graph shows calculation when signal received with $\pm 60\%$ timing uncertainty

median / mode filter applied to this noisy data continues to track the actual value of resistance with two caveats:

- Initial value selection is based on the first sampled value. If this value is corrupted by substantial noise due to time jitter, then the algorithm will require additional time to settle to a final value
- If the jitter is not zero-mean, then the baseline calculation will never converge to the correct value of impedance. However, this value becomes the new baseline and the system will continue to detect deviations correctly from this new baseline.

To insure the IEDs maintain the same time reference, they are synchronized to a common clock. While it isn't explicitly required that IED clocks be synchronized to atomic time, atomic time is commonly available through a variety of means and protocols (IRIG-B, NTP [65], PTP [5], cellular time server, GPS receiver, and LW or SW receivers for DCF77, CHU, WWV, and MSF [55]) with straight-forward (though not necessarily low-cost or low-power) methods for synchronizing geographically diverse clocks to high accuracy ("Stratum" level timing [13]). Once the individual clocks are set to the same time, a mechanism must exist to allow all devices to capture data at the same time.

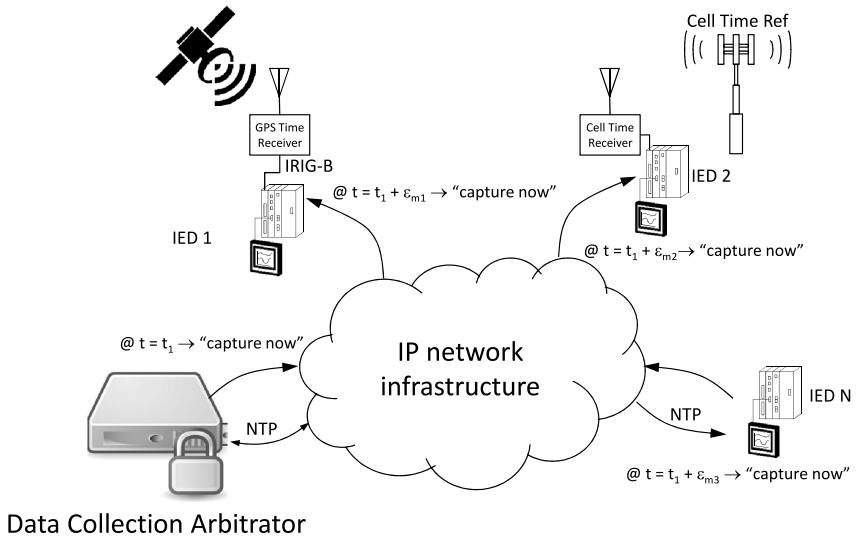

Figure 21: One-to-many capture request experiencing multiple delays varying by location and device

Figure 21 shows one method of transmitting a request from a Data Collection Arbitrator (DCA) to a group of IEDs. The request is received at the various IEDs at different times due to varying network delays (ε_{mx} where $x = 1, 2, \ldots n$), changing the meaning of "now".

Figure 22 shows this concept with each IED receiving the digitally encoded "capture now" signal delayed through different portions of the network (shown in the z-domain). To work around this problem, two solutions that are suggested to insure that all nodes capture data at the same time.

2.3.5.1 Periodic Background Capture Method Referencing figure 23, this method works by having the IEDs periodically write the necessary time stamped data at pre-arranged intervals into a circular buffer (data accumulates until memory is exhausted at which point the oldest data is overwritten). Figure 23 shows requested capture time $x(t)$ only occurring at the top of a second. In this scheme, either a request is made for data in the past, or sufficiently far in the future to allow all nodes sufficient time to receive the request and be ready to capture at the time requested. While the delay from when the message actually arrives at each IED is variable and non-deterministic, the embedded message is the same. As long as the IED's circular buffer still contains the data for

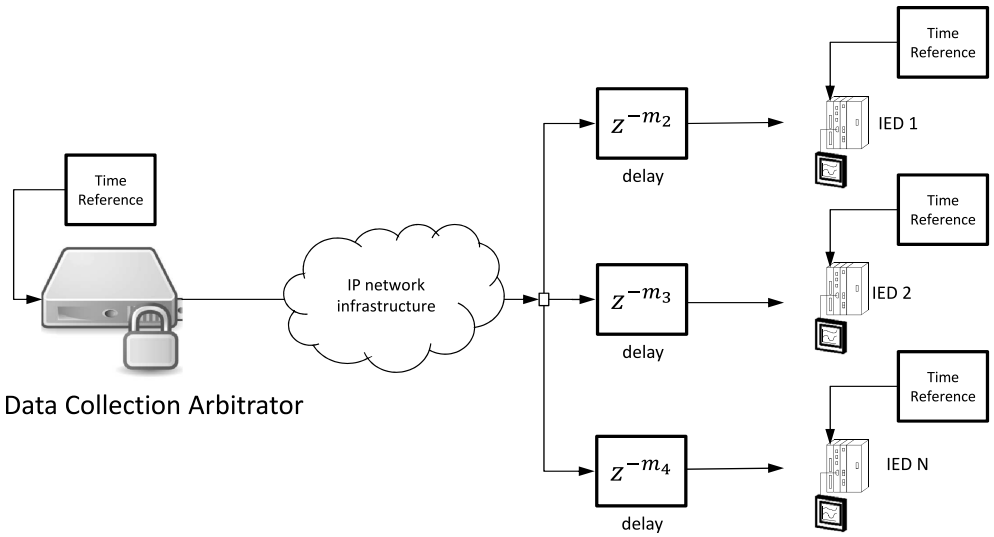

Figure 22: Digital data streams from host to remote IEDs can be modeled as passing through variable time delays (shown in z-transform representation of z^{-m_x})

the requested time slot, that data is returned. As the magnitude of variability in network delays increases, requests for future captures must be delayed sufficiently long to allow the slowest network path to transmit the request to that IED. As shown in figure 24, that may require skipping to the next or even later synchronized sample window.

While figures 23 and 24 show capture windows synchronized to the top of each second, if an IED has been programmed to only capture data at the top each minute or hour, memory requirements are reduced allowing even devices with modest memory or power resources to still provide precisely time synced data. A disadvantage of this method is that data collection at time points other than pre-arranged points will not be available. This makes it difficult to "go back in time" to look at a specific event occurring at an specific time (although if the device is programmed to capture on exception and time stamp, it may have been possible to capture a wide-area event, assuming *each* device in the wide area likewise captured the same event).

2.3.5.2 Continuous Pre-Trigger Buffer Method To work around the problem of not being able to obtain waveform captures from diverse devices at any arbitrary time of interest, all at the

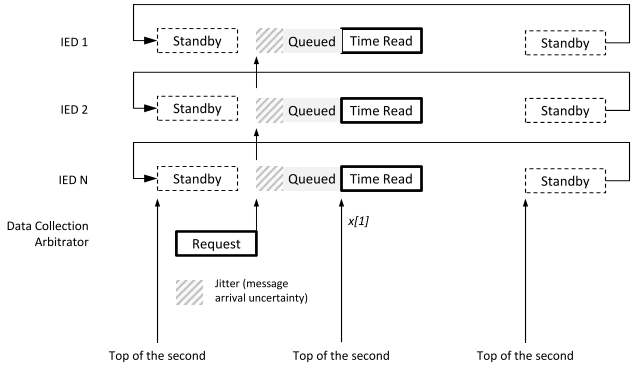

Figure 23: Periodic background capture method. Capture on next available time window

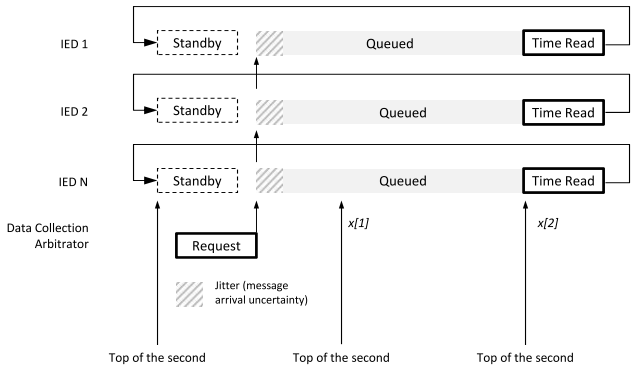

Figure 24: Periodic background capture where network latency to one or more nodes requires delaying to a subsequent available time window

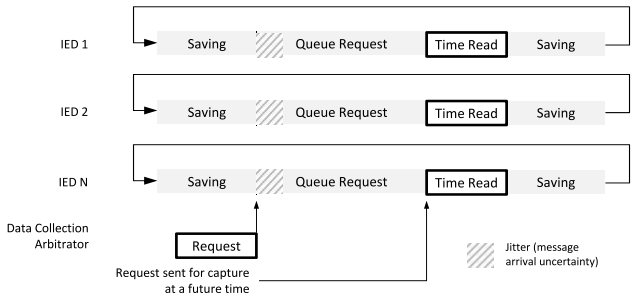

Figure 25: Continuous background capture. Knowledge of worst case latency until message is received is factored into how far in the future a request for a data capture is made.

same time (even if an individual device did not trigger on an event), another method is proposed – continuous pre-trigger buffer method. As with the periodic background capture method, a circular buffer operates to collect waveform data. However, unlike the periodic background method, this method collects data continuously as rapidly as possible with no intentional (or at least much smaller) delays between captures (figure 25).

Each IED continues to capture and time stamp data collected, with the amount of data based on the number of channels trended, the bits allocated per sample and the sample (A/D quantization) rate. When a request containing the desired time window over which to capture data is transmitted to the IEDs from the DCA, the IED looks up the start position within the buffer and copies the request block to non-volatile memory and then transfers it to the requester (DCA). While the request experiences variable delays in reaching the IED (shown as the hatch pattern marked "jitter" in figure 25), as long as the circular buffer has the data from the time window requested, it is returned. If some or all of the data has shifted out of the buffer, an error message is returned (optionally along with any portion of the requested data that still remains available).

Each of these methods operates over a channel that has an arbitrary slow throughput and an arbitrary uncertainty / jitter and yet still manages to capture data from widely dispersed IEDs at essentially precisely the same time. The next step is to describe a method of synchronizing all IED (and data acquisition device) clocks to the same time (atomic or other reference).

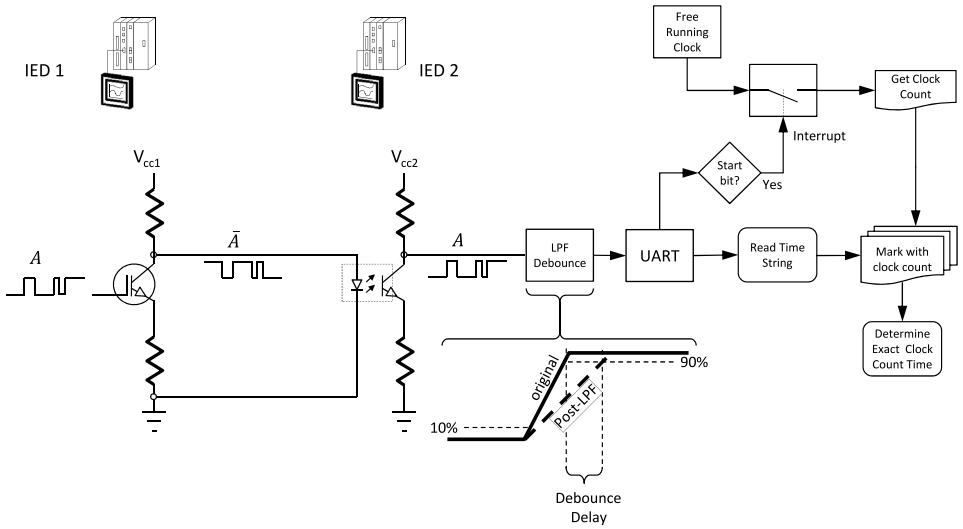

Figure 26: Optically isolated, low cost time sync without requiring connection to atomic time reference

2.3.5.3 Low Cost Time Sync Method As discussed earlier, a common method for synchronizing devices is to use atomic time. For multiple devices mounted within a common enclosure, one cost savings method could be to allow one device to send a time synchronization signal via a digital input/output pair using a 5 Vdc (e.g. the method used by IRIG-B [60]) or 24 Vdc (e.g. DCF-77 [80]). Similar to how cameras used in large multi-camera venues are all frame-by-frame synchronized (known as "genlocking" [67]), a single on-site time reference (not necessarily synced to atomic time, but frequently is) transmits a synchronization signal to each camera over cable or fiber. Differing delays due to cable length are factored to allow nanosecond time-sync resolution. Typically these protocols transmit data at a relatively slow rate, but rely on the receiving station's UART to trigger a system interrupt on the receipt of an incoming start bit of the serial data stream. That interrupt establishes a common marker between both the sending and receiving station, where typically the attached message streaming later will establish the actual time value of that marker. If this trigger signal were sensitive to coupled noise, the resulting storm of interrupts could cause stack or buffer overflow errors, potentially causing the system to malfunction.

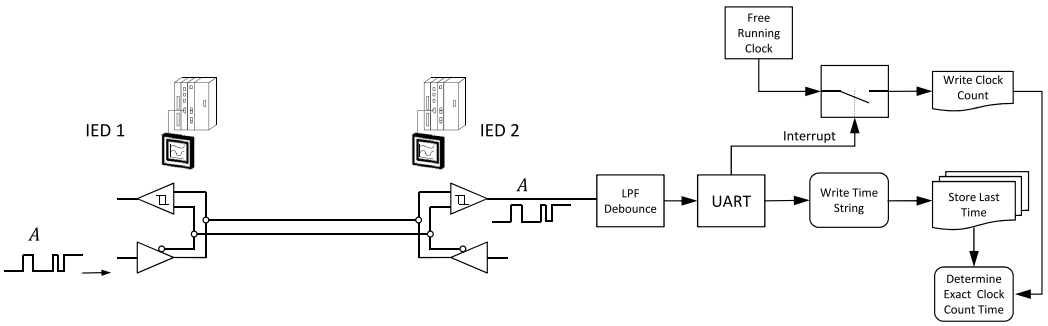

Figure 27: Differential transmission to improve reliability (transceivers also optically isolated)

For this reason, a careful selection of receiver input filtering (de-bounce) and the use of a differential (figure 27) or fiber rather than single-ended (figure 26) connections would be preferred. The analog debounce circuit is typically only a single stage RC filter. To reduce timing drift due to temperature variations, an analog filter with temperature compensated elements (such as metal film resistors and class 1 ceramic capacitors) rather than a digital filter would be recommended. Since a digital filter relies on sampled data, the throughput is related to the sample rate, which for cost reasons, will be kept as low as possible. Since the inbound leading edge of the time signal would arrive between samples, this increases uncertainty of the *actual* arrival time of the sync pulse versus measured time would increase error.

But an analog low pass filter adds delay too (see figure 26), so such delay from the DCA to the IED would need to be factored out. However, for a known voltage and when operated within a known temperature range with low drift components, this delay would be deterministic and could be factored out by having a node realize that the pulse was actually transmitted xx microseconds prior to the time of detection and could adjust the time stamp accordingly.

Many of the legacy devices do include support for triggering a waveform capture via a network message, however, many do not support this message as a multi-cast broadcast. Even for those devices that do support a multi-cast/broadcast waveform capture command, the latency from message reception to action may be plagued with timing jitter. IEDs consider their protection functions the highest priority. Depending on how quickly their serial port is serviced, it would not be unexpected for an IED to buffer a request while other, more “important” processing was completed. This delay

may very well be non-deterministic, due to uncertainties in ISR servicing delays, means that the delay could not be predicted, except with statistical measures (potentially improved through over-sampling discussed in section 4.1.5). This complicates the process to insure that captures occur at all parts of the network at the same time.

Consider that only ± 1 ms of jitter (uncertainty) corresponds to ± 22 deg of phase error at 60 Hz.

$$\phi = \pm 0.001 \text{ sec} * \frac{60 \text{ cycles}}{1 \text{ sec}} * 360 \frac{\text{deg}}{\text{cycles}} = \pm 21.6 \text{ deg} \tag{2.61}$$

Since arcing contacts dissipate real power, this can be modeled by a change in resistance. While normally resistance could be calculated by multiplying the measured impedance by the power factor, with a ϕ shifting by ± 21.6 deg, that calculated value of R would be shifted correspondingly. Consider a system with an X/R ratio = 4.9 (20% PF):

$$\phi_1 = \tan^{-1}(4.9) = 1.37 \text{ rad} = 78.46 \text{ deg} \tag{2.62}$$

$$\text{Power Factor} = \cos(\phi_1) = \cos(78.46 \text{ deg}) = 0.2 \tag{2.63}$$

$$\cos(78.46 \text{ deg} + 22 \text{ deg}) = -0.182 \tag{2.64}$$

$$\% \text{ diff} = \frac{0.2 - (-0.182)}{0.2} = 191\% \tag{2.65}$$

Equation 2.65 predicts that a 22 degree (1 ms) uncertainty results in an error in resistance of nearly 200%! Consider that even a detection of 100% change in resistance would require twice the timing resolution. Begin by considering a circuit with a total impedance $Z = 1\Omega$ with an $X/R = 4.9$

$$Z = 1\angle 78.465...\text{deg} = 0.19996 + j0.979804 \tag{2.66}$$

If the value of R increases by 100%, then:

$$2Z = 2\,(0.19996) + j0.979804 = 0.3999 + j0.979804 = 1.05828\angle 67.7965...\text{deg} \tag{2.67}$$

The equivalent time offset corresponding to this phase shift is calculated as:

$$(\phi_1 - \phi_2) * \frac{1 \text{ cycle}}{360 \text{ deg}} * \frac{1 \text{ sec}}{f} = t_{offset} \tag{2.68}$$

$$(78.46 - 67.80)\,\text{deg} * \frac{1 \text{ cycle}}{360 \text{ deg}} * \frac{1 \text{ sec}}{60 \text{ cycles}} = 0.000494 \text{ sec} = 0.49 \text{ ms} \tag{2.69}$$

Clearly a method that only relies on a phase angle measurement with a time jitter no better than $\pm$1ms will be insufficient to resolve even a 100% change in resistance on a $\sim 1\Omega$ circuit. If this kind of timing accuracy is required to detect a 100% change, what is required to measure a 1% change? As can be inferred from equations 2.61through 2.69 immediately above, the accuracy required would be, from inspection, 1/100th of 0.49 ms or 4.9 μs.

The important point to remember is that phase angle measurements are being calculated at dispersed meters. Certainly if a single meter (with a single time reference) were used, the uncertainty in timing could be better. However, a general purpose method must be able to operate across a network (TCP/IP LAN or WAN) with geographically dispersed metering devices. Factor in, also, the operating system of each device, the additional (and potentially variable) overhead of encrypting variable length messages and the problem become more difficult (figure 28 and more detailed in figure 29).

Because of these concerns, it will be important for an algorithm to operate within an environment that has a level of uncertainty in the timing accuracy, if existing legacy devices are to be considered for use. For this reason, three-phase testing using actual power system data, the testing was performed with IEDs that included real-time clocks synchronized to within approximately $\pm$1 ms ($\pm$22 deg on 60 Hz signal) of atomic time. Reference will be made as to which data was collected via simulation, bench testing with instrumentation (typically to within 1 μs timing resolution or better and three-phase power system data (1 ms timing resolution).

But as discussed in figures 23 through 25, the algorithm must function where network delays are variable. With internal clocks set to actual time $\pm$1 ms, the variable delays seen in figures

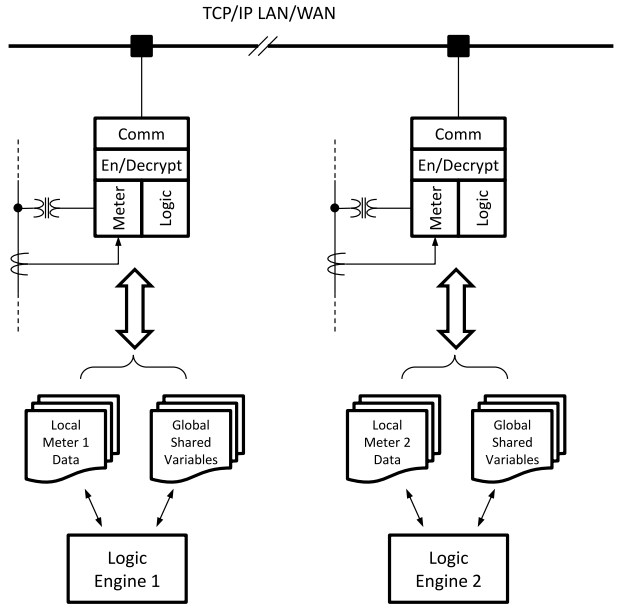

Figure 28: Geographically dispersed devices synchronizing across a network.

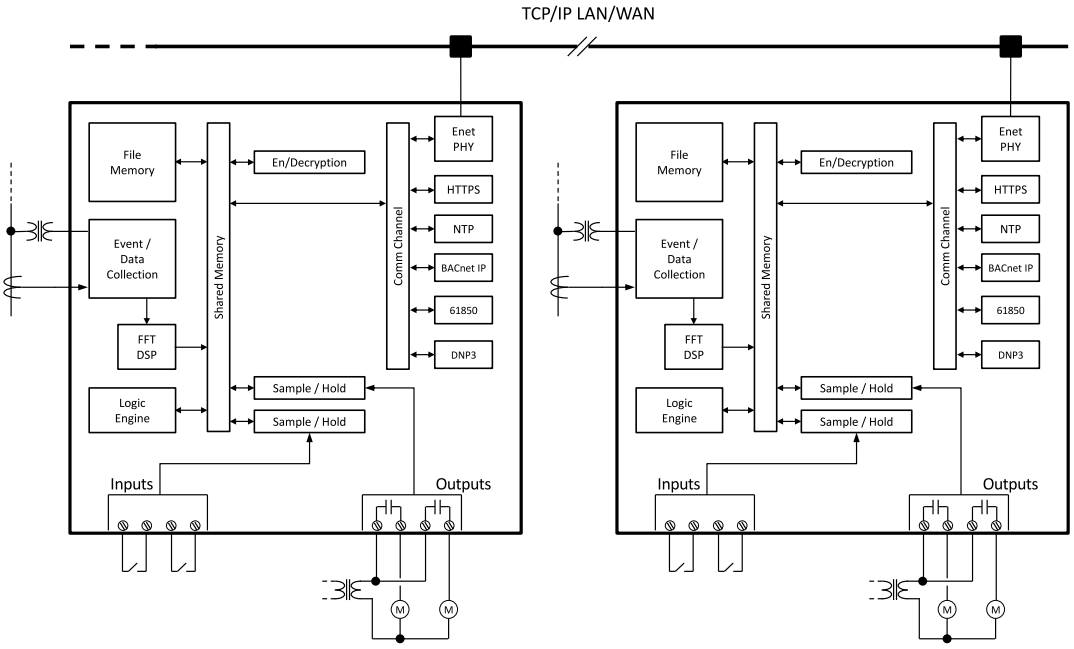

Figure 29: Potential Hardware Implementation Model

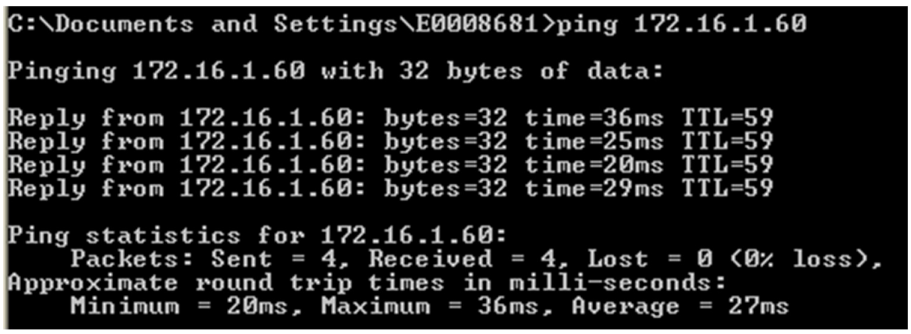

Figure 30: Network latency and jitter - 25 miles

30 and 31, when transmitting ICMP PING messages across a corporate LAN, showed substantial timing inconsistencies packet to packet.

In 30 the round trip delay showed 36 ms max latency with 14 ms of jitter (defined here as the range of latency values measured) for two nodes that are only 20 miles apart (Pittsburgh airport area to Cranberry Township Pennsylvania approximately 25 miles away). It may be expected that if a 20 mile separation in nodes results in 14 ms of jitter then two nodes separated 20 times further would experience even more. However, figure 31 shows two nodes separated by 400 miles only experiencing 1 ms of timing jitter between ICMP pings. One cause of the inconsistency can be attributed to differing levels of traffic in and outbound from each node at the time of each test. Normalizing the jitter to traffic effects would better clarify the cause.

However, regardless of the cause of the jitter, the presence and non-deterministic nature of this error is the reason that the methods outlined in figures 30 and 31, or something similar, must be used.

Another issue to deal with is the issue of encryption of data between nodes. Throughput calculations of encrypted data transmission to and from IEDs has been [45] analyzed and conclusions have been made that asymmetrical key encryption burdens legacy IED CPUs more (too) heavily when those IEDs must transmit time critical data. While symmetric key encryption is faster (since both end-nodes have a common shared secret with no need to create the complex prime number factoring problem on the fly), the concern is that this shared secret could be discovered and the data compromised. As these IEDs frequently are monitoring and protecting critical infrastruc-

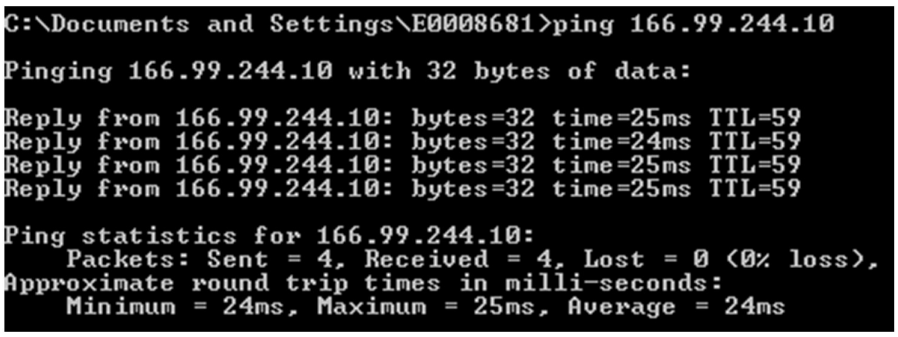

Figure 31: Network latency and jitter - 400 miles

ture, this is a problem that must be addressed. The authors of that paper recommend including a second shared secret "underneath" the first. Since this second shared secret would never be used except during situations where the first shared secret needed to be replaced, it would be much more difficult to discover.

More modern IEDs now include processors that include dedicated on-board encryption hardware so the concern against asymmetric key encryption can be reduced. Note, that key type and length must be chosen commensurate with the required level of secrecy for the data. As of the date of this writing, the SHA-1 160-bit hash algorithm is expected to have been compromised by determined nation-states, and is no longer secure. Higher security cryptographic hash functions are available (SHA-2, SHA-3), but these require even more computational resources.

The system designer is advised to consult with knowledgeable domain experts who have expertise in not only cybersecurity protocol suites, but also their implementation in hardware including time / overhead profiling when used in algorithms in order to understand the consequences of their use with regards to throughput and determinism.

However, as stated before, this variability will be mitigated using one of the techniques shown in figures 23, 24 or 25.

3.0 RESOLUTION ENHANCEMENT TECHNIQUES

3.1 MULTIVARIATE ANALYSIS

One technique that will be described below to detect change in a more sensitive manner is to monitor not only the signals, but also secondary effects, or combinations of those signals and secondary effects. Multivariate analysis examines patterns of interaction between signals that many not be immediately evident from examining signals individually. A simple example is the derivation of bus impedance using current, voltage, (plus potentially harmonic content and ambient temperature) from two separate devices that can provide an upstream (V_1) and downstream (V_2)voltage measurement. Either rms or instantaneous (see Appendix A) values of voltage and current can be ratioed, then the difference taken to resolve a measure of Z_S, as shown in equation 3.1 and figure 32.

$$Z_S(\omega) = \frac{\Delta V(\omega, T)}{I(\omega)} \tag{3.1}$$

Such a signal $(Z_S(\omega))$will be largely unusable as calculated from this equation due to quantization errors, noise, non-linearity (switching) and other artifacts, but the equation provides a basis for explaining how those problems will be eliminated via additional filtering techniques that will be applied.

Consider that the calculation of the source impedance, Z_S, is derived using knowledge of voltage drop, current and temperature, with the voltage drop and current, in turn, being a function of the particular frequency of the current and voltage. While the essential mathematics of solv-

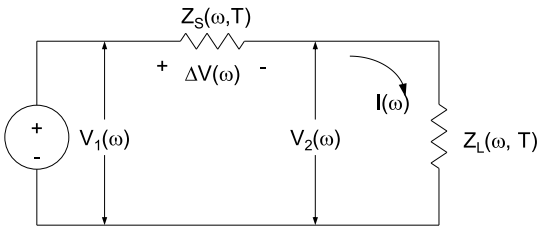

Figure 32: Simple multivariate system

ing these equations are well known, the practical limitations on the sensing methods available in legacy equipment limits the resolution of the impedance calculation. to not being sensitive enough to detect degradation (unless something is done to increase this resolution).

To measure a sufficiently small change in impedance, the goal of this research has been to develop methods, filters and algorithms to examine the signal, remove the noise and provide sufficient resolution to detect accurately enough the ΔV, and I to resolve Z and eventually R to notice degrading connections.

3.1.1 Multi-Frequency Impedance Analysis

One method for achieve greater resolution is to measure this impedance at multiple frequencies, then combine the readings in some meaningful method. While the power system may operate at a nominal power frequency, superimposed are harmonics of that frequency plus switching transients (which to some level of resolution can be modeled as step functions) and noise. While normally considered undesirable (many energy metering systems work to remove this noise to improve metering accuracy), the method outlined here will instead use this noise as information.

One step is to create multiple simultaneous readings (at different frequencies) to provide a more complete picture of the conductors connecting two nodes. This measurement technique calculates the Z and R at different frequencies. Since reactance of the circuit will cause measurable attenuation of the higher frequencies, plotting this attenuation relative to the series resistance at each frequency provides insight into the magnitude of X. In other words, the decline in the energy contained in those frequency bands allows the calculation of an X/R ratio. When combined

with measurements of changes in R (due to skin effect [30, pg 2-24]) into a non-linear equation and solved numerically / iteratively, this technique provides additional information regarding the location of a fault.

3.1.1.1 RMS Decomposition of Harmonic Impedances

Consider that each harmonic current produces a voltage drop across the nodal impedances Z_{xx} as shown in figure 33 or more simply as $Z_S$in figure 32. The KVL equation across $Z_S(\omega, T)$ becomes:

$$V_1(\omega) - V_2(\omega) = I(\omega)(R_S(\omega) + jX_S(\omega)) \tag{3.2}$$

Rewriting:

$$I(\omega) = \frac{\Delta V(\omega)}{R(\omega) + jX(\omega)} \tag{3.3}$$

Summing each harmonic contribution as an rms value and substituting in the values from equation (3.2)

$$I_{rms} = \sqrt{\frac{I_1^2 + I_2^2 + I_3^2 + \cdots + I_N^2}{N}} \tag{3.4}$$

$$I_{rms} = \sqrt{\frac{\left(\frac{\Delta V(\omega_1)}{R(\omega_1)+jX(\omega_1)}\right)^2 + \left(\frac{\Delta V(\omega_2)}{R(\omega_2)+jX(\omega_2)}\right)^2 + \cdots + \left(\frac{\Delta V(\omega_N)}{R(\omega_N)+jX(\omega_N)}\right)^2}{N}} \tag{3.5}$$

$$I_{rms} = \sqrt{\frac{\sum_{n=1}^{N}\left(\frac{\Delta V(\omega_n)}{R(\omega_n)+jX(\omega_n)}\right)^2}{N}} \tag{3.6}$$

Performing a Fourier decomposition of each of the individual harmonic currents and voltages allows for the derivation of the $Z(\omega_n)$ at each frequency component.

3.1.1.2 Derivation of Conductor Resistance at Frequency

Note that the effect of frequency on the resistance (skin effect) of wire (round conductors) can be derived using Bessel functions and is shown in equation 3.7) [9]. The surprising complexity (explaining the need for Bessel functions) is related to the complex relationship of conductor skin depth (which is not really a depth, rather a gradient) due to the eddy currents established by the circulating currents within the conductor, each at a different frequency, then superimposed to create the equation for the skin "depth". The equation for this effective resistance as a function of frequency is shown in equations 3.7 through 3.10:

$$R_{eff} = \frac{2R_s}{\pi\left(1-e^{-r/\delta}\right)\left(2r-\delta\left(1-e^{-r/\delta}\right)\right)}\,\Omega/\mathrm{m} \tag{3.7}$$

And:

$$\delta = \frac{1}{\sqrt{\pi f \mu \sigma}} \tag{3.8}$$

And:

$$R_s = \frac{1}{\sigma\delta} = \sqrt{\frac{\pi f \mu}{\sigma}} \tag{3.9}$$

Therefore:

$$R_{eff} = \frac{2\sqrt{\frac{\pi f \mu}{\sigma}}}{\pi\left(1-e^{-r/\left(\frac{1}{\sqrt{\pi f \mu \sigma}}\right)}\right)\left(2r-\delta\left(1-e^{-r/\left(\frac{1}{\sqrt{\pi f \mu \sigma}}\right)}\right)\right)}\,\Omega/\mathrm{m} \tag{3.10}$$

Where:

R_{eff}	Effective resistance at frequency f
R_s	Resistivity at surface of conductor (Ω)
r	Radius of round wire (m)
δ	Skin depth (defined as the point where current density has dropped to a value of $1/e$ times the magnitude of the current density at the surface of the conductor)
f	Frequency (Hz)
μ	Permeability of conductor material (H/m)
σ	Conductivity of conductor material (S/m)

Note that the definition of δ is defined as the value that results in the current density in the conductor to drop to a value $1/e$ of nominal or:

$$J = J_S e^{-d/\delta} \tag{3.11}$$

$$J = J_S e^{-1} \text{ when } d = \delta \tag{3.12}$$

Where:

J	Current density (ac) within conductor at depth
J_S	Current density at surface of conductor
d	Depth within the core of the conductor

Combining these equation with the (primarily inductive) reactance of the power distribution circuit, the complete equation is derived as equation :

$$Z_{eff}(\omega_1) = R_{eff}(\omega_1) + j\omega_1 L \tag{3.13}$$

By solving for the change in the ratio of $X(\omega_n)/R(\omega_n)$, estimations for R and X can be derived without knowledge of timing (phase angle). This is important since it reduces or eliminates the need for accurate time stamping at each device, further reducing the cost of the installation (since legacy metering devices may have little or no time stamping capability). Oversampling (see section 4.1.5) is done to insure that random noise in the calculated values of R_{eff} are minimized.

3.1.1.3 Back Substitution of Admittance Matrix With this knowledge of a new method of calculating $R_{eff}(\omega_1) + j\omega_1 L$, consider that these derived impedances are represented as the node-to-node impedances as shown in figure 33 and the equivalent admittance matrix as shown in equation 3.14. Any number of well-known linear algebraic techniques can be used to simplify these matrices to solve for the unknown impedances or admittances based on measured or calculated node voltages and currents (LU / triangular factorization, Kron reduction, Gaussian elimination, etc.), but the real key in achieving the necessary resolution goes beyond simply factoring and solving for the nodal values.

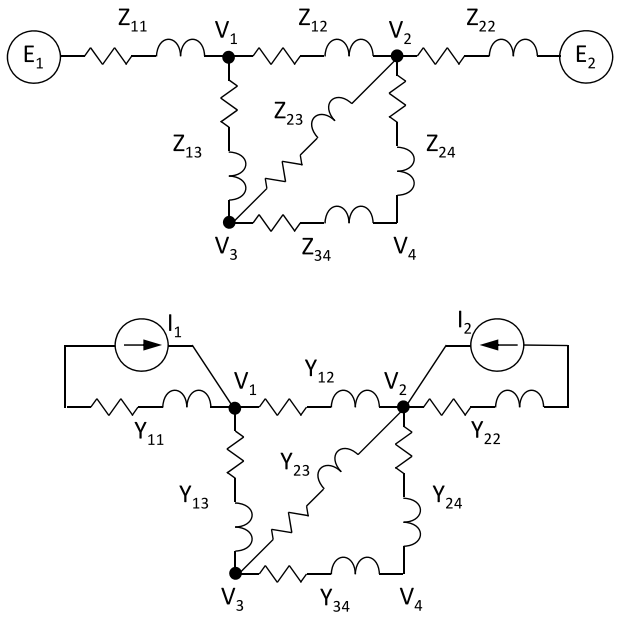

Figure 33: Example system with meshed impedances

To be able to use the raw data available from legacy metering, additional oversampling, noise shaping and statistical processing is required convert conventional state estimation into a tool that allows much higher resolution measurements of those node impedances.

Before those additional methods are applied, a quick review is presented of mathematical analysis for the system shown in figure 33. This figure is written mathematically as equation 3.14.

$$\begin{bmatrix} I_1 \\ I_2 \\ 0 \\ 0 \end{bmatrix} = \begin{bmatrix} Y_{11}+Y_{12}+Y_{13} & -Y_{12} & -Y_{13} & 0 \\ -Y_{12} & Y_{12}+Y_{22}+Y_{24}+Y_{23} & -Y_{23} & -Y_{24} \\ -Y_{13} & -Y_{23} & Y_{12}+Y_{22}+Y_{24} & -Y_{24} \\ 0 & -Y_{24} & -Y_{24} & Y_{12}+Y_{22} \end{bmatrix} \begin{bmatrix} V_1 \\ V_2 \\ V_3 \\ V_4 \end{bmatrix} \tag{3.14}$$

The well known short hand notation for equation 3.14 is written as equation 3.15 and will be used later as the anchor of this noise removal processing:

$$\mathbf{I} = \mathbf{Y}_{bus} \cdot \mathbf{V} \tag{3.15}$$

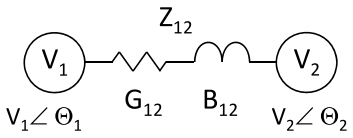

Figure 34: Simple 2-source power flow diagram

In legacy systems recall that $\mathbf{Y}_{bus}$ is derived from measuring the voltages and phase angles at each end of a bus, along with real and reactive power flow through the bus and solving:

$$Q_i = \sum_{k=1}^{N} |V_i|\,|V_k|\,(G_{ik} sin\,(\Theta_{ik}) + B_{ik} cos\,(\Theta_{ik})) \tag{3.16}$$

Then recognizing that by knowing the phase angle and conductance G and susceptance B between each node permits writing the equation that solves for each element (Y_{ik}) in the $\mathbf{Y}_{bus}$ admittance matrix, where:

$$Y_{ik} = G_{ik} sin\,(\Theta_{ik}) + B_{ik} cos\,(\Theta_{ik}) \tag{3.17}$$

However, as outlined in equations 3.2 through 3.13, an iterative process of comparing measured R and X values to one another at different frequencies is another, perhaps more practical (although uncommon) method for deriving the phase angle. In order to obtain the necessary resolution, these calculations, too, are over-sampled, and statistically processed using noise shaping to derive the higher resolution than would normally not be available from legacy metering.

Solving admittance matrices and applying that knowledge to determine unknown power system states are well known techniques [24], and researchers have built on this foundation using various statistical modeling techniques [83, 17, 18, 77] to improve accuracy for transmission line state-estimation.

What has, apparently, been less well researched, is using the signal processing techniques outlined here (derivation of $R(\omega)$ and use of harmonic energy to derive complex frequency without phase angle measurements, etc.) to remove the noise from this state estimation problem further

assisted with oversampling and new filters proposed here. The explanation of these techniques is the central theme of this analysis and this document.

4.0 NOISE CHARACTERIZATION AND REMOVAL

4.1 OBTAINING ENHANCED RESOLUTION

A key challenge when attempting to use data from legacy metering is overcoming the problem of insufficient resolution to measure very small changes in resistance.

4.1.1 Deriving Nominal Junction Resistance

Consider that in Table 13 within UL891 (Standard for Safety – Switchboards [48]) it is stated that a pressure terminal connector for externally field installed conductors that exceed 125 amperes cannot have a temperature rise of greater than 50 deg C above ambient (defined as 40 deg C). Furthermore, section 6.2.6.20 of this same standard requires that a switchboard or field wiring circuit rated more than 125 A must use conductors sized for 75 deg C ampacity. Since most modern cable insulation systems are rated 90 deg C, operating the cable such that the operating temperature is no more than 75 deg maximum temperature rise means the current flowing is less than the rated ampacity of the cable (when operated at rated temperature of 90 deg C). Such a cable can be considered to be oversized for the circuit.

This means that in most cases, the terminated conductors, when carrying rated current, will be cooler (75 deg C) than the terminal point to which they are connected (50 + 40 = 90 deg C). In these cases, the cables and junction (terminals) effectively act as a heat sink for the switchboard. During the design and testing of a switchboard, manufacturers expect that these cables be present and that the terminations are made with an appropriately low resistance (recall figure 19) and therefore expect that the cables will provide cooling (via conduction) during operation.

To insure properly sized cables are used, contractors and installers refer to the National Electrical Code (NFPA 70 NEC [11]) to size cable ampacities that meet the 75°C temperature rise limit. Specifically, NFPA 70, Table 310-15(B)(16) (formerly table 310.16 prior to the 2014 code) provides the minimum required conductor sizing for cables that are routed to the switchboard via conduit. The important point is that neither UL nor the NFPA / NEC specifies the acceptable resistance of a termination. Rather, the key related specification is the maximum temperature of that conductor termination.

For an example of the is importance of designing a resistance measuring system that can provide sufficient resolution to detect a "good" versus a "bad" junction, consider a 200 A circuit, consisting of 50 meters of 4/0 AWG copper conductor terminated by two lugs, each rated for 200A. Referring to UL/IEC standard 60947-7-1 ([50]) and figure 35, a properly terminated connection is defined as having no more than a 3.2 mV drop. With a 200A rated lug, the equivalent impedance is calculated:

$$\frac{V}{I} = Z = \frac{0.0032\ \text{V}}{200\ \text{A}} = 16\mu\Omega \tag{4.1}$$

As this is an absolute upper limit, actual impedances will be less. Laboratory tested 200A lug connections have been measured (see figure 35) as $R_{lug1(good)} = R_{lug2(good)} = 10\mu\Omega$. As electrical equipment purchased for commercial construction projects is heavily discounted, the equipment typically does not provide additional margin above its published ratings. This means that the terminals are operating at close to the allowed maximum temperature even when they are clean, tight and corrosion free. Under such circumstances, *any* increase in resistance increases losses, potentially raising voltage drop and temperature above the maximum permitted by UL/IEC limits. Since the correlation between resistance and temperature is complicated (recall the need to solve a quartic equation 2.25), for this case a very conservative assumption is made that a failing connection occurs when a resistance of the junction increases to 300% of nominal. In this example, such a situation occurs when its resistance equals 30 $\mu\Omega$, which is an increase of 20 $\mu\Omega$ over nominal levels measured in the lab. As UL/IEC standard 60947-7-1 ([50] and per equation 4.1) establishes a maximum acceptable resistance for this 200A termination at $16\mu\Omega$, a test value of $30\mu\Omega$ would exceed that limit and so would be considered a failure that, ideally, should be detected by the method being proposed.

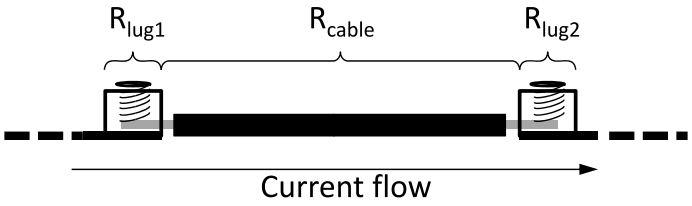

Figure 35: Example conductor terminated at two lugs.

4.1.2 Temperature Effects on Measured Resistance

But consider that the existing metering wired as shown in figures 15 and 16 is called upon to measure not only the resistance of the termination, but also the entire set of the conductive path between the two voltage sensing points. Understanding this, what percentage of the resistance of the total conductor would the changed by a 20 $\mu\Omega$ increase in one termination?

The solution begins by referring to figure 35, and noting that the end-to-end resistance is defined as $R = R_{lug1} + R_{cable} + R_{lug2}$ where R_{cable} consists of 50m of 4/0 AWG ($0.207\Omega/\text{km}$ [7]) copper wire where:

$$R_{cable} = 50\text{m} * 0.207\Omega/\text{km} * \frac{1\text{ km}}{1000\text{ m}} = 0.01035\Omega \tag{4.2}$$

$$R_{good} = R_{lug1(good)} + R_{cable} + R_{lug2(good)} = 2 * 0.00001\Omega + 0.01035\Omega = 0.01037\Omega \tag{4.3}$$

If we consider that the rightmost lug in figure 35 is beginning to fail, then that is describes as in equation 4.4.

$$R_{bad} = R_{lug1(good)} + R_{cable} + R_{lug2(bad)} = 10\mu\Omega + 30\mu\Omega + 0.01035\Omega = 0.01039\Omega \tag{4.4}$$

$$\%\text{ diff} = \frac{R_{bad} - R_{good}}{R_{good}} = \frac{0.01039 - 0.01037}{0.01037} = 0.19\% \tag{4.5}$$

However, even more of a problem is that most legacy meters do not offer even that level of repeatability, resolution or accuracy to measure such small changes in voltage drop, phase angle and current. As such, they will not be expected to be able to resolve such a small resistance change. When impedance values are computed from such low resolution hardware, the result is as shown in figure 38.

What was discovered though, was that the solution to solving these problem is to recognize that since, over some short-enough (time-invariant) period, the underlying physics of the system do not change and therefore by characterizing the signal as being corrupted by uncorrelated noise it is possible to statistically analyze the signal to remove that noise. In fact, the presence of this uncorrelated noise tends to move the underlying measurement across more bits of the A/D which offers other benefits (that will be discussed in section 4.1.5).

Furthermore, since current is measured, if the parasitic heating of the conductor due to the current were calculated, this too could be factored out. Finally, since most junction failures are rare, it stands to reason that the likelihood of a simultaneous three-phase degradation (of precisely the same amount of degradation) is lower than the likelihood of a single junction degrading. On three phase systems the impedance on each phase is calculated independently. Degrading junctions on one phase appear as outliers from the per-phase impedance trend plots of the other two phases. While certainly this technique has applicability on single-phase or dc systems too, having a three-phase system provides this extra measure of analysis capability to separate degrading junctions from other external effects.

4.1.3 Normalizing Conductor Characteristics by Temperature

This small amount of resistance change (equation 4.5) is even further masked by normal temperature changes within those conductors and termination. Frequently power systems experience change in current flows. Since heating energy dissipated within the conductor is proportional to the square of the current $\left(P = I^2R\right)$, the temperature swings can range from ambient (no current), to temperatures approaching UL limit (75 deg C). The higher temperatures, in turn, increase the resistance, causing even more energy dissipation (assuming the current remains constant). The need to derate the current ampacity of the conductors to compensate for this recursive increase (current

increase causing an increase in temperature causing an increase in resistance, causing an increase in temperature...) has been recognized and documented in the NEC [11]. In article 310.15 [Ampacities for Conductors Rated 0-2000 Volts](B)(2), and 310.60 [Conductors Rated 2001 to 35,000 Volts](B)(4) a correction factor to compensate for changing conductor temperatures is included.

Higher temperatures increase resistance, and therefore induce greater line losses, (which recursively produces even higher temperatures). These induced higher temperatures deplete the margin, both between the conductor temperature and the insulation temperature rating as well as conductor temperature and UL termination limits. This lowers available conductor ampacity. While this equation cannot be used directly in our normalization function, the theory underlying this equation formed the basis for the solution to the problem. For reference, the NEC defines the reduction current ampacity of a conductor in equation (4.6).

$$I^{'} = I\sqrt{\frac{T_c - T_a^{'}}{T_c - T_a}} \tag{4.6}$$

Where:

$I^{'}$	ampacity corrected for ambient temperature
I	ampacity shown in tables (e.g. 310.15(B)(16))
T_c	temperature rating of conductor (^{o}C)
$T_a^{'}$	new ambient temperature (^{o}C)
T_a	ambient temperature used in the table (^{o}C)

An examination of equation (4.6) show that as the temperature $T_a^{'}$ increases (either due to changes in ambient or due to increased temperature which is recursively induced from increased resistance or from increased current which likewise induces this recursive temperature/resistance property), the numerator decreases. This reduces the ampacity rating of the conductor by a value proportional to the square root of that difference divided by a temperature normalizing factor. The equation, while an approximation, is accurate in the range of typical conductor temperatures used in electrical distribution systems.

Note that while this equation hints that cables change resistance, it does not directly provide the compensation factor which our algorithm needs to factor out of the end to end resistance

($R_{cable}$from figure 35). What is needed is a method of factoring out changes in conductor resistance without measuring the conductor temperature directly. The solution to this problem is described in the next section (4.1.4).

4.1.4 Practical Application of Temperature Linearization

Referring to patent [59], several techniques are described to enhance the resolution of conventional (i.e. lower resolution) IEDs, meters and protective relays. The interested reader can find more about this technology [**?**], but to focus attention on the aspect necessary for removing errors due to changing conductor temperature, the technique outlined here first recognizes that the underlying physical properties are not changing sample-to-sample even though the measurement may (will) not be constant. Over some period of time t what is changing, however, are the conductor temperature and the instantaneous magnitude of noise added to the signal.

Conductor temperature linearization is the focus of this section. Essentially, errors due to changing current causing temperature changes can be factored out by returning to the procedure first discussed in 2.2.2, specifically equation 2.25. For example, this equation predicts a non-linear linear relationship between conductor temperature and conductor resistance. As this equation would be difficult to solve (for the reasons mentioned earlier), the fall back perhaps would be to use a temperature sensor to monitor (and normalize) any changes in conductor resistance due to temperature. But adding any sensor adds cost, both in initial capital as well as labor to install and here a separate sensor would be needed for every conductor – even potentially multiple points along the conductor if is possible its temperature would change over its length.

To reduce these costs and effort, another method is proposed.

4.1.4.1 Cable Characterization The previously mentioned simplified method involved performing a least-squares curve fit on experimentally gathered data that correlated conductor temperature rise with conductor current. That method would seem to require extra effort to characterize a particular installation, since wire size, conduit fill, number of wires per conduit and other issues would affect conductor temperature.

Table 3: Maximum Allowable Ampacity for Type THHN Wiring by Conductor Size (Copper)

AWG	mm^2	60^oC	75^oC	90^oC	2nd Order Least Squares Curve Fit
12	3.31	20	25	30	$I_{rated} = -0.0333T^2 + 9.5T - 50$
2/0	67.4	145	175	195	$I_{rated} = -0.0222T^2 + 5T - 50$
250 kcmil	126.8	215	255	290	$I_{rated} = -0.0111T^2 + 4.167T - 75$
500 kcmil	253.4	320	380	430	$I_{rated} = -0.0222T^2 + 7T - 20$
750 kcmil	380	400	475	535	$I_{rated} = -0.0333T^2 + 9.5T - 50$

However, this research discovered a greatly simplified solution. The key turns out to be that while not in a usable form as published directly, the underlying data and calculations needed to solve this problem have already been completed in the National Fire Protection Association's published National Electrical Code [11].

4.1.4.2 Analysis of NEC (NFPA 70) Cable Properties This organization has a central goal in understanding the relationship between conductor temperature and ampacity to recommend cable ampacity limits and reduce the likelihood of fires, in particular, electrical fires. Referring to the most recent National Electrical Code (2014 version), Table 310.15(B)(16), presents the maximum permitted conductor ampacities based on conductor size, type and insulation temperature rating. Other tables place limits on conductor in conduit size and quantity limits and limits on ambient temperature. What isn't presented in these tables are the equations that are curve fit from the field measurements taken to generate these tables.

Therefore, working backward and taking values from this table showing maximum allowed cable temperature rise, versus current and wire type and solving for the second order polynomial curve fit that correlates conductor temperature with the average rms current magnitude passing through that wire, the data shown in Table 3 is summarized.

It is important to realize that the need for precise correlation between current and temperature is not necessary. Indeed, it is likely that the authors included margin so that the conductors would not reach their rated temperature with the published current levels. Instead, what can be learned

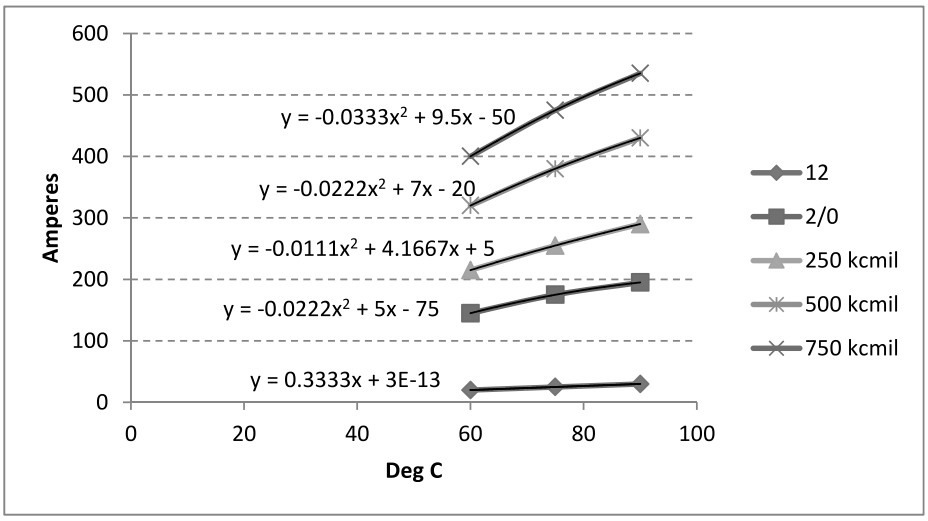

Figure 36: Cross reference, by wire size, of NEC (NFPA 70) current ratings by temperature rating of insulation (based on 30^{O}C ambient)

from these tables is the *relationship* between temperature and current for a particular conductor size, in an particular environment (open tray, metallic conduit, non-metallic conduit, number of conductors per conduit, etc.). This allows a model to be built that predicts the expected *percentage* increase in temperature (which then can be factored into percentage increase in resistance using equation 4.8 listed below). Figure 36 shows the relationships derived from the data shown in Table 3.

Redrawing figure 36 to reverse the x- and y-axes, figure 37 provides the desired orientation to derive the equations correlating predicted temperature rise by current level by wire size[1].

The 2nd order polynomial curve fit equations to each of the graphs shown in figure 37 is summarized in Table 4.

4.1.4.3 NEC Derived PTC Effects The reason the temperature of the conductor is important is that copper and aluminum's positive temperature coefficient (PTC) predictably changes the re-

[1]Data source: 2014 NEC Table 310.15(B)(16) which describes "allowable ampacities of insulated conductors rated up to and including 2000V, 60 deg C through 90 deg C, not more than three current carrying conductors in raceway, cable or earth (directly buried) and based on ambient temperature of 30 deg C.

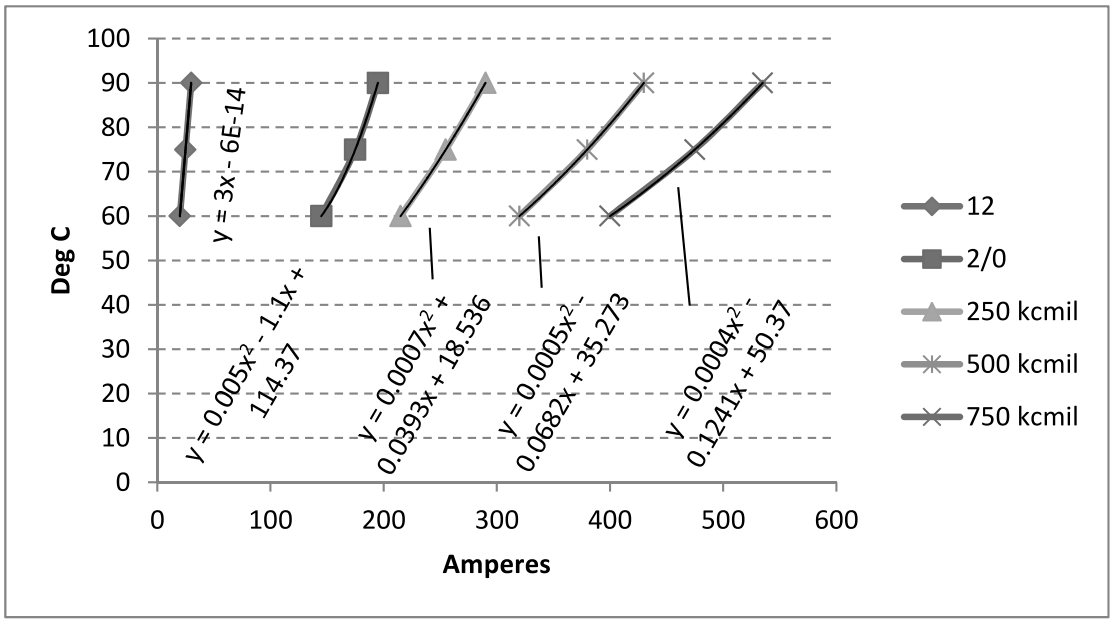

Figure 37: Predicted conductor temperature based on current flow at a 30^{O}C ambient.using equations derived from data found in NEC (NFPA 70) Table 310.15(B)(16)

Table 4: Cable Temperature Prediction (Derived from NFPA 70 Table 310.15(B)(16))

AWG	mm^2	2nd Order Least Squares Curve Fit
12	3.31	$T = 3I$
2/0	67.4	$T = 0.005I^2 - 1.1I + 114.37$
250 kcmil	126.8	$T = 0.0007I^2 + 0.0393I + 18.536$
500 kcmil	253.4	$T = 0.0005I^2 - 0.0682I + 35.273$
750 kcmil	380	$T = 0.0004I^2 - 0.1241I + 50.37$

sistance of the wire with changes in conductor temperature. The changes are large enough, such that with sufficient line length, the change in resistance of the wire will be greater than any change in resistance for a degrading connection. If all that was required was to determine the conductor temperature and factor out the change in resistance, the problem would be solved.

However, the conductor temperature is not known (or if it were known would require additional costly instrumentation that violates the design goal of using only data provided by legacy metering equipment). Therefore, without any normalization of this conductor resistance, even normal load changes may produce a change in conductor resistance similar to that seen at a degrading connection. For this sensitive resistance detection method to be useful in detecting degrading junctions, the conductor resistance due to either changes in ambient or changes in current magnitude must be factored out.

As was evident from figures 36 and 37, as temperatures increase, the derivative of the temperature versus current increases (second derivative is positive). The underlying physical property that is causing this is the increase in conductor resistance causing the recursive temperature increase. While this is useful to understand, exact data is needed. What is needed is an equation that normalizes the conductor resistance based on temperature, which may as a secondary factor, be based on current.

$$\alpha(T,I) = f(T,I) \tag{4.7}$$

It has been known [23] that copper's PTC is linear over a temperature range commonly present on electrical wiring. Since, at constant current, the power dissipated in that wire is proportional to the resistance $\left(P = I^2R\right)$, then any increase in resistance increases losses, dissipation and so works to raise conductor temperature (which as mentioned earlier, recursively increases resistance again, further increasing the temperature[2]).

As mentioned in (2.24), the cooling increases due to the higher temperature gradient between the warmer conductor and the cooler ambient resulting in a non-linear relationship between dissipated power and temperature. So while the temperature does increase, it does not increase linearly proportional to the PTC of copper. Therefore the problem is more complicated than just applying

[2]Constant power loads such as switched mode power supplies and inverters, increase current flow with decreased voltage making this problem even worse.

the α compensation factor to the resistance, although doing so is the first part of the solution. The temperature coefficient of copper and aluminum are described by the Greek letter α and defined in equations (4.8) and (4.9) ([23]).

$$R(T) = R(T_0)(1 + \alpha T) \tag{4.8}$$

$$\alpha = \frac{R(T) - R(T_0)}{T(R(T_0))} \tag{4.9}$$

It is known that the value of α for copper is approximately 0.039 [56], meaning the resistivity of copper changes by 0.39% for each degree Celsius or Kelvin. To see how this affects the previous calculation of resistance change due to failing termination, focus is returned to the diagram shown in figure 35. The equations (4.2) through (4.5) are rewritten, except now operating at a conductor temperature 20 deg C warmer (designated as $R_{cable50}$, since 30 + 20 = 50 deg).

$$\text{Original cable resistance at } 30^{\text{O}}\text{C} \quad R_{cable30} = 0.01035\Omega \tag{4.10}$$

$$R_{cable50} = 0.01035(1 + 0.00386(20)) = 0.01043\Omega \tag{4.11}$$

$$R_{good30} = R_{lug1(good)} + R_{cable30} + R_{lug2(good)} = 2 * 0.00001\Omega + 0.01035\Omega = 0.01037\Omega \tag{4.12}$$

$$R_{good50} = R_{lug1(good)} + R_{cable50} + R_{lug2(good)} = 2 * 0.00001\Omega + 0.01043\Omega = 0.01045\Omega \tag{4.13}$$

Equations (4.12) and (4.13) describe a system where the two lugs remain tight and only the overall cable resistance changes due to the increase cable temperature. From these equations the percent difference can be calculated:

$$\%\ \text{diff} = \frac{R_{good50} - R_{good30}}{R_{good30}} = \frac{0.01045 - 0.01035}{0.01035} = 0.97\% \tag{4.14}$$

Contrast this with the previously calculated equation (4.5 and repeated here as 4.15)

$$\% \text{ diff} = \frac{R_{bad} - R_{good}}{R_{good}} = \frac{0.01034 - 0.01032}{0.01032} = 0.19\% \tag{4.15}$$

A change in conductor temperature created a change in resistance over this distance that was 5 times greater than the change in resistance due to the failing lug connection, effectively and completely masking any termination degradation. This is a serious problem, but fortunately one that can be easily resolved by applying the temperature correction factors to the PTC factor shown in table 4. As the polynomial coefficients change with conductor cross section, the equations can be expanded to create a three dimensional model (in the form of $T \propto f(I,A)$, where A is cross-sectional area of the conductor. The average conductor resistivity can be solved with equation :

$$\rho = R\frac{A}{l} \tag{4.16}$$

$$A = \frac{\rho l}{R} \tag{4.17}$$

Where:

ρ	Electrical resistivity
R	Electrical resistance
A	Cross-sectional area of conductor
l	Length of material

Equation 4.17 solves for the equivalent average cross sectional area, knowing (after measuring) the resistance R with known resistivity ρ (which is a function of the conductor used). As an example, assuming the equation 4.17 resolves to a cross sectional area of 67mm^2, then the temperature compensation equation chosen from table 4 would be $T = 0.005I^2 - 1.1I + 114.37$. Plugging this factor into equation 4.8:

$$R(T) = R(T_0)\left(1 + \alpha\left(0.005I^2 - 1.1I + 114.37\right)\right) \tag{4.18}$$

This equation now solves for the new resistance based on the ambient temperature raised to a new temperature T caused by a current flow of magnitude I. This process would be repeated for

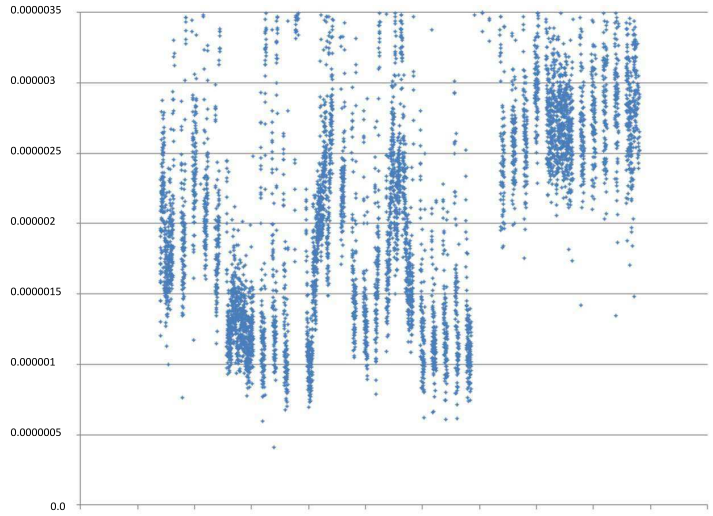

Figure 38: Impedance measurement close to noise floor of instrumentation

other feeder circuits and the corresponding equation of $T = f(I)$ from table 4 for different sized conductors (either know, or solved using equation 4.17). It is restated again, that for purposes of detecting a degrading connection, it is less important to know the actual temperature. Instead this equation will be used to predict the *relative* temperature shift caused by changes in current.

4.1.5 Oversampling

For a signal that can be considered stationary (does not change rapidly, such as lug contact resistance), reading and re-reading a signal multiple times over a time window effectively measures the same signal with differing amounts of random, zero mean noise [71].

When attempting to measure signals below the single bit resolution of the A/D, measured noise can be of a greater magnitude than the signal of interest. However, since this noise can be described statistically, and since impedance is measured as the difference of two signals, the same noise signal measured by the two nodes will subtract and externally induced (source or load) noise can be factored out, leaving largely, instrumentation noise. In this impedance measuring problem, precise measurement of a voltage drop due to a change in conductor impedance requires measurements of a sufficient precision of both magnitude and phase/timing, although as was outlined in section 3.1.

To understand the amount of precision required, consider a dc voltage input with an LSB resolution of ± 1.2 mV and a current sensor with a resolution of ± 120 mA. Pick a nominal voltage of 1001 counts (1.2012 V) and a current of 1 count (0.12 A) and calculate the equivalent impedance of such a circuit (equation 4.19).

$$Z_0 = \frac{V_0}{I_0} = \frac{1.2012}{0.12} = 10.01\Omega \tag{4.19}$$

Using equation 4.19, if the voltage changed by one count (1001 to 1002), what is the minimum change in impedance that could be measured? To calculate, repeat the calculation of equation 4.19with the voltage signal increased by one count (1.2 mV) and current signals remaining constant.

$$Z_{V+} = \frac{V_+}{I_0} = \frac{1.2012 + 0.0012}{0.12} = \frac{1.2014}{0.12} = 10.02\Omega \tag{4.20}$$

$$\% \text{ error} = \frac{Z_{V+} - Z_0}{Z_0} = \frac{10.02 - 10.01}{10.01} = 0.1\% \tag{4.21}$$

As a check point, equations 4.22 through 4.24 show that the percentage error remains the same regardless of the magnitude of the current. Raising the current to 1000 counts (120 A) and repeating the calculations:

$$Z_0 = \frac{V_0}{I_0} = \frac{1.2012}{120} = 0.01001\Omega \tag{4.22}$$

$$Z_{V+} = \frac{V_+}{I_0} = \frac{1.2014}{0.12} = 0.01002\Omega \tag{4.23}$$

$$\% \text{ error} = \frac{Z_{V+} - Z_0}{Z_0} = \frac{0.01002 - 0.01001}{0.01001} = 0.1\% \tag{4.24}$$

Changing the current magnitude (as long as it remained constant between the two readings with the changed voltage) did not affect the resolution since percent change calculation simply measures the percent change between readings and this was only affected by the (intentional) change of the voltage input.

4.1.5.1 Full Scale versus Measurement Resolution

Also, while an error of 0.1% may seem accurate enough, recall at the beginning of this section (page 63) that impedance measurements of ± a few tens of micro-ohms may be required. Further recall that in section 38 an example was given of a legacy meter that measured over a full-scale span of 14 000 V. A 12-bit A/D would divide that into 3.516 V per bit, would be a signal level nearly 3000 times the value shown in this example. So clearly additional bits of resolution (either via hardware or derived through digital signal processing) would be required. However a discussion of bits of resolution alone is misleading.

Returning to the example listed in equations 76 through 76, consider that a voltage of 1.2012 V represents just over 1000 bit counts (actually 1001) up from zero on an A/D with a LSB resolution of 1.2 mV/bit. Would the results vary if the nominal signal level were only 1/10 that value (100 bit counts, 0.1212 V)? Repeating equations 76 through 76 except substituting the lower values of V produces results shown in equations 77 through 77.

$$Z_{0b} = \frac{V_{0b}}{I_{0b}} = \frac{0.1212}{0.12} = 1.01\Omega \tag{4.25}$$

What is the minimum change in impedance that could be measured? To calculate, increase the voltage by 1-bit (1.2 mV) while keeping current constant.

$$Z_{V+b} = \frac{V_{+b}}{I_{0b}} = \frac{0.1224}{0.12} = 1.02\Omega \tag{4.26}$$

$$\%\ \text{error} = \frac{Z_{V+b} - Z_{0b}}{Z_{0b}} = 0.99\% \tag{4.27}$$

Dropping the signal level by a factor of ten, raised the error by a nearly the same factor. It is important, then, to realize that not only are a certain number of bits of resolution required over the span, but also the single bit (LSB) resolution over the span of interest within the full-scale range. Plotting the error as a percentage of the signal change relative to the single bit (LSB) resolution, the error ranges from 50%, to 0.002% for signals ranging as small as where a single bit causes a 50% error (normal value is at 1 bit, so adding one bit doubles the signal where 50% of the signal is now error) to less than 0.002% with 50000 nominal counts and error was 1 bit. 1/50000 = 0.02%. The results are shown in figure 39

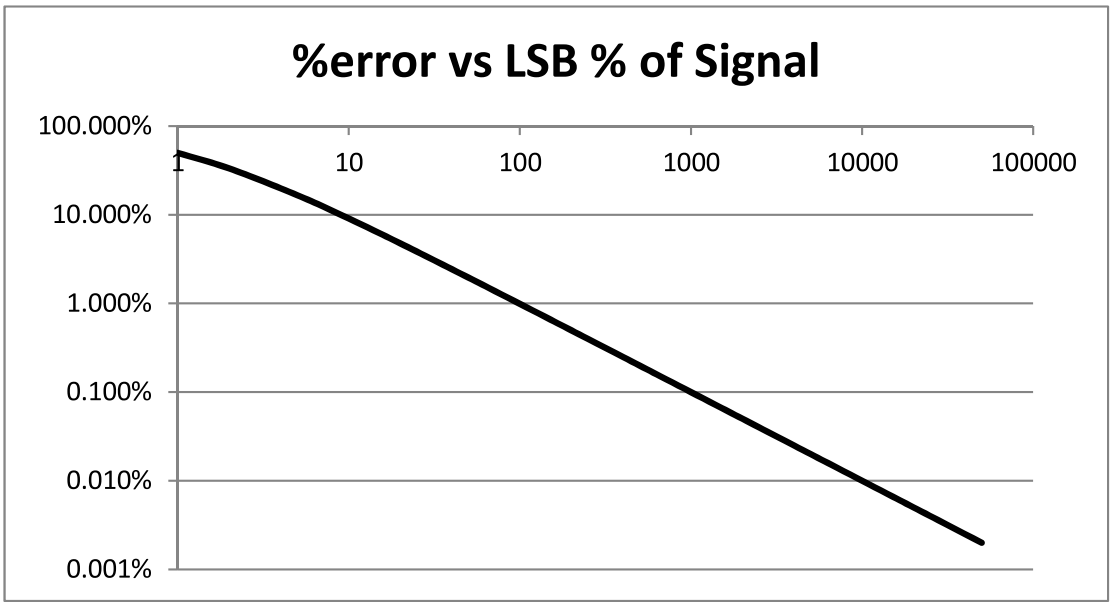

Figure 39: Chart of percent error vs ratio of full-scale span divided by single bit resolution

While it is important to note that a signal such as calculated impedance (figure 38) may be well below the instrumentation noise floor (i.e. the signal to noise ratio, SNR [15] can be negative, or the magnitude of the noise greater than that of the signal), because of the ability to factor out non-linear switching events up and downstream, the remaining detection problem is reduced to a parametric problem (known physics) with known (or assumed) noise characterization. For reference, the metric SNR used to define the ratio of signal and noise is defined as being proportional the logarithm of the ratio of signal variance (power) to noise variance.

$$SNR = 10 \cdot \log_{10}\left(\frac{\sigma_x^2}{\sigma_e^2}\right) \tag{4.28}$$

For example, plotting the magnitude of a calculated impedance signal over time (figure 38) creates a scatter plot with samples that, even with thousands of samples, show no clear tendency to cluster to a central values. As discussed earlier, the central value theorem [41]predicts that as the number of samples increases, the mean value of the noise signal will approach zero. The fact

that this is not happening in figure 38 would indicate that insufficient samples have been collected,, the underlying physical properties of the system (resistance and/or reactance) are changing, or the noise source was correlated (not i.i.d).

In one respect, that last factor can be considered true. Consider that due to circumstances mentioned in section 4.2 prior to subtracting / canceling, the noise sources common in power systems may not all be uncorrelated from one another. Likewise, the second possibility (changing physical conditions) could be occurring since, as was discussed earlier (4.1.4.1), changes in conductor temperature due to changing current flows will cause a change in measured resistance. As this data was collected over nearly 9 days, the magnitude of the current (and therefore the conductor temperature) varied. Consider that figures 16 and 17 show ranges of power flows in that same facility ranging 10:1.

Finally, even the first possibility (insufficient samples) is a very real possibility depending on the SNR. The lower (or more negative) the SNR, the more oversampling and noise shaping is required. Evidence of this is shown by the scaling of the y-axis. The nominal values appears to be in micro-ohms, but before too much faith is placed in the absolute value, consider that some calculated resistance values could be negative. This occurs due to inaccurate calibration where the downstream meter reports a higher voltage than the upstream, creating an apparent negative resistance. Methods of working around this issue were introduced in 2.3.4 and will be shown experimentally section 4.3 on page 104, but a quick discussion of quantization errors and oversampling will now be presented to provide justification for the steps taken below.

Returning to figure 38 on page 75, this data capture represents approximately 12 000 rms voltage and 12 000 rms current values time-aligned with each other, then ratioed (see equation 4.29) to calculate impedance $Z(t)$ over time for a single phase of a 3000 ampere, 480V circuit breaker. Each tick mark on the x-axis is one full day.

$$V_{rms}(k)/I_{rms}(k) = Z(k) \tag{4.29}$$

Y-axis units are in Ohms. Since the actual underlying impedance is known to not be changing over this range, a filter is applied to remove the noise and extract the actual signal.

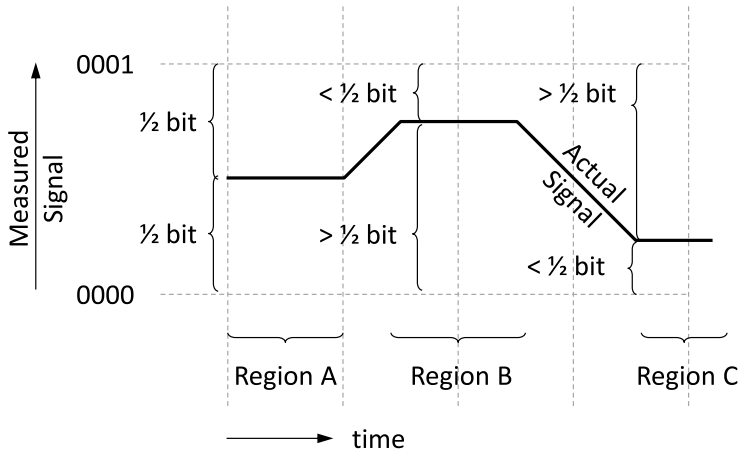

Figure 40: Sub-bit variations in signal level resolved statistically

4.1.5.2 Injected Noise Effects A physical property (like impedance) that changes below the single-bit resolution of the metering equipment, nevertheless can cross those bit boundaries when external noise is applied to the signal. As shown in 40 even changes in signals below the single bit resolution of the equipment can be detected, if the assumption is made that the external noise source is zero mean.

While a signal that deviates less than the equivalent of 1-bit in magnitude in a noiseless environment never crosses the threshold of an A/D level, when noise is added, the signal *can* cross those barriers. Moreover, since the central value theorem predicts that with a normal distribution of noise (equally likely both directions and magnitudes), the likelihood of crossing a particular barrier is related to how "close" the underlying signal is to those barriers. This is a key finding since it implies (and is proven experimentally [59]), that when a signal changes with a magnitude of less than one bit, it can nonetheless be detected by the (low resolution) metering devices, if a noise signal of sufficient magnitude, and of particular character (zero mean, limited variance) is superimposed on the underlying signal (in this case impedance). Through oversampling, the noise can be filtered and an underlying reading (of higher resolution than when measured in a noiseless environment) results. In the simplest case of direct quantization without any advanced noise shap-

ing ([71, pp. 201-213]), a value can be calculated that predicts the number of oversampling events that must occur to extract the equivalent higher resolution.

$$Multiple_{req} = 2^{(bits_{req} - bits_{avail})} \tag{4.30}$$

Using the example from Equation (4.30), the multiple of the number of samples required is calculated. In the experiment discussed above, the existing metering includes 12-bit resolution on both voltage and current sensing. In order to obtain the equivalent of 20-bit resolution, Equation (4.31) is solved.

$$Multiple_{req} = 2^{(20-12)} = 2^8 = 256 \tag{4.31}$$

The solution of this equation implies that by oversampling each value 256 times, our experimental system achieve the equivalent resolution of a 20-bit system. This, in fact, was demonstrated and documented in [59].

Figure 41 shows the same data as shown in figure 38, but with a 200-point rolling average superimposed. Evidence of aliasing and beat frequencies are evident and show that oversampling alone does not provide an accurate, or high enough resolution, model of the underlying impedance.

4.1.5.3 Experimental Results To validate the magnitude of the resolution enhancement, the schematic as shown in figure 42 was built and used as the test platform.

$$I = \frac{V_{in}}{(10.2 + 100 + Z_u)} = \frac{2.5\text{ V}}{(10.2 + 100 + Z_u)} \tag{4.32}$$

An 8-channel USB analog input module ($\pm$10Vdc span, 14-bit resolution, 1.2 mV/bit) captured V_{in}, V_{out}, and the derived $I \approx \frac{V_{in} - V_{out}}{10.2}$ (current measured using the 10.2 Ω resistor acting as a shunt over which the voltage drop was measured) were plotted at a sample rate of 240 samples/sec. As discussed in section , the timing accuracy of this device channel-to-channel is not affected by variable (non-deterministic) delays. Also, since these initial tests were performed with direct current, phase angle measurements do not apply. Later tests will use alternating current, and here timing jitter will become a factor. Figure 43 shows the distinct quantization levels for the calculated value of $V_{in} - V_{out}$, with each step represented 1.2 mV greater or less than the previous.

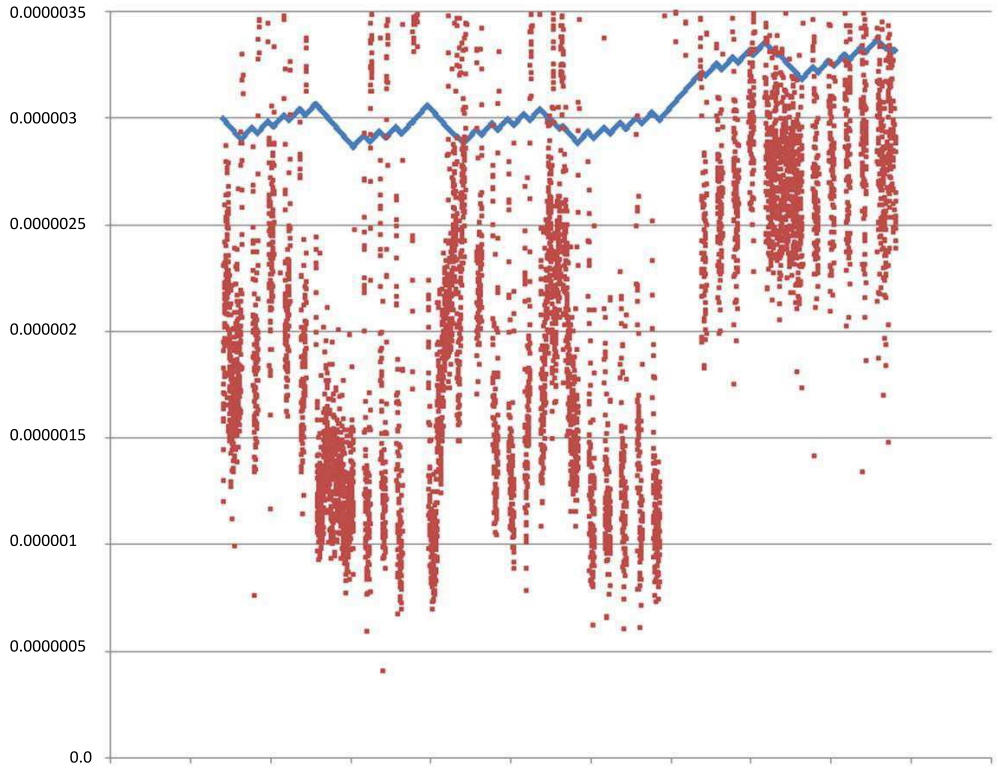

Figure 41: Signals resolved at or below noise floor

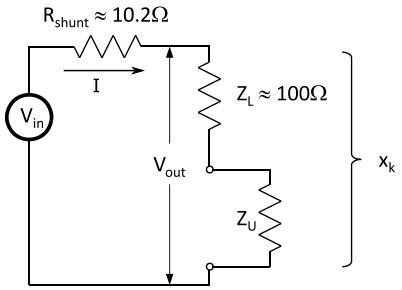

Figure 42: DC Test circuit for filter experiments with $V_{in} \approx 2.5$ V

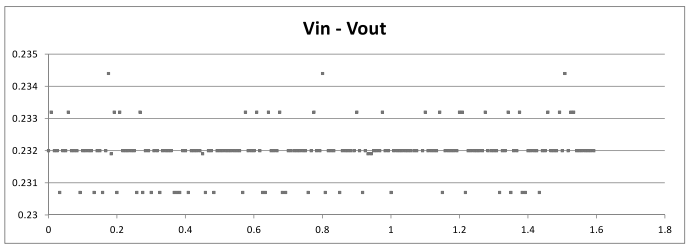

Figure 43: Plot showing the quantization limits of resolution for voltage measurements

Solving 4.32 for Z_u:

$$Z_u = \frac{2.5}{I} - 110.2 \tag{4.33}$$

$$Z_u = \frac{2.5}{\frac{V_{in}-V_{out}}{10.2}} - 110.2 = \frac{25.5}{V_{in}-V_{out}} - 110.2 \tag{4.34}$$

To calibrate the system, the equations are solved with $Z_u = 0$. In that situation, x_k can be solved as:

$$x_k = \frac{V_{out}}{I} \tag{4.35}$$

Equation 4.35 is plotted in the graph in figure 44.

Subject to the published tolerances on the resistor Z_L, the calibration of the shunt resistor R_{shunt} and the accuracy of the A/D input module, the expected value of $x_k$would be ~100Ω. Due to the

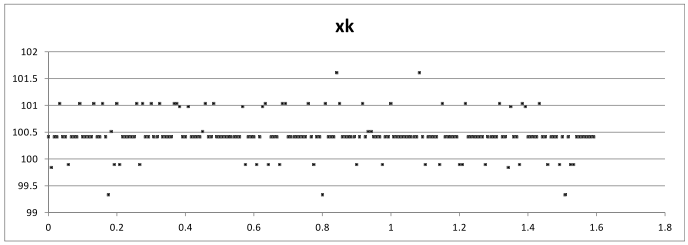

Figure 44: $x_k(Z_L)$ with $Z_u = 0$

quantization levels not including enough bits to resolve 100Ω precisely, plus the the reality of noise in the measurement system, figure 44 shows a scatter plot of calculated resistances ranging from 99.33Ω up to 101.61Ω. Over the range of these 192 data points the average x_k was, in fact 100.45Ω, very close to our estimate and certainly within tolerance of these components.

For the next part of the experiment, Z_U was increased by resistance of a 45.7 cm, 24 AWG copper wire (resistivity ρ = 1.724e-8 ohms/m). At 84.2 ohms/1000 m, the resistance is calculated as:

$$R = \frac{\rho L}{A} = \frac{1.724 \cdot 10^{-8} \frac{\Omega}{m} \cdot 0.457 \text{ m}}{\pi \cdot (0.000511/2)^2} = 0.0384\Omega \tag{4.36}$$

What immediately stands out is that the actual resistance measured by the experiments exceeds 150 mΩ, not the predicted 38 mΩ. As this wire was plugged into a breadboard, the total resistance included not only the resistance of the wire, but also of the breadboard spring clips and the underlying interconnects within the breadboard. This type of sensing is exactly the purpose of this low resistance measurement. Consider that in distribution equipment the resistance contained within a circuit breaker is only part of the circuit. The stabs on the breaker, any wires clamped to terminals, shipping splits in equipment or any other non-welded junction has the potential for degradation.

However, to detect failing junctions, the primary need is not to be able to detect absolute impedance or resistance values. Rather the assumption will be made that after installation, sufficient tests were performed to validate the installation and to have declared that whatever value of impedance or resistance is present is considered normal. At this point the impedance/resistance monitoring system begins trending, only looking for deviations from this previously declared "normal" value. Since the physical properties of this 45.7 cm wire have not changed, a warning sign would be any *unexplained* increase in resistance.

As was discussed above, the average value of the 192 data points provided an estimate of the impedance (resistance) value with a finer resolution than was possible with a single reading. In other words, oversampling allows for intra-bit values to be possible, so the next step was to compute a rolling average of the signal. A 200-point moving average signal was calculated and plotted with the raw $x_k$calculation and shown in figure 45.

Due to the quantization error, the majority of the calculated values remain within the 101.5 to 100 ohm band. However, it is clear from looking at the plot, that following the point where the

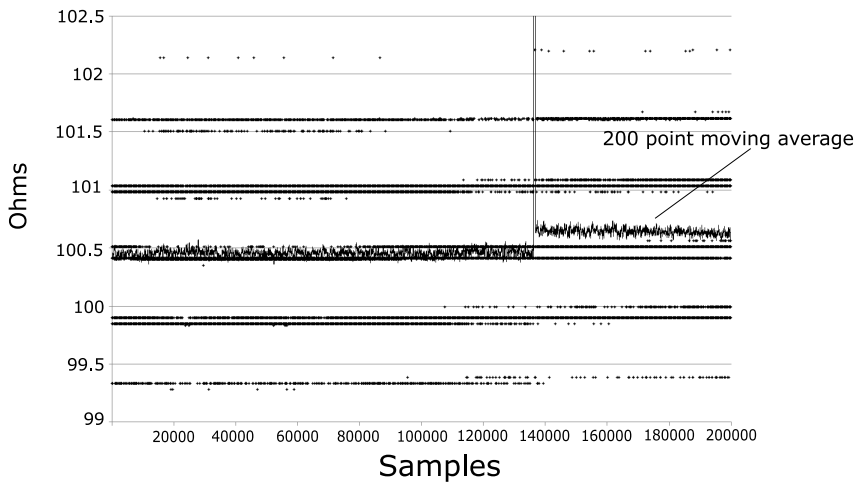

Figure 45: 200 point moving average superimposed over raw Z calculation showing a clearly detectable change after the switching operation.

extra resistance was added, the likelihood of occasional values greater than 101.5 increased, while the likelihood of values less than 100 ohms decreased. If the need was to determine if something greater than 0.1Ω (100 mΩ) were added, clearly this system provides sufficient resolution. But recall, that the input voltage was only 2.5 V. Full scale on this 14-bit A/D was 10 V, meaning that the 2.5 V represented 25 percent of full scale, a substantial portion.

If, on the other hand, the 14-bits were divided across 600 V or 14 400 V, far fewer bits would be available and as shown in figure 39, the error increases dramatically as the signal level diminishes. And consider that even with the 25% span being used, the noise band appears to display 0.05 - 0.1 Ω of uncertainty. This would be insufficient to detect the 20-30 $\mu\Omega$ changes that might be expected in a typical junction.

Oversampling, on its own appears to not provide sufficient resolution enhancement. It is apparent that other methods of noise filtering are required beyond calculating averages of signals. Other methods such as first and higher order noise shaping ([71, pg 209]) provide additional noise reduction for less oversampling, but what will be shown in the paper is a method that provides even better performance than oversampling, even when noise shaping. The improvement in resolution was surprising.

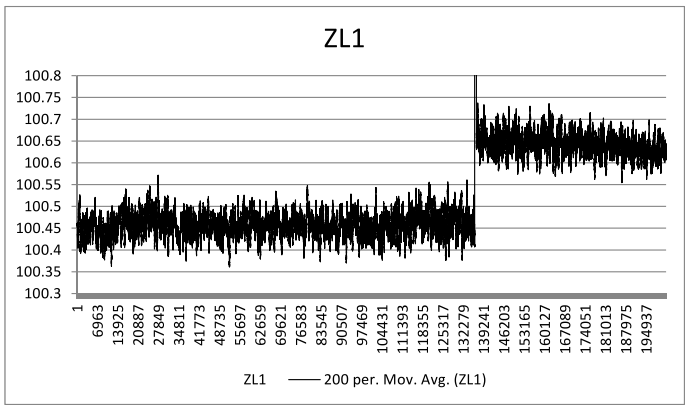

Figure 46: With 14-bit A/D resolution Approximately 0.18 to 0.20 Ω increase in resistance visible after 45 cm, 24 AWG wire added to circuit

4.2 FILTER DESIGN

Filter design is a well researched area of study [91, 10, 43, 52, 71, 88, 15]. While the purpose of this chapter will be to explain why certain filters work best for this impedance measuring problem, the reader is directed to external resources for in depth analysis regarding filter design. This document will, instead, explain why a particular filter was chosen. To begin this process, a quick overview of filter theory is presented to acquaint all readers with the necessary background to appreciate the reason behind that particular selection.

From a signal-processing point of view, the problem was particularly interesting. On the one hand, a large portion of the detection effort on this project was able to use parametric methods because the underlying physics of the electrical power system are understood. However, due to stochastic switching (both sources and loads), those physical properties change at unpredictable times. What was confirmed was that measurements made at a sufficiently high sample rate (over a sufficiently narrow time window) can be modeled as linear and time-invariant unless a switching event occurs during that window. Using the normalization process of measuring both the up and downstream Z and calculating the difference in those values also removed external signals. Finally as with other stochastic processes, these randomly occurring events can be analyzed statistically.

Next, in addition to statistical processing and other known techniques to linearize non-linear processes (Jacobian, smaller window, faster sample rate, etc.), a pre-processing "triage" step was defined during which data containing transients (specified defined as where dV/dt or dI/dt deviated out side "sine tracking[3]" limits) were processed using a separate set of algorithms. When the output of this triage step showed a signal deviated from a stationary process, a separate analysis was used. These changed the analysis of the system away from using the more typical Bayesian / Markov[4] techniques to a set of custom technique that switched algorithms depending on the state of the process. All measurements include errors due to noise. In particular, careful attention is paid to the separate characterization of systemic (epistemic) and statistical (aleatonic) noise (uncertainty). Epistemic uncertainty deals with the problem of insufficient resolution with the data collected by the legacy metering and protective devices. Aleatonic uncertainty compensation works on the problem of how non-linearity (and its unpredictable noise) can be modeled, and therefore, removed. A major discovery of this research was to create a method that improves both types of uncertainties.

As can be inferred from statements made earlier, all the filter designs presented below will be presented from the point of view that assumes commonly installed metering and protective devices were used to collect voltage, current and phase angle data. The work effort is to post process that data, in whatever form it exists, with the goal of obtaining sufficient resolution to detect important precursors of equipment failure. Since the typical legacy metering devices are designed to measure large ranges (even worse, protective devices might need to measure 8x or greater multiples of full-load current), the available bits are stretched across a potentially wide range, reducing the precision per bit. With signal resolution at perhaps a one part in 4096 (12-bit) resolution, the available span per bit will be quite large in legacy metering.

As discussed earlier and shown below in more detail, these legacy metering devices do not, naively, offer sufficient resolution to measure the micro-volt, or even milli-volts changes in voltage drop to detect a change in a conductor's impedance indicating a failing junction. Obtaining such

[3]Sine tracking implies that the underlying fundamental frequency of the signal is tracked and the next sample is "predicted" based on knowledge of the previous signals (states). A deviation outside a selected dead band around that estimated signal (e.g. $\pm 10\%$ of the next predicted value) causes a derivative (dV/dt or dI/dt) trigger that initiates this triage processing.

[4]Bayes Rule states that prediction of a future state can be based on knowledge of previous states. This will be discussed later and shown in equation 92

resolution from the rather poor data source raises the level of importance in this task of filter selection.

For all the systems modeled, over the "linear" period of data collection, the noise source will be assumed to be i.i.d. (independent, identically distributed) with zero mean and with finite energy (and therefore a non-infinite variance). As will be explained below, both assumptions are valid for these power systems.

To provide a basis for the discussion that follows, the standard definitions common with stochastic processes will be reviewed to show how they are applicable to the filter selection decisions made. The reader familiar with random variables and calculating probability within random processes may skip to section 4.2.1, but since this research cross-cuts multiple domains within electrical engineering, this material is included to insure a firm understanding of the relevant principals discussed later.

The first concept is the to explain is the reason for assuming that noise will be i.i.d with zero mean. The mean, or expected value of the random noise is defined as in equation (4.37):

$$\mu_x = \bar{x}_k = E(x) = \sum_k x_k p_x(x_k) = 0 \tag{4.37}$$

$$p_x = P(X = x) \tag{4.38}$$

Equation (4.38) defines a probability mass function, p_x, that characterizes the likelihood, or weighting, of a particular random variable X of having a particular value when measured. To further characterize these random variables, the methods outlined here will rely on the central limit theorem [41] which predicts that these random signals, as being created from the sum of a large number of independent random variables, will approach the standard normal (Gaussian) random variable with mean = 0 and variance = 1. While the filter chosen doesn't strictly require standard normal random noise variables, the central limit theorem predicts that this will be the type of signal measured. The shorthand notion used when describing the standard normal Gaussian r.v. is written as $\mathcal{N}(0,1)$. While some noise generated in the power system is *not* random (e.g. higher probability of arcing the closer to reaching a sinusoidal voltage peak, predictable transients due to air or vacuum interrupter current chop or SCR switching near current zeros, semiconductor commutation

near multiples of 15, 30 or 60 degrees in multi-phase converters / rectifiers, etc.), a premise of the central limit theorem is that the larger the combination of these type of random variable, the more they look Gaussian with mean zero. Power systems have *many* different loads operating independently, each generating some percentage of correlated and uncorrelated noise. In summary, while the filter method described below does not require standard normal noise distribution, the theory predicts that this is the type of signal that will be measured.

Another assumption made from the central limit theorem is that the random variables will be characterized with unit variance. The reader recalls that variance is a measurement related to the distance between each sampled value and the overall sample space mean, or specifically:

$$\sigma_x^2 = \mathrm{Var}(X) = E\left\{[X - E(X)]^2\right\} = \sum_k (x_k - \mu_x)^2 p_x(x_k) < \infty \tag{4.39}$$

Or alternatively written as:

$$\sigma_x^2 = \mathrm{Var}(X) = E\left[X^2\right] - E^2[X] \tag{4.40}$$

When dealing with two random variables, the reader also recalls the additional element defined as covariance, and written as $\sigma_{x_1x_2}^2$, is used:

$$\sigma_{x_1x_2}^2 = cov(x_1x_2) = E[(x_1 - \bar{x}_1)(x_2 - \bar{x}_2)] \tag{4.41}$$

Dividing the covariance by the product of the individual variances produces the normalized measure of correlation between the two random variables and is defined as the correlation coefficient ρ_{12}:

$$\rho_{12} \equiv \frac{\sigma_{z_1x_2}^2}{\sigma_{x_1}\sigma_{x_2}}. -1 \leq \rho_{12} \leq 1 \tag{4.42}$$

For i.i.d. variables, which for the periods over which the signal is considered "linear", the correlation coefficient for the measured noise $\rho_{12} = 0$.While all the preceding equations have been scalar, in typical power systems, the measure of variance between elements of the admittance matrix (3.14) (3.15) will be accomplished by grouping multiple covariances between random variables into a covariance matrix. In particular the discussion of the Kalman filter will explain how the covariances are of central importance in calculating the internal states of the Kalman filter.

Once in matrix form, linear algebra principals can be used to interpret the results in newer, more meaningful ways. In particular, converting equation (4.39) to a matrix form (as a column vector $x = [x_1, x_{2,} \ldots x_n]^T$) can be defined as [44] :

$$\begin{aligned} cov(\mathbf{x}) &\equiv E\left[(\mathbf{x}-\bar{\mathbf{x}})(\mathbf{x}-\bar{\mathbf{x}})^T\right] \\ &= \int_{-\infty}^{\infty}\ldots\int_{-\infty}^{\infty}(\mathbf{x}-\bar{\mathbf{x}})(\mathbf{x}-\bar{\mathbf{x}})^T \rho(\mathbf{x})\, dx_1 \ldots dx_n \\ &\equiv \mathbf{P}_{xx} \end{aligned} \tag{4.43}$$

This covariance matrix will be a symmetric n by n matrix and will be positive definite with order n (unless there is a linear dependence between components). The relationship between (4.41) and (4.43) is that the $(i,j)^{th}$ element of the covariance matrix $\mathbf{P}_{xx}$ is $\sigma^2_{x_1x_2}$. Diagonal values within $\mathbf{P}_{xx}$ are variances (e.g. the scalar value for that particular sample as defined in (4.39)).

While knowing that a zero mean implies that the noise will cancel over a time average, for practical purposes the averaging period required to sample can be too long to be practical[5]. One method of linearizing around a sampled value is to increase the sampling rate to obtain more points nearby. The expectation is that during that time window the process can be modeled as being linear. Unfortunately, that method is not available for owners of legacy metering equipment. Certainly if metering equipment could be chosen to reduce the sampling interval (and so provide more samples per window), this problem would could be mediated. Because the goal of this design is to develop a solution that can operate with legacy equipment, the sample rate may not be fast enough to create a narrow enough sample window to create a time-invariant window within the time varying process. In other words:

$$y(t) = f(x(t)) \neq f(x(t+\delta)) \tag{4.44}$$

Since a time-invariant process cannot be assumed, other methods of canceling the noise are required.

[5] As shown in figure 75, the underlying process was not time-invariant over the window where these values were sampled.

4.2.1 State Estimation of Process

The output of the filter is an estimation of the actual state of the system or the measurement of a sensor. For causal systems (i.e. systems that only rely in historical data), this implies that past data can predict a future state. Using the equations listed in the previous section, this assumes the system is linear and time invariant (LTI), both conditions that we know (or will be proven) that this system is not. However, by careful selection of data, portions can be modeled as LTI and can be processed with those equations.

Those portions of the data modeled as LTI will be described here but can be defined by the relationship between the current state $\mathbf{x}(t_0)$, the current input $u(t)$ and that next state (output) $y(t)$.

$$\left.\begin{array}{c}\mathbf{x}(t_0)\\ \mathbf{u}(t), t \geq t_0\end{array}\right\} \mathbf{y}(t), t \geq t_0 \tag{4.45}$$

With this background we define the state sequence conventionally.

$$\mathbf{x}_k = \mathbf{f}_k\left(\mathbf{x}_{k-1}, \mathbf{v}_{k-1}\right) \tag{4.46}$$

Where $\mathbf{f}_k$ is a (potentially) non-linear function of the state $\mathbf{x}_k$ with an i.i.d process noise sequence defined as $\mathbf{v}_k$.

Likewise, our input signal vector $\mathbf{z}_k$ is assumed to be similarly corrupted with measurement noise, $\mathbf{n}_k$, which masks the true state $\mathbf{x}_k$ that the filter is attempting to measure.

$$\mathbf{z}_k = \mathbf{h}_k\left(\mathbf{x}_k, \mathbf{n}_k\right) \tag{4.47}$$

Of course while the noise sequence is considered a random i.i.d sequence, the underlying signal is not.

As discussed (4.2), one problem is that the underlying signal cannot be measured with sufficient precision with the existing legacy equipment. However, since the system model can be constructed from physical properties (energy storage, losses, etc.), certain predictive (Bayesian) principals can be applied since the system would be known to have a certain voltage, current, flux, speed, charge or other physical property that, while not known precisely, are known to exist. Therefore, since the next state for a parameter (e.g. V, I, speed) is expected to be related to

the previous, a recursive process of processing the previous state, any external influences, and the noise through a filter function $\mathbf{f}_k$ is done with the goal of providing some degree of certainty in the estimation of the next state. The scope of work, then, breaks down to be the determination of a particular state (impedance, phase angle, etc.) based on knowledge of measurement of the previous state and any measured external influences, with an understanding of the current state of the system. This implies that some knowledge of the state at time $k-1$ is known. Then, at its simplest level, the chosen filter performs a prediction function that uses prior state information (x_{k-1}) to infer the current state (x_{k-1}). One technique of accomplishing this is with the use of the Chapman-Kolmogorov equation [10].

$$p\left(\mathbf{x}_k \mid \mathbf{z}_{1:k-1}\right) = \int p\left(\mathbf{x}_k \mid \mathbf{x}_{k-1}\right) p\left(\mathbf{x}_{k-1} \mid \mathbf{z}_{1:k-1}\right) d\mathbf{x}_{k-1} \tag{4.48}$$

Reminding ourselves of Bayes' Rule that states that the conditional probability of event A given event B is defined as:

$$p\left(A \mid B\right) = \frac{p\left(B \mid A\right) p\left(A\right)}{p\left(B\right)} \tag{4.49}$$

And because it is recognized that any current state has been reached as a result of moving through previous states:

$$p\left(\mathbf{x}_k\right) = p\left(\mathbf{x}_k \mid \mathbf{x}_{k-1}\right) = p\left(\mathbf{x}_k \mid \mathbf{x}_{k-1}, \mathbf{z}_{1:k-1}\right) \tag{4.50}$$

Writing $p\left(\mathbf{x}_k\right)$ is just a short-hand expression for the more accurate Markov expression of $p\left(\mathbf{x}_k \mid \mathbf{x}_{k-1}\right)$. In other words, this equation uses the same notation as (4.49) with the notation $p\left(a \mid b\right)$ implying the probability of the occurrence of a condition a event occurring based the condition b has occurring is as defined in (4.50).

Likewise, the state of the measurement vector can be determined based on knowledge of previous values read:

$$p\left(z_{1:k}\right) = p\left(z_k \mid z_{1:k-1}\right) \tag{4.51}$$

Once time step k is reached, z_k data becomes available so using (4.49) the next state $p(\mathbf{x}_k)$ can be determined:

$$p(\mathbf{x}_k \mid \mathbf{z}_{1:k}) = \frac{p(\mathbf{z}_k \mid \mathbf{x}_k)\, p(\mathbf{x}_k \mid \mathbf{z}_{1:k-1})}{p(\mathbf{z}_k \mid \mathbf{z}_{1:k-1})} \tag{4.52}$$

While recursively solving (4.52) will provide the optimal solution, the solution is only available analytically for certain methods (including the standard Kalman filter used with linear data inputs). However, as will be shown, because of the system is neither linear, nor time-invariant, this equation does not provide optimal results. The intractability of the optimal solution of a non-linear power system when using the Kalman filter led the research towards other methods that were analyzed and then discarded (extended Kalman filter, approximate grid based filters and, to some extent, particle / Monte Carlo filters) [10].

4.2.2 Kalman Filter

The Kalman filter [39] operates recursively over data that includes noise and provides an optimal estimate of the underlying signal using the statistical technique of producing an estimate of the value and an estimate of the error, assuming the system is linear and the signal is corrupted by uncorrelated noise that can be modeled with a mean and covariance [40, 29]. The Kalman filter is a good beginning point for this analysis since it has been shown to provide the optimal estimation for a linear system corrupted by uncorrelated noise [61]. The steps to understand why begins by breaking this optimization calculation into two state estimation problems. The first is shown using a simplified model as shown in figure 47.

From figure 47 it is shown that the next state is estimated based on the value of the previous state summed with a ratio of sums between the measured process variable and the previous sample. The factor that is used to determine what percentage of the next state is based on the previous state or from the process variable is called the Kalman Gain. As is evident from 47 a Kalman gain of 0 results in $\hat{x}_k = \hat{x}_{k-1}$, whereas a Kalman gain of 1 is:

$$\hat{x}_k = \hat{x}_{k-1} + z_k - H\hat{x}_{k-1} \tag{4.53}$$

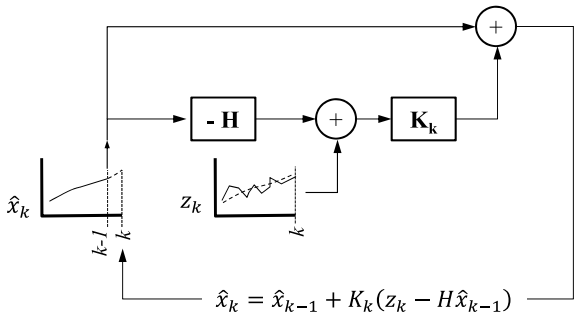

Figure 47: x_k state estimation loop of a Kalman Filter data flow diagram

If $H = 1$ then,

$$\hat{x}_k = z_k \tag{4.54}$$

The state estimation loop diagram 47, then, states that with a Kalman Gain = 1, the next state is based solely (in the case of $H = 1$) on the most recently retrieved process variable and completely discounts the previous step, while a Kalman Gain results in the process variable being completely ignored.

With such importance placed on the proper selection of the Kalman Gain, attention is next turned to the equations used to iteratively derive it. Referring to figure 48 show how the choice of K_k is calculated in a separate loop that does not consider any process variable or process state equation. Rather, as will be shown below, it is computed indirectly based on a "prediction/Covariance error($\mathbf{P}_k$) matrix" which in turn is computed from a process noise metric (covariance of the noise vector).

While the direction of the data flow arrows in figures (47) and (48) shows information flow in a particular direction, backward-time Kalman filters has been developed [34]. While this technique will not be discussed in detail, [10] describes a method where "It is possible to formulate a backward-time Kalman filter that recurses through the data sequence from the final data to the first and then combines the estimates from the forward and backward passes to obtain overall smoothed estimates." As was pointed out in the article, this technique suffers from the need to calculate the inverse of a matrix that may be non-existent (singular / diminished rank).

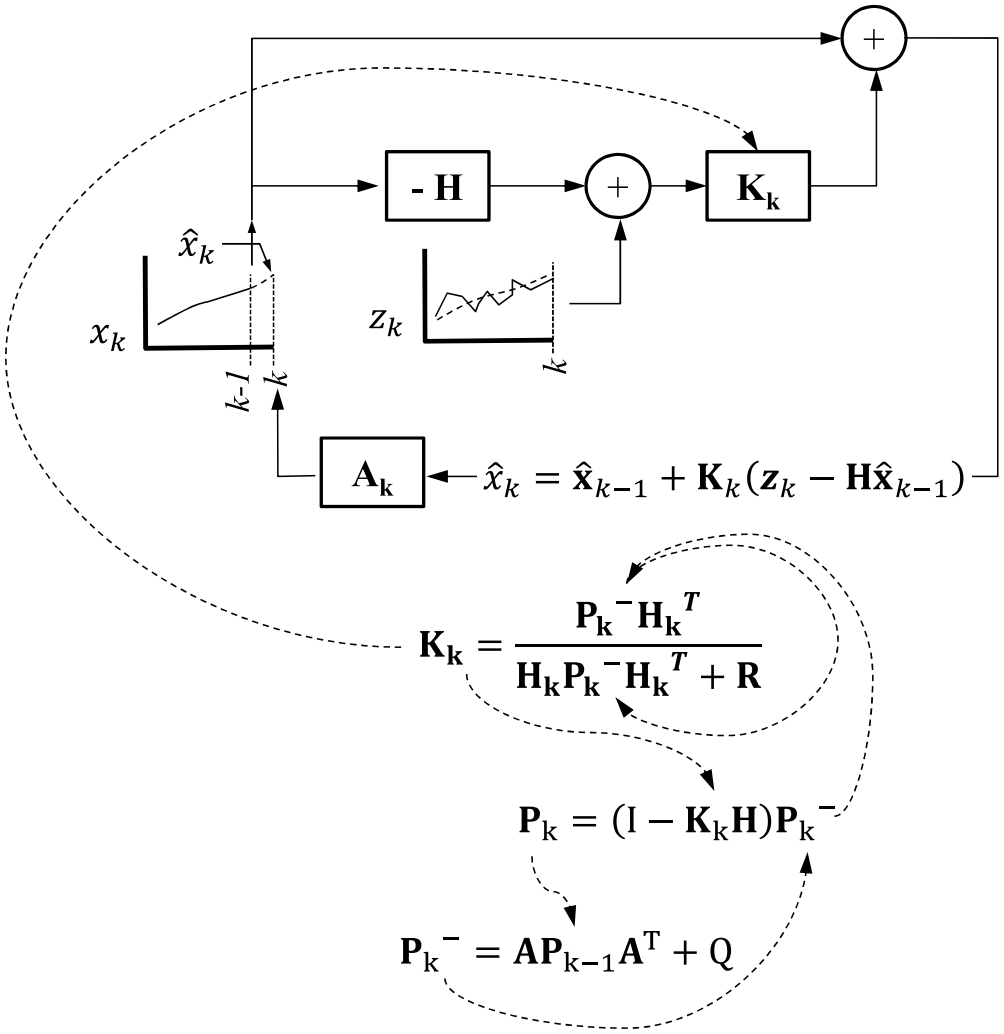

Figure 48: Measurement correction loop added to prediction loop

When examining figure 47, an intuitive understanding can be gained by assuming the H matrix to be the identity matrix. As described earlier, assume the present value of the Kalman gain $(K_k) = 0$. In that special case, the next state is set to the previous state (the input signal z_k is totally ignored). Why would this occur? This can occur when the external signal is corrupted or otherwise invalid. What can cause the opposite condition when the Kalman gain $(K_k) = 1$. In that special case, the next state ignores the previous state and all decisions on state estimation come from the input signal z_k. This extreme could occur during system start up where the previous state is found to be invalid. In practical implementations, the value of the Kalman gain will range between 0 and 1.

The process to analyze the Kalman filter further begins by writing the linear state equations:

$$\mathbf{x}_k = \mathbf{A}_k\mathbf{x}_{k-1} + \mathbf{B}_k\mathbf{u}_k + \mathbf{w}_k \tag{4.55}$$

$$\mathbf{z}_k = \mathbf{H}_k\mathbf{x}_k + \mathbf{v}_k \tag{4.56}$$

Where:

$\mathbf{A}_k$	Linear state transition model applied to the previous state $\mathbf{x}_{k-1}$
$\mathbf{B}_k$	Control input model applied to control vector $\mathbf{u_k}$
$\mathbf{u}_k$	Control signal vector
$\mathbf{w_k}$	Zero mean multivariate process noise with covariance $\mathbf{Q}_k$ $(\mathbf{w}_k \sim \mathcal{N}(0, \mathbf{Q}_k))$
$\mathbf{z}_k$	External observation of the true state $\mathbf{x}_k$
$\mathbf{H}_k$	Linear observation model mapping true state space into observed space
$\mathbf{v}_k$	Zero mean measurement noise with covariance $\mathbf{R}_k$ $(\mathbf{v}_k \sim \mathcal{N}(0, \mathbf{R}_k))$

Note:

$$E\left[\mathbf{w}_k\mathbf{w}_k^T\right] = \mathbf{Q}_k \tag{4.57}$$

$$E\left[\mathbf{v}_k\mathbf{v}_k^T\right] = \mathbf{R}_k \tag{4.58}$$

An initial insight as to the problem of using the Kalman filter in this application comes from realizing that equations (4.55) and (4.56) as well as figure 48 are written as a linear set of equations.

This is because the Kalman filter equations assume that the **A**, **B**, and **H** matrices are linear and known. However, in a power system with switches and circuit breakers, one or more of these transfer functions change during the transition. While the noise vectors are assumed to be mutually independent, during the transition the noise vectors may be correlated during this time. All of this serves to complicate the use of the Kalman filter. Solutions to this problem will be discussed later, but the next step is to compute the covariance/ error matrix. The time update prediction equations (4.59) and (4.60) rely on a computed covariance matrix $\mathbf{P}_K$.

$$\hat{\mathbf{x}}_k^- = \mathbf{A}_k\mathbf{x}_{k-1} + \mathbf{B}_k\mathbf{u}_k + \mathbf{w_k} \tag{4.59}$$

$$\mathbf{P}_k^- = \mathbf{A}_k\mathbf{P}_{k-1}\mathbf{A}_k^T + \mathbf{Q}_k \tag{4.60}$$

Where:

$\hat{\mathbf{x}}_k^-$	Estimate of the current state
$\mathbf{P}_k^-$	Prediction error
$\mathbf{Q}_k$	Covariance matrix of the process noise $\mathbf{w}_k$

Notice that the $\mathbf{A}_k\mathbf{P}_{k-1}\mathbf{A}_k^T$ portion of equation (4.60) is simply the $\mathbf{A}_k$ state transition matrix squared then "skewed" by the $\mathbf{P}_{k-1}$ covariance matrix, then summed to $\mathbf{Q}_k$.

$$\mathbf{P}_k = \begin{matrix} \sigma_{11}^2 & \sigma_{12}^2 & \cdots & \sigma_{1k}^2 \\ \sigma_{x_1x_2}^2 & \sigma_{22}^2 & \cdots & \sigma_{2k}^2 \\ \vdots & \vdots & \ddots & \vdots \\ \sigma_{k1}^2 & \sigma_{k2}^2 & \cdots & \sigma_{kk}^2 \end{matrix} \tag{4.61}$$

Where:

σ_{11}^2	corresponds to $\sigma_{x_1x_2}^2$(as described in equation 4.41)

To understand how this works, consider a system with i.i.d. standard normal Gaussian noise variance terms $\mathcal{N}(0,1)$.

With such a system, only the direct variance terms have value $\left(\sigma_{ii}^2 \text{ where } i = 1,2\ldots k\right)$ while the covariance (off diagonal) terms $\left(\sigma_{ij}^2 \text{ where } i,j = 1,2\ldots k, i \neq j\right)$ are zero (i.i.d, therefore each

subsequent reading is completely uncorrelated with any prior). As such the prediction error matrix $\mathbf{P}_k$ (equation 97) can be written as (4.62).

$$\mathbf{P}_k = \begin{matrix} 1 & 0 & \cdots & 0 \\ 0 & 1 & \cdots & 0 \\ \vdots & \vdots & \ddots & \vdots \\ 0 & 0 & \cdots & 1 \end{matrix} \tag{4.62}$$

In such a case $\mathbf{P_k} = \mathbf{P}_{k-1} = \mathbf{I}$ (identity matrix). In this simple case where $\mathbf{A}_k$ is a vector, then solving:

$$\mathbf{A}_k\mathbf{I}\mathbf{A}_k^T = \begin{bmatrix} A_1 & A_2 & \ldots & A_k \end{bmatrix} \begin{bmatrix} 1 & 0 & \ldots & 0 \\ 0 & 1 & \ldots & 0 \\ \vdots & \vdots & \ddots & \vdots \\ 0 & 0 & \ldots & 1 \end{bmatrix} \begin{bmatrix} A_1 \\ A_2 \\ \vdots \\ A_k \end{bmatrix} = A_1^2 + A_2^2 + \cdots + A_k^2 = R^2 \tag{4.63}$$

This resolves in 2-space to a circle, in 3-space to a sphere.

$$\underset{1 \text{ x } n}{\begin{bmatrix} A_1 & A_2 & \ldots & A_k \end{bmatrix}} \underset{n \text{ x } n}{\begin{bmatrix} 1 & 0 & \ldots & 0 \\ 0 & 1 & \ldots & 0 \\ \vdots & \vdots & \ddots & \vdots \\ 0 & 0 & \ldots & 1 \end{bmatrix}} \underset{n \text{ x } 1}{\begin{bmatrix} A_1 \\ A_2 \\ \vdots \\ A_k \end{bmatrix}} \tag{4.64}$$

Replacing the identify matrix with the $\mathbf{P}_{k-1}$that contains non-zero off-diagonal covariance terms "skews" the shape of the circle into an ellipse and a sphere into an ellipsoid. Also note that equation (4.63) always produces a scalar result.

Continuing with the definition of the operation of the Kalman filter, The process proceeds recursively with the calculation of not only the state space equations (4.55) and (4.56), but also computing s the Kalman gain $\mathbf{K}$. The prediction error / covariance matrix $\mathbf{P}$ and Kalman gains $\mathbf{K}$ are computed with equations (4.65), (4.66) and (4.67).

$$\mathbf{K}_k = \mathbf{P}_k^- \mathbf{H}_k^T \left(\mathbf{H}_k \mathbf{P}_k^- \mathbf{H}_k^T + \mathbf{R} \right)^{-1} \tag{4.65}$$

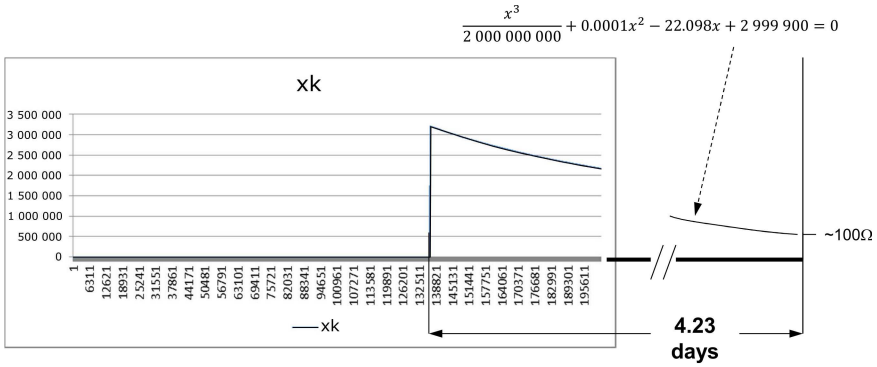

Figure 49: Linear Kalman filter applied to switched impedance

$$\hat{\mathbf{x}}_k = \hat{\mathbf{x}}_k^- + \mathbf{K}_k \left(\mathbf{z}_k - \mathbf{H}_k \hat{\mathbf{x}}_k^- \right) \tag{4.66}$$

$$\mathbf{P}_k = (\mathbf{I} - \mathbf{K}_k \mathbf{H}) \mathbf{P}_k^- \tag{4.67}$$

One advantage of the Kalman filter is its recursive nature which eliminates the need to store any previously sampled values, reducing memory requirements. Furthermore, if each component in the measurement noise vector $\mathbf{v}_k$ is uncorrelated to each other, a simplification is to perform a state update one measurement at a time. This replaces matrix manipulations with scalar math, and in particular, eliminates the need for matrix inversion [44].

4.2.3 Kalman Filter Limitations

While the Kalman filter (really estimator) does produce excellent results (actually optimal) for linear systems, this is not the case for non-linear systems. Consider a system calculating the impedance of a circuit and assume a switching event momentarily opens, then recloses the circuit into the same or different impedance.

Such a switching sequence is shown graphically in figure 49. The line begins with the Kalman filter calculating the $x_k$impedance over the first 135 000 samples trending around 100Ω. Near sample 135 000 the current flow is interrupted and the Kalman estimate of the resistance (within

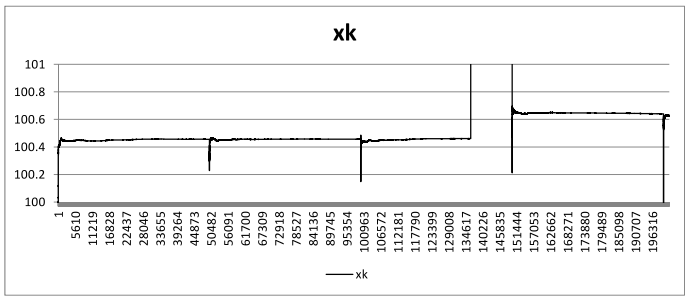

Figure 50: Kalman gain and covariance values recalculated every 50000 samples with optimized (average of previous) coefficients injected after the re-initialization

the resolution of the sensing equipment) tends towards infinity at which point the circuit is reclosed back into nearly the same resistance as before (~100Ω, except increased by ~0.1Ω). As is shown in figure 49, the standard Kalman filter does not deal well with the non-linear switching event. The calculated value of Z (shown as x_k) does not return to a correct value within the remaining time shown on the graph (end of graph approximately at sample 200000, while the transient occurred at approximately sample 138000, at 240 samples/sec. This means that 258 seconds or about 4.3 minutes elapsed from the point of the peak of the transient impedance until the end of the graph at which point the Kalman estimate of $x_k(Z)$ still exceeded 2 MΩ.) Curve fitting and solving for when the calculated value for $x_k$would once again reach 100 Ω, the answer turns out to be over 4 days!

Since actual power systems may experience transients (switching events) on a regular basis, it is clear the basic Kalman filter be discarded, or at least modified, to be useful in this application. While one solution is to use the same Kalman filter, but reinitialize the calculations after a set number of sampled values as shown in figure 50, that method too has obstacles.

Here the filtered value recovers to a nominal value following the transient, but because of the need to reset the Kalman recursive loop (once every 50000 samples or at every 50000 sample interval – at 240 samples/sec this represents about 3.5 minutes), the calculated value is unusable. Also, since the Kalman function is not reinitialized until 50 000 iterations of the state estimation

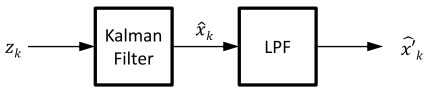

Figure 51: Output of periodically reset Kalman filter post-processed by low pass filter to reduce transient effects

loop are completed, the ability of the algorithm to detect a transient more rapidly (in this cause potentially being delayed 3.5 minutes) is delayed accordingly.

4.2.4 Mode / Median Extension to Kalman Filter

One modification made to the Kalman filter is to apply a low-pass filter to the output of the calculated state, and shown functional in figure 51.

A particularly useful version of the low-pass filter when coupled to the output of the Kalman filter is the mode filter. The mode / median filter examines and records the most common value, largely ignoring the short duration, but high magnitude deviations, providing instead an output that is shows far less transients than the raw Kalman filter output. The flow chart shown in figure shows how it operate.

The mode / median filter shown in the flow chart in figure 52 operates by comparing the most recently calculated Kalman filter output $\hat{x}_k$ with the most recently calculated value $\hat{x}_{k-1}$. If the new value exceeds the previous value, rather than simply passing through the new value, the mode / median filter only increments the previous value by a fraction of an initial value for $\hat{x}_k$. Likewise if the new value is less than the previous value, the mode / median filter subtracts a fraction of the initial value from the most recent value. This works well when the signal remains within a tight range (as impedance will/should).

In effect, this is identical to the Kalman gain calculation with the exception that this gain is not recalculated periodically. After all, it is known that the when the Kalman filter is operating with linear (non-switched) data, it will settle to an optimal estimation of the true value. In this case the next estimate $\hat{x}_k$ will be very close to the previous estimate $\hat{x}_{k-1}$.

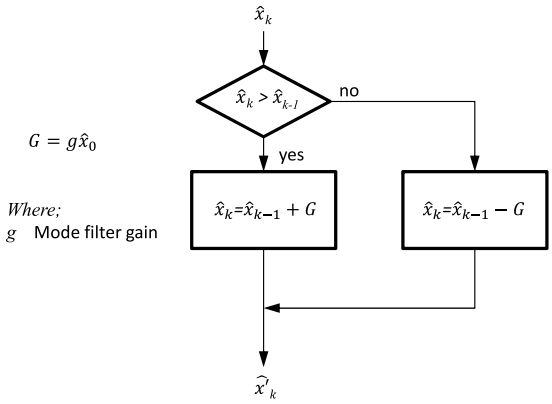

Figure 52: Output of Kalman filter $\hat{x}_k$is input to a mode / median filter with programmable gain g

If, however, a transient occurred (such as recalculating the Kalman coefficients so as to reduce settling time to transient events), then the next several calculated values of $\hat{x}_k$ may deviate widely from the previous value and will oscillate around the previously calculated (true) value of $\hat{x}_k$. The mode / median filter provides an optimal response in that it essentially ignores the magnitude of the deviation thus damping the signal to oscillate ± 1 count around the previously calculated value. Note that this mode / median filter is different than a conventional low-pass filter since the next sample deviation from the previous sample is always a fixed amount, not an amount proportional to the amount of deviation. By limiting the maximum step size when moving from $x[k-1] \rightarrow x[k]$, systems with arbitrarily large variances can be processed. In the realm of power systems, this works well, since systems can have arbitrarily large amounts of power. Waiting for the Kalman filter to settle after being triggered on a high current transient could require extended times.

Figure 54 shows the output of the Kalman filter (thin line) with an overlaid version of the Kalman estimation passed through a low pass filter. The low-pass filter can simulated digitally with either FIR or IIR (FIR chosen here). A simple LP FIR digital filter with a Hanning window ([76]) is shown in equations 4.68 through 4.70 and in figure 53 showing a diagram of an generic FIR filter of order 2.

$$y[k] = \frac{1}{4}\left(x[k] + 2x(k-1) + x[k-2]\right) \tag{4.68}$$

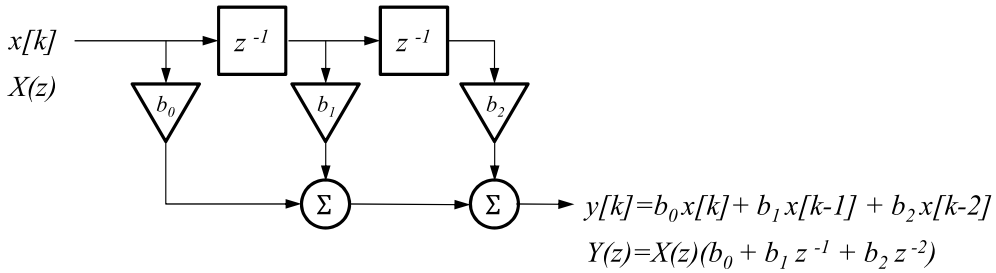

Figure 53: FIR digital filter of order 2

$$H(z) = \frac{Y(z)}{X(z)} = \frac{1}{4}\left(1 + 2z^{-1} + z^{-2}\right) = \frac{(z+1)^2}{z^2} \tag{4.69}$$

$$(z+1)^2 = 0, \text{ therefore } z = -1 \tag{4.70}$$

As equation 4.70 shows, this Hanning implementation has two zeros, both in the left hand plane of the z-plane, confirming that this filter acts as a low pass filter. However, the problem is immediately evident in that while the LPF attenuates the deviations following each of the Kalman coefficient recalculation points, it is also clear from looking at the resultant output in figure 54 that several thousand new state estimation updates are required before the value settles back to the steady value of impedance.

The speed at which the value settles determines how quickly an actual impedance change can be detected.

Figure 54 shows that the transient deviations are substantially reduced by passing the output of the Kalman filter through a LPF. Depending on the desired response time vs the expected magnitude of deviations, this mode / median tuning constant can be adjusted. One aspect of the research that will be done is to examine the non-linear variants of the Kalman filter (Extended Kalman filter and the Unscented Kalman filter).

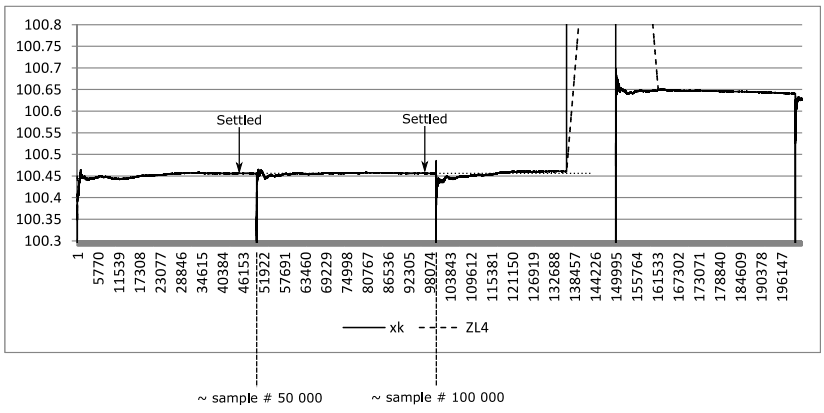

Figure 54: Kalman filter calculation post-processed through low-pass filter (example Hanning)

4.3 IMPROVED FILTER DESIGN

To compare the performance of the Kalman filter to the other filters an experiment was run on a simple dc circuit where the metered values were deliberately chosen to be at or below the noise floor of the chosen instrumentation. The same data was then run through different filters and the performance compared.

Figure 55 shows the first filter attempt based solely on oversampling to negate the random noise. As discussed earlier, this gave an indication of a 0.1Ω change, but such a result would not be sufficient (at 200 sample averages) to provide much better resolution. Certainly not down to the micro-ohm levels of resolution.

The next filter analyzed was the basic Kalman filter. While provide outstanding resolution, the filter is plagued by the inability to deal (in a reasonable time frames – 4 days settling time is not reasonable) with non-linear switching events.

The third filter examined was the Kalman filter with periodically (and selectively) chosen reset commands. The reset causes the Kalman gain to move to larger values (steady state it moves towards 0). While much better than the oversampling filter, and the transients could be ignored (since impedance or resistance changes occur slowly), work continued to find a better smoother filtering method.

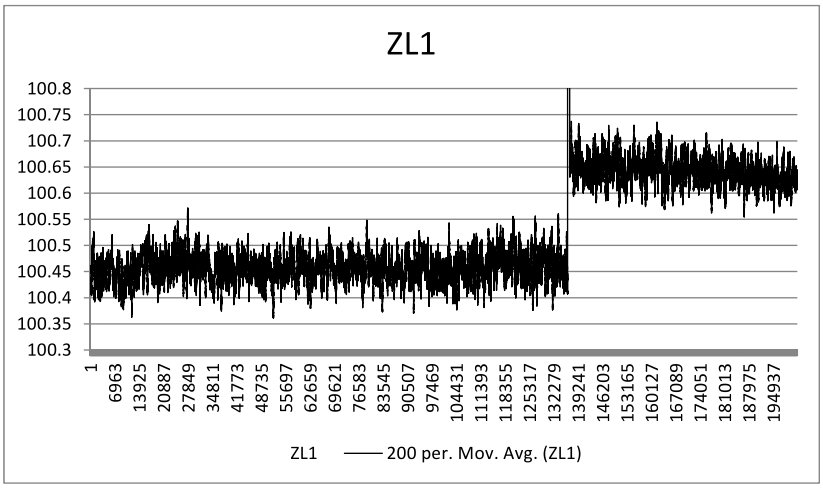

Figure 55: 200 point moving average of calculated Z

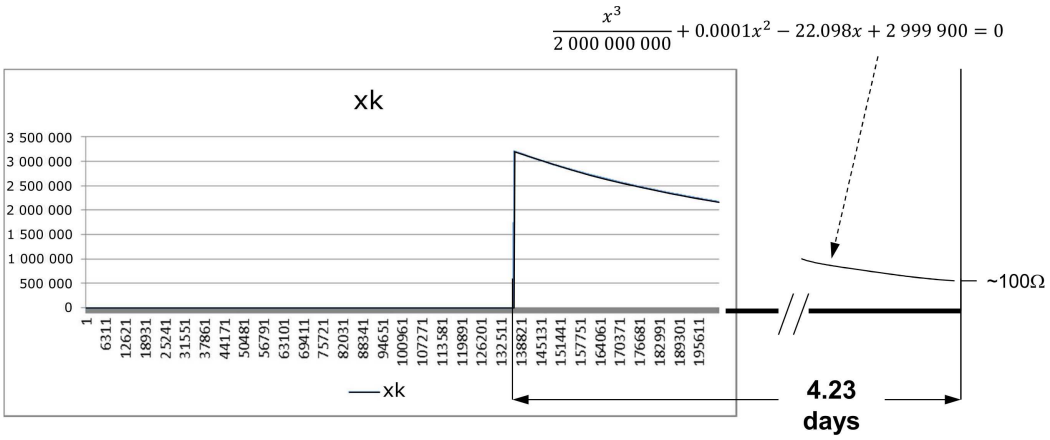

Figure 56: Kalman filter estimation of calculated Z

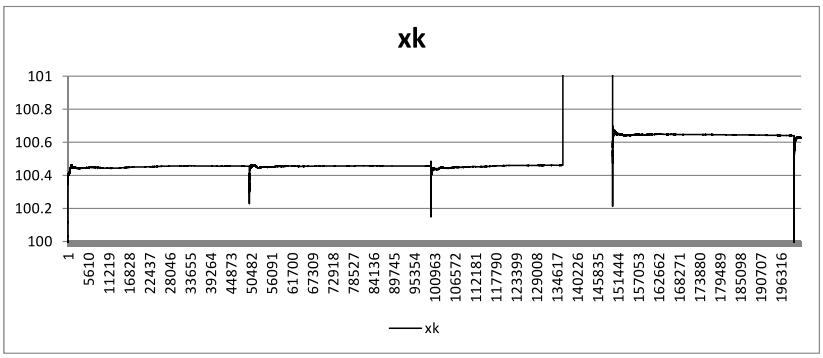

Figure 57: Kalman filter estimation of calculated Z with periodic reset

The fourth filter chosen was the one discussed in figure 51. The output from the third filter (figure 57) is input into a mode / median filter described in figure 52. The transients are nearly completely attenuated, however since the underlying estimator is the Kalman filter, the transient event that occurs near sample 135 000 is incorrectly estimated to return to ~100.6Ω at sample 150 000. In fact, it returned only a few seconds (<1000 samples) after sample 135 000. While this delay of a few minutes is likely not critical for impedance monitoring system, work continued to find a faster filter, but one that still showed outstanding stability.

The fifth filter is a pure mode / median filter. Figure 59 shows a $ZL2$ parameter trended over time with a nearly constant estimate of impedance over time. The jitter in the signal is even less than the Kalman filter, but nonetheless it jumped to the new value within a few seconds, closely tracking the actual process variable.

Figure 59 was a fascinating plot in that it was extremely simple and yet outperformed the presumed best filter (Kalman) in both response time, and stability. In fact, the only two areas along the curve where any deviation in signal were noted were the large step change when the circuit was switched and a smaller bump just prior to the switch. Since the switching involved taking hold of a conductor and pulling it out of a socket, it is possible that this filter even detected the small deviations prior to the actual disconnection!

This sensitivity (similar to Kalman where $K_k \approx 1$) quickly detected a real change in the process variable, but then acted more like the Kalman filter with $K_k \approx 0$ in that the signal essential imme-

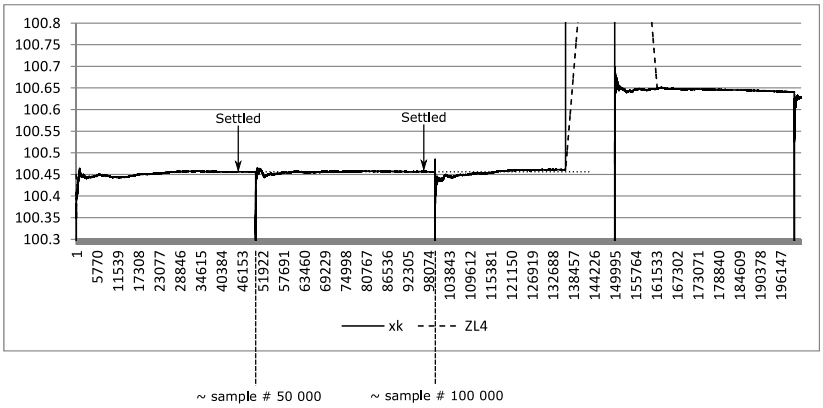

Figure 58: Kalman filter estimation with mode / median post-processing of calculated Z with periodic reset

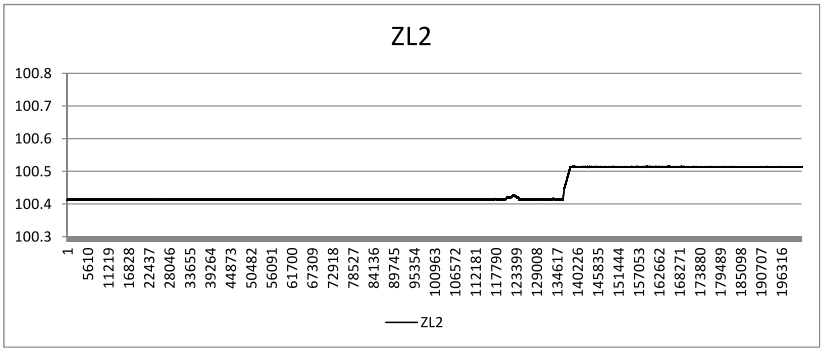

Figure 59: Mode / median (only) of calculated Z

diately settled to a final value. And unlike the Kalman filter, there was no need to add extensions to deal with non-linearities (retriggering / recalculating coefficients a user defined periods). And consider that even these extensions were only partially acceptable in that a time value after each periodic reset message was needed to allow the Kalman filter to settle to a final value. Too frequent reset messages would not have provided enough time for the algorithm to settle to a final value. On the other hand, sending reset messages too infrequently meant that transient events would be missed require even more time to settle.

This special mode / median filter appears to solve both problems and was a nice surprise as an outcome of this research.

5.0 PRECISION PHASE ANGLE ESTIMATION

During this analysis mathematical models were developed, computer simulations run and circuit tests were performed and compared. An interesting artifact came from comparing some of the theoretical calculations of impedance and of the supposedly similar (but not) test results. One of the differences came from the issue that when calculating the $R + jX$ values of impedances connected in parallel, when those parallel reactive elements included resistances (as they also always do), skewed the conventional *RLC* impedance and resonance calculations slightly. In effect the resistance allowed re-tuning not only the X/R ratio (and therefore the circuit Q) but also the resonance point f_r and the effective total Z_{eff}, R_{eff}, and X_{eff}. Finding the exact value of the effective impedance of the combined elements was more complicated than simply paralleling R, L, and C elements and solving for the combined impedance.

5.1 PARALLEL VERSUS SERIES RLC SYSTEMS

This was important since measurements of phase angle between voltage and current waveforms along with measured impedance (ratio of V_{rms}/I_{rms}) do not directly lead to discovery of underlying separate R and X values of each parallel element. While simple series *RLC* circuit *can* be analyzed in the manner, typical power systems include several parallel elements, each with R, L, and C components. Also, as outlined in Appendix A, measuring the slope of the instantaneous impedance provides valuable information regarding direction to a fault. Since that method for resolving fault location relies on examination the slope (first derivative) of this calculated pseudo-impedance over time (which to the eye creates a particular "shape"), factors that distort this slope must be considered and analyzed. One factor is resonance. Capacitors sized for power factor correction typically

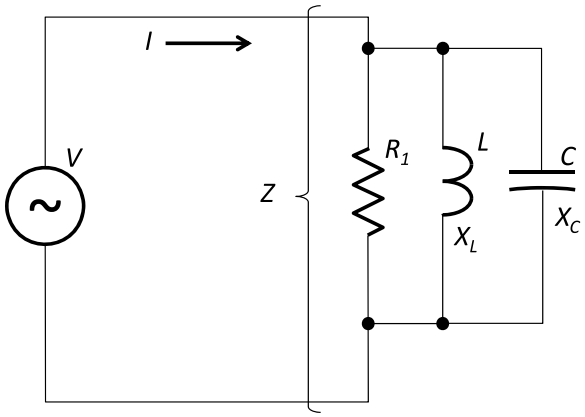

Figure 60: Parallel RLC circuit with no resistance in series with capacitor

do not induce resonance at fundamental power frequencies (otherwise they would self-excite), but frequently *do* excite resonances at harmonic multiples of the power frequencies.

A Fourier decomposition of a non-linear transient such as mechanical or electronic switching or rectification will reveal energy at these harmonic frequencies above the power frequency. Such a decomposition usually includes a broad spectrum of frequencies, typically odd order, but if magnetic elements are included can also include even harmonics. Once a resonance near one of these frequencies is excited, oscillations between the system inductance and the system capacitance occur. These oscillations superimpose a ring waves on top of the power system frequency, changing the instantaneous slope of the measured current (and possibly voltage depending on the source impedance) which results in the same frequency oscillations being superimposed on the calculated pseudo-impedance $z1(t)$ (see Appendix A). Recalling the goal is to develop an algorithm that detects fault location while minimizing the processing required, the question must be asked is what minimum level compensation must be applied to deal with these oscillations?

Using the schematic shown in figure 60 the equation for resonance is written as simply the point at which $X_L = X_C$.

$$2\pi f_r L = \frac{1}{2\pi f_r C} \tag{5.1}$$

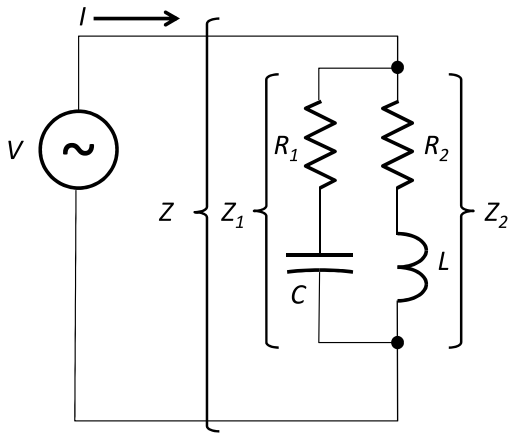

Figure 61: Power factor correction circuit with two separate resistances

$$f^2 = \frac{1}{4\pi^2 LC} \tag{5.2}$$

$$f_r = \frac{1}{2\pi\sqrt{LC}} \tag{5.3}$$

For most texts this is the equation shown. But recall that the conductors connecting the capacitor are not zero resistance. Including the proper resistance value in the capacitor conductors (figure 61) changes the equation for resonance (and impedance) accordingly.

A more general diagram that includes a separate parallel R element in parallel with the two reactance + resistance elements (figure 62).

The process to solve for the effective X and f_r (equation 5.3) values of such a system begins with substituting $R_L + jX_L$ for jX_L alone and $R - jX_C$for $-jX_C$ and solving for Z_{eq}:

$$Z_{eq} = \frac{Z_L Z_C}{Z_L + Z_C} = \frac{(R_L + j\omega L)\left(R_C - \frac{j}{\omega C}\right)}{(R_L + R_C) + j\left(\omega L - \frac{1}{\omega C}\right)} \tag{5.4}$$

Since:

$$Z_{eq} = R_{eq} + jX_{eq} \tag{5.5}$$

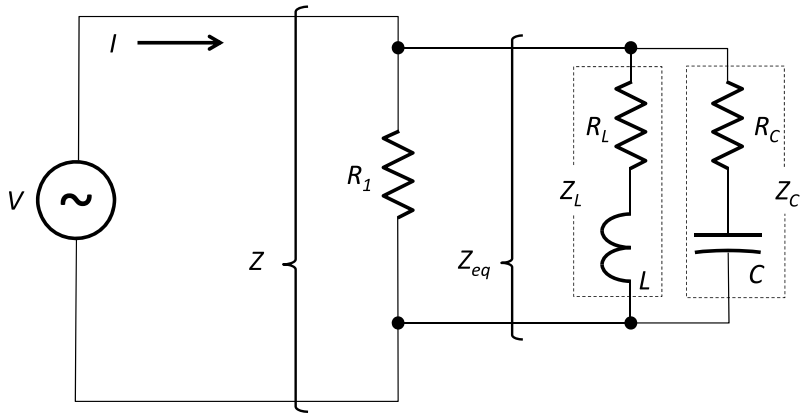

Figure 62: Parallel RLC circuit with resistance shown in series with capacitor

Equation 5.5 is shown schematically in figure 63. Using the method outlined in [68], the real and imaginary components can be isolated (rationalized) :

$$R_{eq} = \frac{\left(R_L R_C + \frac{L}{C}\right)(R_L + R_C) + \left(\omega L R_C - \frac{R_L}{\omega C}\right)\left(\omega L - \frac{1}{\omega C}\right)}{(R_L + R_C)^2 + \left(\omega L - \frac{1}{\omega C}\right)^2} \tag{5.6}$$

$$X_{eq} = \frac{\left(\omega L R_C - \frac{L}{C}\right)(R_L + R_C) + \left(\omega L R_C - \frac{R_L}{\omega C}\right)\left(\omega L - \frac{1}{\omega C}\right)}{(R_L + R_C)^2 + \left(\omega L - \frac{1}{\omega C}\right)^2} \tag{5.7}$$

5.2 MORE ACCURATE EQUIVALENT R AND X CALCULATIONS

Looking at figure 63, the equation for Z can be written by inspection:

$$Z = \frac{R_1\left(R_{eq} + jX_{eq}\right)}{R_1 + \left(R_{eq} + jX_{eq}\right)} \tag{5.8}$$

$$Z = \frac{R_1 R_{eq} + jR_1 X_{eq}}{\left(R_1 + R_{eq}\right) + jX_{eq}} \tag{5.9}$$

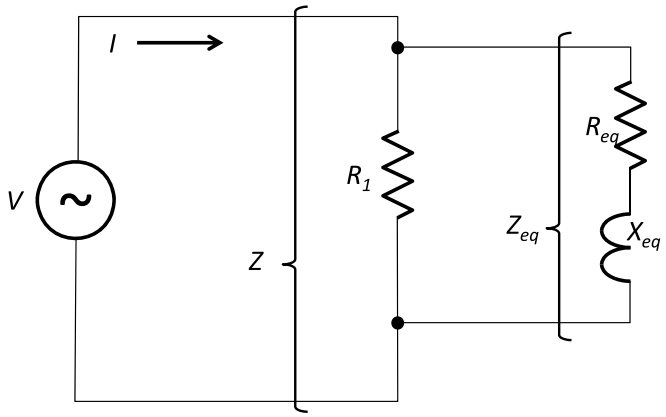

Figure 63: Simplified figure combining X_L and X_C elements into a common X_{eq} 62

Multiplying the denominator by its complex conjugate, the rationalization step is performed again:

$$Z = \frac{R_1 R_{eq} + jR_1 X_{eq}}{(R_1 + R_{eq}) + jX_{eq}} \cdot \frac{(R_1 + R_{eq}) - jX_{eq}}{(R_1 + R_{eq}) - jX_{eq}} \tag{5.10}$$

$$Z = \frac{R_1 R_{eq} X_{eq}^2}{(R_1 + R_{eq})^2 + X_{eq}^2} + j\frac{(R_1 + R_{eq}) R_1 R_{eq} X_{eq}}{(R_1 + R_{eq})^2 + X_{eq}^2} \tag{5.11}$$

$$R_{eq2} = \frac{R_1 R_{eq} X_{eq}^2}{(R_1 + R_{eq})^2 + X_{eq}^2} \tag{5.12}$$

$$X_{eq2} = \frac{(R_1 + R_{eq}) R_1 R_{eq} X_{eq}}{(R_1 + R_{eq})^2 + X_{eq}^2} \tag{5.13}$$

$$X/R = \frac{X_{eq2}}{R_{eq2}} \tag{5.14}$$

The equivalent values of load inductance L and load resistance R can now be calculated.

$$\begin{cases} \text{if } X_{eq2} > 0 & L_{eq2} = \frac{X_{eq2}}{\omega} \\ \text{else} & C_{eq2} = \frac{1}{\omega X_{eq2}} \end{cases} \tag{5.15}$$

$$PF = cos\left(tan^{-1}\left(\frac{X_{eq2}}{R_{eq2}}\right)\right) \tag{5.16}$$

It is clear from examining equation 5.16 that the real portion of the power factor depends on the equivalent L and C values, but also on the values of the three resistances. Also, by inspection is is clear that $L_{eq2} \neq L$ and $C_{eq2} \neq C$, therefore calculated values such as resonance frequency using equation 5.3 are now recognized as being only approximations. While likely clear, it is important to emphasis that the X/R ratio and power factor of such a circuit no longer are simply calculated (that tends to be what is shown in textbooks).

$$R_{eq} \neq R_1 \tag{5.17}$$

$$X_{eq} \neq 2\pi fL - \frac{1}{2\pi fC} \tag{5.18}$$

Instead:

$$R_{eq} \rightarrow R_{eq2} = \frac{R_1 R_{eq} X_{eq}^2}{\left(R_1 + R_{eq}\right)^2 + X_{eq}^2} \tag{5.19}$$

$$X_{eq} \rightarrow X_{eq2} = \frac{\left(R_1 + R_{eq}\right) R_1 R_{eq} X_{eq}}{\left(R_1 + R_{eq}\right)^2 + X_{eq}^2} \tag{5.20}$$

All this is to say that the values chosen for power factor capacitors are only approximations of the exact values needed to compensate to a particular value. The important take-away with respect to the calculation of pseudo-impedance (Appendix A) when measuring circuits with resonance frequencies near common power system harmonics is that these more detailed equations should be used. While the goal of any distribution system designer should be to reduce losses as much as practical, the reality is that wire with non zero resistance will be used and as shown above this wire affects the power factor and resonance.

Also, these equations explain the previously unexplained deviation between LTSPICE simulations and the simplified equations for resonance. Another point of potential error is in the common

equations used to calculate the equivalent reactive power available (kvar) from a particular capacitor at a particular voltage and frequency.

$$Q = var = \frac{V^2}{|X_{eq2}|} \tag{5.21}$$

$$S = VA = \frac{V^2}{|Z|} \tag{5.22}$$

Hopefully this will help others explain small deviations between their hand calculations and their computer simulations.

5.3 SECONDARY EFFECTS

One final interesting point to mention refers all the way back to figure 40. In the last (bottom) image the two conductors were under so little pressure that the two conductors were barely touching. It was mentioned in the text in that section, that the current concentrates over fewer and fewer connections, raising the current density and therefore the temperature. As the current density increases to the point where the temperature reaches the boiling point of the underlying metal, the current continues to flow through the air.

Now normally, as the current in a conductor increases, the resistance increases. This holds true for pressure junctions too, although if that junction starts to create a series arc, the arc intensity increases as the current increases. This *decreases* the resistance of the arc, resulting in an apparent "negative" resistance (current increases and voltage drop decreases). While this tends to mask the degradation (since the resistance of the failing junction begins to drop – normally an indication of a *good* junction), this negative resistance is distinguishable from V versus I plots on adjacent phases with the same physical properties. The current through the phase with the negative resistance element will show flat topping where the voltage drop decreases as the current increases. The relative increase in resistance for the phase conductor that includes the glowing/arcing pressure junction will not be as much as adjacent conductors with same physical properties passing the same current.

This factor needs to be considered, but the suggested solution is to monitor the frequency content of the current. Arcs produces wide-spectrum noise that when detected and combined with the appearance of "flat-topping[1]" of the impedance trend plot provide strong evidence of a severely degraded (near failure) connection.

[1]Flat topping implies that the impedance over time has trended up, then plateaued.

6.0 FUTURE RESEARCH

6.1 PRECISION FAULT LOCATION

Using the techniques described here (and in Appendix A), locations of circuit failures can be determined. What these methods do no provide is precision location of the failure. Several methods are proposed for continued research.

- Time Division Reflectometry (TDR)
- Frequency Division Reflectometry (FDR)
- Harmonic Energy Ratio Detection (HERD)

Accurate time-stamped data from devices with timing resolution similar to phasor measurement units could feasibly provide triangulation data from an event that was detected by two or more IEDs with this capability. Similar to the TDR/FDR techniques used to detect the location of a faulted communication line, this method would measure the time difference between the voltage and current transient signals from multiple-devices. A difference would be that unlike the TDR/FDR methods whereby the metering device generates the test signal, this proposed method would operate more like passive sonar and use the signals generated by the fault. Consider seismographs that measure the time difference between the P and S waves to locate the hypocenter / epicenter of an geologic event. [82]. Arcing events at failing series connections would produce both a noise signal in voltage and current, with the delay in the current signal being a measurement of the energy storage between each metering devices and the developing failure. It is possible that a characteristic

model could be developed that maps these impedances, compares the timing between the V and the I signals from that arc, and makes a determination of direction based on known attenuation from these maps.

This topic is explored more thoroughly in the next section discussing HERD.

6.1.1 Harmonic Energy Ratio Detection (HERD)

This is a new term to describe a proposed method of detecting the distance to a fault. It works under the principal that metering devices using the method described earlier can calculate the bus $R + jX$ to a high precision. Furthermore, it is understood that the impedance (and admittance) of these buses varies by the frequency of the forcing function (e.g. arc, switching event, etc.). By calculating separate impedances at each frequency and comparing how those impedances change pre- and post-event, mathematically a metric related to the magnitude of impedance between the IED and the fault can be more precisely calculated. Since as with distance relays, knowledge of the system allows converting impedance to distance, this method would create a method to determine the "electrical distance" to the arcing circuit.

The way this would operate is during steady state operation, the ratio of the differences in the impedance at each frequency would be calculated. A "harmonic amplitude difference" would represent the change in that harmonic impedance during a fault. This difference would be compared to the nominal harmonic impedances at all frequencies prior to the event. As higher frequency signals are attenuated to a greater level, a distance can be inferred based on attenuation of different frequencies such that when combined with the precise timing provided by the multiple IEDs with PMU-like time stamps, this new data set can supplement the fault location detection algorithm described here.

The proposed equations are listed below.

Rewriting equation (3.15):

$$\mathbf{I} = \mathbf{Y}_{bus} \cdot \mathbf{V} \tag{6.1}$$

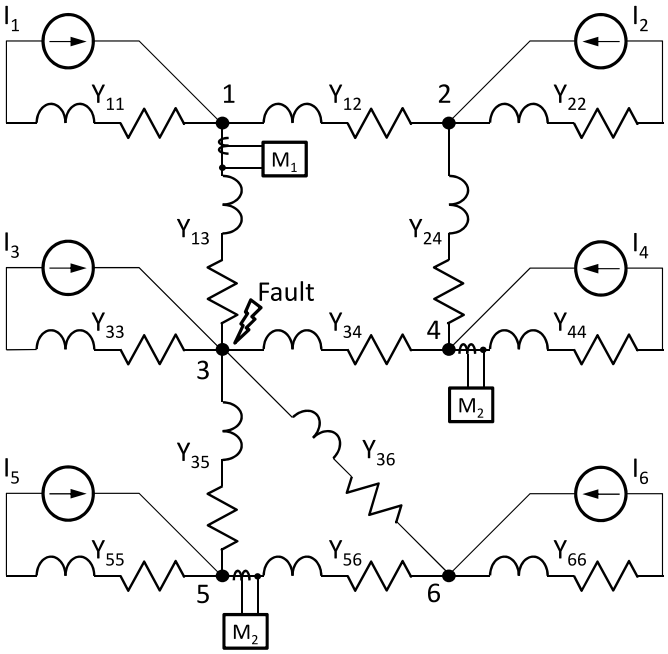

Figure 64: Fault detection within mesh admittance network using sparse metering

$$\mathbf{Y}_{bus} = \begin{bmatrix} Y_{11}+Y_{12}+Y_{13} & -Y_{12} & -Y_{13} & \cdots & \cdots & \cdots & \cdots \\ -Y_{12} & Y_{12}+Y_{22}+Y_{24} & -Y_{23} & \cdots & \cdots & \cdots & \cdots \\ -Y_{13} & -Y_{23} & Y_{13}+Y_{33}+Y_{34}+Y_{35}+Y_{36} & \cdots & \cdots & \cdots & \cdots \\ 0 & -Y_{24} & -Y_{34} & \cdots & 0 & 0 & 0 \\ 0 & 0 & -Y_{35} & \cdots & -Y_{24} & 0 & 0 \\ 0 & 0 & -Y_{36} & \cdots & -Y_{34} & -Y_{35} & -Y_{36} \\ & & & \cdots & Y_{24}+Y_{34}+Y_{44} & 0 & 0 \\ & & & \cdots & 0 & Y_{35}+Y_{55}+Y_{56} & -Y_{56} \\ & & & \cdots & 0 & -Y_{56} & Y_{36}+Y_{56}+Y_{66} \end{bmatrix} \tag{6.2}$$

$$Y_{ij} = G_{ij} + jB_{ij} \tag{6.3}$$

$$G_{ij} = \frac{R_{ij}}{R_{ij}^2 + X_{ij}^2} \tag{6.4}$$

$$B_{ij} = -\frac{X_{ij}}{R_{ij}^2 + X_{ij}^2} \tag{6.5}$$

$$Y_{ij} = \frac{R_{ij}}{R_{ij}^2 + X_{ij}^2} + j\left(-\frac{X_{ij}}{R_{ij}^2 + X_{ij}^2}\right) \tag{6.6}$$

$$\angle Y_{ij} = \tan^{-1}\left(\frac{B_{ij}}{G_{ij}}\right) = \tan^{-1}\left(-\frac{X_{ij}}{R_{ij}}\right) \tag{6.7}$$

$$X_{ij}(\omega_n) = \omega_n L_{ij} \tag{6.8}$$

Looking at one bus and recognizing that the effective impedance is a root mean square of the values computed at each frequency component contained in the current. Since the total current is equal to the rms summation of each of the harmonic currents, then the equations for the current can be written as:

$$I_{rms} = \sqrt{I_1^2 + I_2^2 + I_3^2 + I_4^2 + I_5^2 + \cdots + I_N^2}\text{ , where N = max harmonic \#} \tag{6.9}$$

$$I_i = Y_{i1\omega_1}V_1 + Y_{i2\omega_1}V_2 + \cdots + Y_{1k\omega_1}V_k \text{ where } k = \text{\# of voltage sources} \tag{6.10}$$

$$Y_{i1\omega_1} = \frac{I_i - (Y_{i2\omega_1}V_2 + \cdots + Y_{1k\omega_1}V_k)}{V_1} \tag{6.11}$$

$$\begin{aligned} Y_{i1\omega_1} = \frac{1}{V_1}\Bigg(& \sqrt{I_{i\omega_1}^2 + I_{i\omega_2}^2 + I_{i\omega_2}^2 + I_{i\omega_3}^2 + I_{i\omega_4}^2 + \cdots + I_{i\omega_N}^2} - \\ & \left(\frac{R_{ij}}{R_{ij}^2 + X_{ij\omega_1}^2} + j\left(-\frac{X_{ij}}{R_{ij}^2 + X_{ij\omega_1}^2}\right)\right)V_2 + \cdots \\ & \cdots + \left(\frac{R_{ij}}{R_{ij}^2 + X_{ij\omega_1}^2} + j\left(-\frac{X_{ij}}{R_{ij}^2 + X_{ij\omega_1}^2}\right)\right)V_k\Bigg) \end{aligned} \tag{6.12}$$

These are only preliminary equation, but since we know the phase angle of each element of the admittance matrix (equation 6.7), the remaining work effort would be to develop a correlation equation that would compare the calculated value of $Y_{i1\omega_1}$ both before and after the event.

$$d = f\left(\frac{\left(\sqrt{\frac{\sum_{\omega=\omega_1}^{\omega_N} Y_{i1\omega_1}}{N}}\right)_{post-event}}{\left(\sqrt{\frac{\sum_{\omega=\omega_1}^{\omega_N} Y_{i1\omega_1}}{N}}\right)_{pre-event}}\right) \tag{6.13}$$

Where:

d Ratio related to distance to the fault based on this HERD (Harmonic Energy Ratio Detection) method

6.2 CABLE INSULATION, SPD AND ARRESTER DEGRADATION LOCATION

The procedures described throughout this research describe method that accurately measures an impedance that included a resistance very close to zero. This was valuable since it provided a method of measuring degradation discontinuous points along the circuit path (e.g. cable terminations, circuit breaker contacts, LTC contacts, etc.).

$$Z_{series} = R_{series} + jX_{series}, \text{ where } R_{series} \approx 0 \pm \varepsilon_1 \tag{6.14}$$

$$\frac{1}{0 \pm \varepsilon_1} = \infty \pm \varepsilon_2 \tag{6.15}$$

Since it has been shown that Z_{series} and R_{series} can be calculated, and recognizing that R_{series} is a very small value $(0 \pm \varepsilon_1)$, then it follows that the reciprocal of R_{series}could be calculated to an equal precision. Such a calculation would measure a number that approaches infinity. The ability to measure parallel "infinite" (insulation) resistance precisely would be the complementary algorithm to the series resistance failure detection problem.

$$Z_{parallel} = R + jX, \text{ where } R \to \infty \tag{6.16}$$

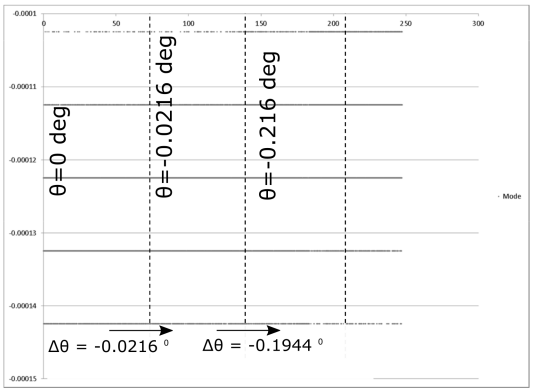

Figure 65: Fractional degree phase angle shift detection is not visible on raw capture of cycle to cycle timing

Therefore, the expectation is that this same method of measuring the reciprocal of a precision R_{series} along with the corresponding power factor $\left(\cos\left(\tan^{-1}\left(\frac{X_{series}}{R_{series}}\right)\right)\right)$ will be used to locate circuits with failing SPDs or arresters, insulation systems, bushings, VTs / PTs and other devices that have full phase voltage applied across them. The nearly spectacular phase angle resolution detected is not visible in raw cycle-to-cycle timing (see figure 65), but when passing through the median / mode filter, clear deviation of just under two tenths of a degree in phase angle are visible.

For example, figure 66 notice the shift from the second column (marked $\theta = -0.0216^0$) to the third column (marked $\theta = -0.216^0$) for a change in phase angle of $\Delta\theta = -0.1944^0$. At 60 Hz, 0.1944 degrees represents a timing resolution of 9 μs!

More research is needed to validate this hypothesis that this algorithm can provide a sensitive insulation monitor, but preliminary results shows that a small modification to the algorithm produces substantially improved resolution, and makes the median / mode filter even more precise. Figure 67 shows the results of an interesting modification to the algorithm that boosted sensitivity such that a 100 nA change in current was measured correctly by an A/D input with a 1 mA resolution, or 10 000 times greater resolution. This has been an exciting finding and further research is being done to create an insulation degradation detector. The details of this higher resolution

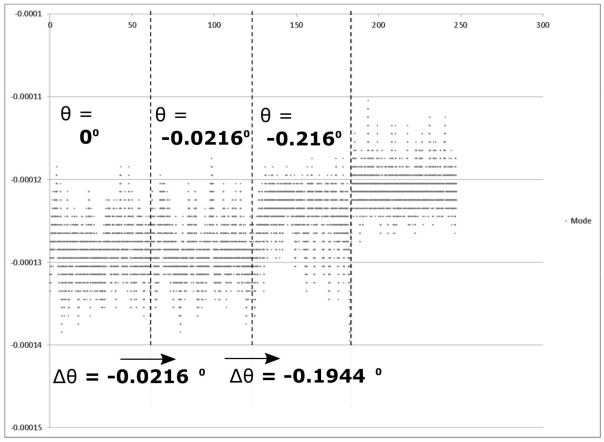

Figure 66: Fractional degree phase shift is visible when passed through median / mode filter

analysis technique (over and above the median / mode technique) will be left to a future paper, but this finding is expected open up a whole new group of predictive diagnostic methods for electrical distribution circuits.

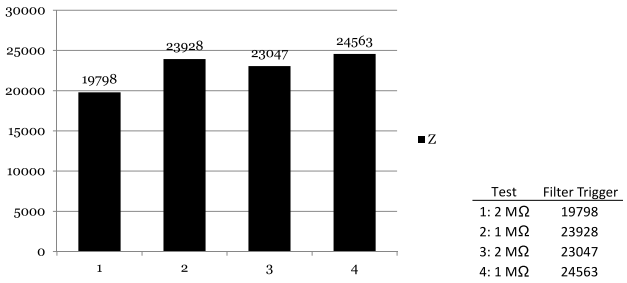

Figure 67: Insulation failure detection using special post-processing added to mode / median filter to detect ~100 nA change in dc charging current

APPENDIX A

SIMPLIFIED ALGORITHM FOR ANALYSIS OF FAULT DIRECTION

Fault direction algorithms are well-known and available for a variety of applications. Here a new algorithm is theorized, modeled and tested that provides excellent performance, while requiring far fewer computational resources or phase measurement (timing) accuracy. The expectation is that with simpler computational and data collection requirements, the algorithm can be installed on devices with fewer resources. This may permit fault direction capability to be installed on more devices. With more fault direction finders on the power distribution system, the location of the fault can be isolated with even greater precision, potentially reducing outage duration.

A.1 INTRODUCTION

The need to locate and isolate faults dates to the earliest days of electrical systems. While the earliest power systems (late 1800's) were much simpler, they all featured what we might term isolated distributed energy sources connected to local customer loads.

Eventually this type of "1-generator per system" expanded to interconnect multiple generators with an ever larger pools of loads. Tying groups of generators together added redundancy. However, connecting loads together also added the advantage of load diversity to average out the peaks and valleys of disparate loads. With more loads connected, the ratio of peak to average loading decreased. With lower peak requirements, generator over-sizing could be reduced, reducing capital equipment costs. As these benefits become more well-known, systems expanded to the very

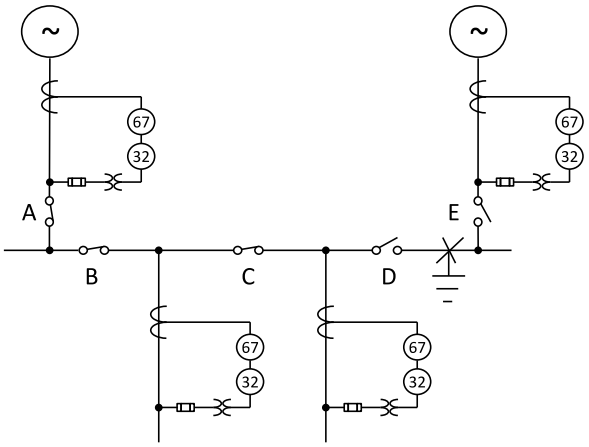

Figure 68: Fault selectively causes switches D and E to open. Switches A, B and C remain closed maintaining power to loads

large regionally connected systems common today all featuring large generation interconnected with loads via a meshed transmission system.

Today, we see a bit of a deviation in this pattern. With the growing popularity, and even mandate, of alternative energy sources, utility systems are again looking like the power systems of yesteryear, with more, and smaller, generators scattered throughout the system. While potential for bidirectional power flow complicates protection and the non-dispatchable nature of the sources (e.g. solar PV, wind) complicates control and stability, one of the potential promises of such a system is the ability to intelligently island loads into separate "micro-grids". With distributed generation closer to the load, it becomes easier to imagine that a portion of the grid could separate from a faulted system and still continue to provide power the local loads.

Of course such a system requires that faults be detected and switches be operated to intelligently isolate these faults. Such a switching scheme implies that there is a mechanism to determine the accurate location of a fault. While there are many methods of isolating faults, a first pass simplification in detecting a fault location is to determine if it exists "upstream" or "downstream" from a particular metering point.

There are many common methods for detecting a such a fault. Choices range from simple electromechanical methods[79] to more complex algorithms[20, 22, 25, 31, 32, 33, 37, 38, 42, 70,

75, 78, 84, 87, 89, 90]. The more complex algorithms offer improved resolution and accuracy by employing more sophisticated mathematics including artificial neutral nets, wavelet analysis and other advanced mathematical constructs. These methods do provide improved performance, but their computational overhead may limit their usage when designers attempt to apply them within low-cost protection or metering devices more commonly applied on distribution circuits. Furthermore, in systems where cost saving measures to improve the return on investment are already closely scrutinized, adding costly instrumentation may not be supported by the project's investors.

For these reasons, low complexity (and therefore low-cost) method of detecting fault locations quickly (within 1/2 cycle) would be very desirable.

A.2 EXISTING FAULT DIRECTION ALGORITHMS

Designers of protective relaying have a large number of fault direction algorithms from which to choose[14]. When examining these methods, nearly all the most commonly used can be categorized as either using directional (current or power) relaying or impedance (distance) relaying or some variation of both.

A.2.1 Directional Relaying

Over-current devices that also measure direction of the current flow work well with loop, mesh, network or radial system that include distributed generation. Commonly employed in combination with distance (impedance) relaying, directional elements infer fault location when the assumption is made that a fault's low impedance would cause a current reversal in a bus.. Figure 69 shows current flows during faults at two locations on a system with three generators. The direction of the current flowing through each protective device reverse during certain faults to indicate whether the fault is up or downstream from a particular protective relay.

Also, as power system engineers understand well, the term "directional current" does not have meaning when that current is measured in isolation from other signals. However, when that current is measured at a particular phase angle relative to the voltage, power flow can be determined.

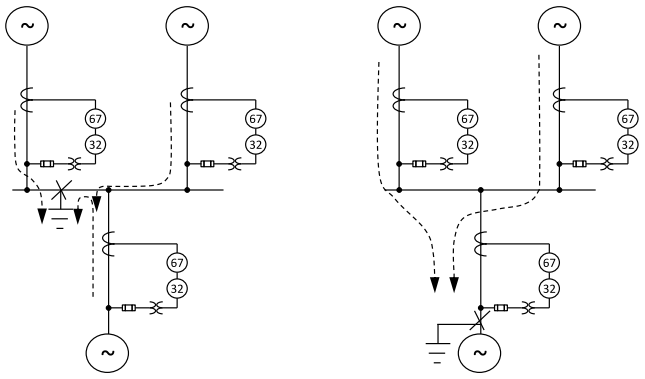

Figure 69: Directional fault current (IEEE device 67) and power (IEEE device 32) isolating fault location

Therefore, directional current means the present current is flowing during a time when the power flow is moving in a particular direction. In the case of forward real power flow, this implies that the phase angle of the current relative to the phase voltage is less than ± 90 degrees. Since this phase angle against the voltage signal must be determined, even relays that only report current (e.g. IEEE device type 67 directional over-current), must also measure voltage. Figures 70, 71, 72 and 73 provide a tutorial review of the correlation between the relative phase angle displacement of the voltage and current versus time waveforms with the corresponding direction of real and reactive power flow [58]. Since directional current sensing requires phase angle, these relays use various methods to determining phase shift (phase locked loop, zero crossing, induction disk, etc.), each with advantages and disadvantages. For example, the zero crossing method is not used with distorted waveforms that may include multiple zero crossings. Phase locked loops are accurate, even with distorted waveforms, but require more digital signal processing. Depending on the signal, harmonic filtering, i.e. digital filtering, may be required and also increases the computational complexity.

As stated earlier, directional current sensing works well when there is a source of energy (or stored energy in devices such as rotating equipment) downstream of the metering point. This stored energy can cause a momentary reversal in real power flow that can feed energy into an upstream fault. For systems without downstream energy sources (or if the source is offline, such as

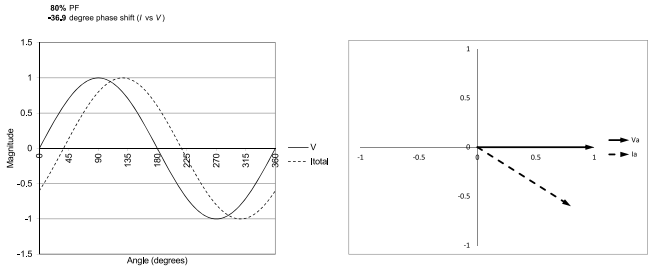

Figure 70: Forward power, positive power factor (I lags V)

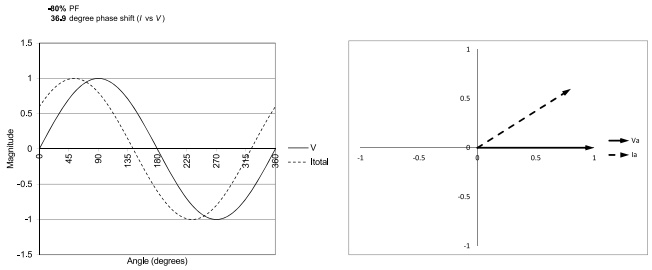

Figure 71: Forward power, negative power factor (I leads V)

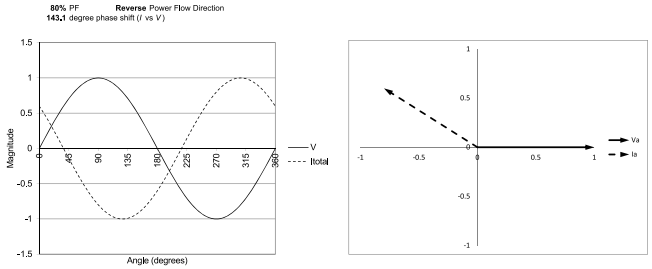

Figure 72: Reverse power, positive power factor

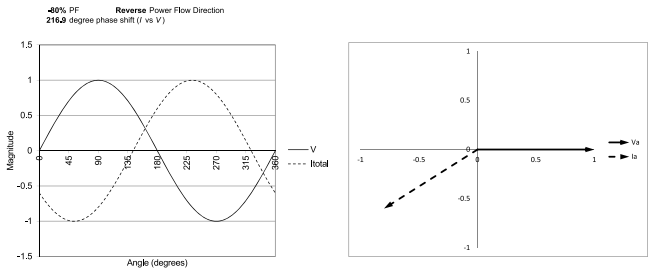

Figure 73: Reverse power, negative power factor

with intermittent solar or wind powered generators), no such downstream source is available and another techniques are needed to determine fault direction. This complicates the use of directional current sensing in micro-grid power systems that include intermittent energy sources.

A.2.2 Impedance (Distance) Relaying

Distance relays operate by calculating the impedance to the fault. With knowledge of certain physical properties of the circuit (conductor size, spacing, layout, type and resistance), the impedance measured can be converted to a distance to the fault. These systems work very well for direct line-to-line faults, but less well for arcing and/or ground faults (due to uncertain impedances in series with the conductors). Also, distributed energy sources can make a line appear to have a different impedance depending on how much energy is being produced downstream of the distance relay at the time of the fault. These issues may cause these protection schemes to over- or under-reach their intended zone of protection. Nevertheless, this technique is considered a state-of-the-art method for locating faults. Many research efforts have continued to improved distance relaying accuracy [14, 75, 37]. When installed on systems that experience bi-directional current flow and are monitored with directional current elements, the distance relay's reach can extend up- or down-stream from the relay's location.

But, as mentioned during the discussion of directional relaying, distance relays only "reach" downstream (in the sense of current flow), so an impedance relay normally must have a source of energy upstream that forces current through the relay to measure impedance to a downstream fault.

Likewise, if generation sources are always available downstream, then distance relays likely will be able to measure impedance to a fault upstream too. However, if the energy source downstream from the protective device is intermittent, then this method does not address the problem of intermittent energy sources removing reverse current flow through a metering device .

This paper proposes a slight modification to how the impedance relay is used to address the problem. This method doesn't rely on directional current relaying techniques and so simplifies the computation requirements by eliminating the need to calculate phase angle.

A.3 SIMPLIFIED BI-DIRECTIONAL FAULT DIRECTION ALGORITHM

Here a method is proposed to work around the problem of not being able to use directional current relaying on switched or intermittent sources of energy (e.g. solar or wind generators) common on islanded micro-grids. The solution proposed is to use a derivation of the impedance relay. Whereas a conventional distance relay only measures impedance to a fault for forward current flow through the relay, this proposed fault direction algorithm uses that limitation to build a logic state machine to eliminate the possibility of the fault being downstream, and therefore recognize that the fault is upstream of the metering point. In other words, as with ordinary impedance relays, the detection method can only look at faults downstream. Any suitable voltage disturbance $(dv(t)/dt)$ triggers the examination of the impedance. If the impedance drops, indicating a downstream fault, the algorithm alerts as such. If no change in impedance is noted, the algorithm notes the lack of change in downstream impedance and reports that the fault is understood to be upstream of the relay.

The simplified algorithm begins by assuming that interval data for both phase voltage and current are available. Step 1, then of the algorithm is to calculate a sample-by-sample ratio of the change in voltage to a change in current. This results in a proxy measurement of the impedance, starting from that point to the load, that completely ignores the phase angle between the signals. This is summarized in equation A.1.

$$z1(t) = \frac{v(t) - v(t-1)}{i(t) - i(t-1)} \tag{A.1}$$

While a more conventional calculation would measure the ratio of the magnitude of the calculated rms values of the voltage and current, this isn't strictly necessary for our purposes. Recall that rms method requires squaring, summing, dividing and finding the square root of a time series of voltage and current signals. While not difficult, by eliminating this requirement, calculations are sped up. Certainly, if our goal is to determine whether the fault is up- or downstream from the metering point, and therefore use that knowledge to isolate the faulted section, faster detection speed is desired.

A.3.1 Detailed Method

As discussed earlier, the goal was to develop an algorithm that:

- Accurately categorized fault location as being either up or downstream from the metering point and
- Was computationally simple and could be included within practically any device that could measure voltage and current

To validate performance over as wide a grouping of circuit types as possible, real-world circuit tests were augmented with simulations built in LTSPICE [28]. The simplest simulation included a single utility source with an simple distributed generation system feeding a modest 10A load operating at an 80% power factor $(X/R = 0.75)$. Faults were placed both upstream and downstream of the metering device and voltage and current waveforms were captured. Other simulations change the load power factor, connected or disconnected the distributed generation and added or removed power factor correction capacitors.

As previously stated, while impedance is found by dividing the rms value of voltage by the rms value of the current, the method described here used an interesting approximation. Since equation A.1 skips the rms calculation step and also ignores the phase angle, certainly such a calculation would not seem to provide a precise fault location determination. What do the simulations show?

A.3.1.1 Tests 1-4: Utility + DG Source + No PFC Taking time series voltage and current samples and solving for $z1(t)$ using equation A.1 the data shown in figures 75 (upstream fault) and 77 (downstream fault) are created. These figures show that this calculated pseudo-impedance

(shown as $Z1$ in the plot) appears to be quite non-linear, even prior to any fault being applied. In particular, every half-cycle, $z1(t)$ jumps to either a very high positive, or negative, value and then reverses polarity again.

In a system with only linear elements and no switching during fault-free operation, why is the output of equation A.1 non-linear? The answer comes from noticing that these regions of non-linearity occur near current peaks. Again referring to equation A.1 it is clear that at these points, the denominator begins approaching zero. The denominator approaches zero when the two sample values $i(t)$ and $i(t-1)$ are approximately equal. Mathematically this occurs when the first derivative of the sampled current waveform at that particular time value T $\left(\text{i.e., } \frac{di(t)}{dt}_{t=T}\right)$ approaches 0. Furthermore, since the graphical representation of this signal approaches infinity, once the current signal begins changing direction, the denominator changes sign within one sample period. This results in the dramatic swing in the $z1(t)$ from either positive to negative "infinity" and vice versa. Since this event occurs at each maxima or minima of the fundamental frequency of the waveform, the output from equation A.1 would be expected to be undefined at these points, and thus explaining the non-linearity. Would non-linearity increase uncertainty and therefore reduce the accuracy of these calculations? The simulation shows otherwise.

Begin by noting that the discussion of maxima or minima has assumed a fundamental waveform only with no noise or harmonics. As the sign of the difference equation of the current changes due to sub-cycle noise or harmonics, how would this affect the calculation of $z1(t)$? The discussion begins with simulations, but an actual "noisy" real-world fault direction test was also included.

Beginning with the simulations showing how this method is able to accurately predict the direction of a fault, an LTSPICE simulation was built that included two switching operations:

- $t = 0.2$ seconds switch S1 closes and produces a fault upstream of the measuring point (fault closer to the 30 kA, 480V "utility" source).

- $t = 0.3$ seconds switch S2 closes and applies a fault downstream of the measuring point (fault closer to the 90A, 480V "DG" source)

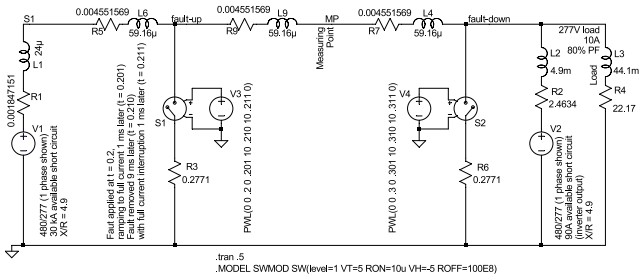

Figure 74: LTSPICE simulation of fault upstream from measured current. Point marked “MP” is the metering point

In both cases, the fault was allowed to persist for 10 ms. To more accurately model an arcing contact, the fault current ramped linearly from zero to maximum on initiation of a fault. When the fault was removed, the current ramped from maximum to zero. In both cases time period over which the current magnitude ramped was 1 ms

Referring to figure 74, switch S1 places a line-to-ground fault ahead of the metering point (MP) on this single phase model of a three-phase circuit. Switch S2 places the equivalent fault downstream of the metering point.

A.3.2 Measured Results

Waveforms were captured for both upstream and downstream faults. The visual difference in the calculated $z1(t)$ plot between the two tests was dramatic, clearly showing the ability to locate a fault using equation A.1.

A.3.2.1 Test 1: Upstream Fault Figure 75 shows the plot of $z1(t)$ collected for the upstream fault occurring during the time interval $t = 0.2$ to $t = 0.210$. As is clear from a visual inspection, the shape of the $z1(t)$ plot does not change, even during the transient event. Restating, since $z1(t)$ calculates the impedance downstream from the metering point and since the impedance downstream has not changed, this plot has not changed. This is a key indication that the fault is not downstream of the metering point.

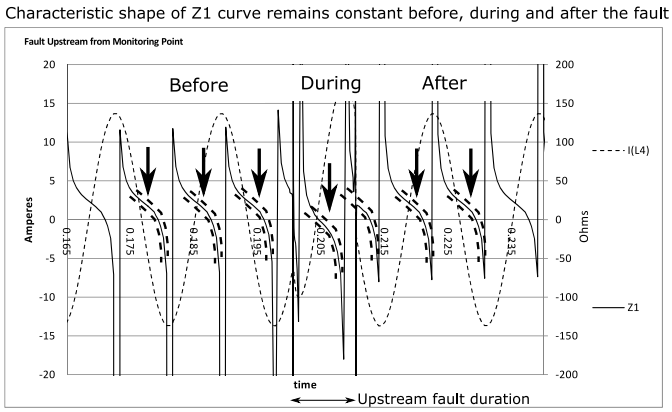

Figure 75: Test 1: Fault upstream of monitoring point, I(L4), with superimposed instantaneous impedance $z1(t) = v(t)/i(t)$

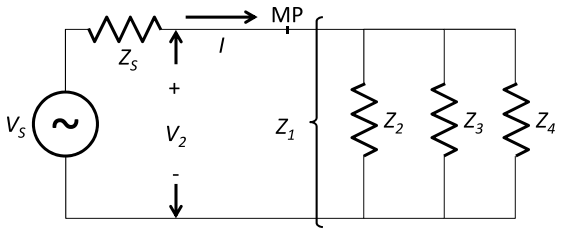

Figure 76: Simplified Figure 74 with alternative generation offline

Why would $z1(t)$ not be expected to change for an upstream fault? Referring to figure 76 (which is a redrawn and simplified figure 74) it is clear that the KCL equation needed to solve for the voltage V_2 is shown as equation A.2:

$$V_2 = I\left(\frac{1}{\frac{1}{Z_2}+\frac{1}{Z_3}+\frac{1}{Z_4}}\right) \tag{A.2}$$

Rewriting,

$$\frac{V_2}{I} = Z_1 = \frac{1}{\frac{1}{Z_2}+\frac{1}{Z_3}+\frac{1}{Z_4}} \tag{A.3}$$

The signals V_S and Z_S are recognized to not be used to calculate Z_1 (and therefore Z_1). Z_1 is derived only as the ratio of V_2/I. By inspection, equation A.3 shows that this calculation, in the steady state, can only be affected by downstream impedances Z_2, Z_3, and Z_4. This means that $z1(t)$ only measures the equivalent impedance from the metering point (MP) *towards the load* ignoring any changes in Z_S or V_S. While it may not be clear that equation A.3 is not shown as a difference equation, recall that the pseudo-impedance equation A.1 is and what is recognized, therefore, that if there were stored energy elements downstream of the metering point MP, then momentary changes to the upstream voltage could cause the transient effects shown in figure 75. However, as is also clear from examination of figure 75, these transients do not prevent the determination of the direction to the fault.

A.3.2.2 Test 2: Downstream Fault The next test was performed by placing a fault downstream from the metering point (shown as MP on the schematic in figure 74).

Unlike the plot shown in figure 75, examination of figure 77 immediately shows an obvious change in the shape of the $z1(t)$ curve during the fault window ($t = 0.3$ to $t = 0.31$).

A.3.2.3 Test 3: Upstream Fault - Low Power Factor Load - Larger DG Source Would changing the magnitude of stored energy in the load or creating a larger downstream source affect the shape of the z1(t) plot? To answer that question a simulation was run with a load power factor set to 20% (X/R=4.9) and the DG source available short circuit raised to 30 kA . Test 1 was then

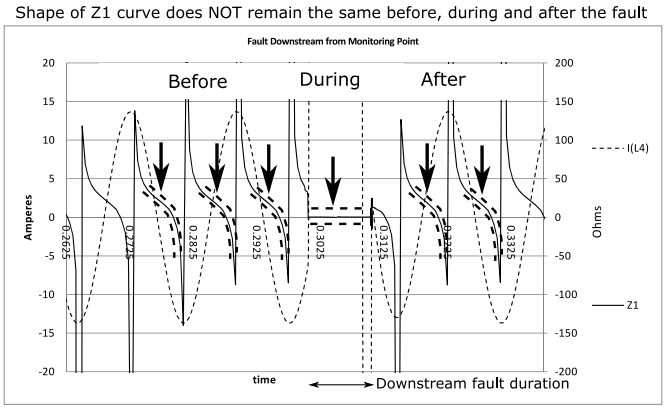

Figure 77: Test 2: Fault downstream of monitoring point

repeated with these higher stored energy sources downstream from the fault. The schematic for this test is shown in figure 78 and the plotted results in figure 79.

Figure 79 shows that as with figure 75 the characteristic shape of $z1(t)$ curve does not change during the period of time that the fault persists on the bus.

A.3.2.4 Test 4: Downstream Fault - Low Power Factor Load Similar to the difference between Test 1 and Test 3, Test 2 (downstream fault) is repeated, now as Test 4, with the only difference being the same lower load power factor and larger DG source that was used in Test 3. Also, like Test 2 (figure 77), Test 4 (figure 80) shows a change in $z1(t)$ that very clearly shows the

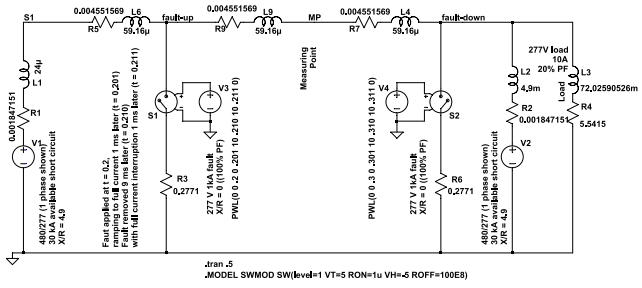

Figure 78: LTSPICE simulation (Tests 3 and 4): 30 kAIC utility and DER sources. 20% load PF

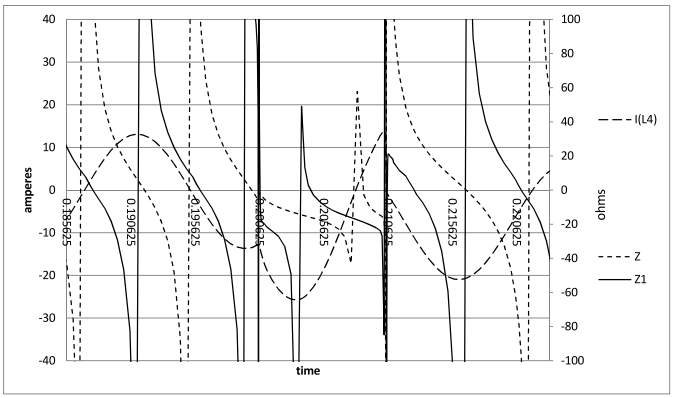

Figure 79: Test 3: 30 kA utility and 30 kA DER. 10A, 20% PF load. Upstream fault

characteristic drop in magnitude of $z1(t)$ indicating the presence of a downstream fault. The conclusion that can be made is that neither load power factor or the size of DG affect the determination of fault direction to any appreciable amount using the $z1(t)$ algorithm (equation A.1).

A.3.2.5 Test 5: With Intermittent Generation Offline Earlier, a theoretical explanation was given why intermittent distributed generation can complicate both directional and impedance fault locating methods. To examine how the switched presence or absence of DG/DER on the system could potentially affect this new method, additional simulations were run with the distributed generation source offline.

In figure 81 the distributed generator V_2 has been removed from the circuit (by setting series resistance $R_2 = 1$ GΩ). Repeating the test simulations shows similar results to earlier tests.

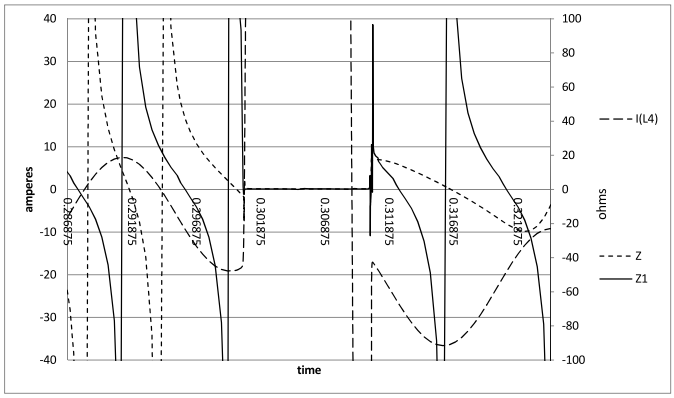

Figure 80: Test 4: 30 kA utility and 30 kA DER. 10A, 20% PF load. Downstream fault

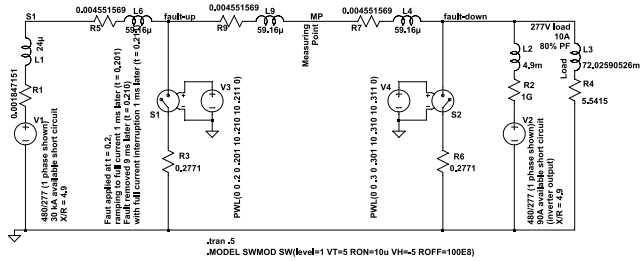

Figure 81: Tests 5 and 6: Distributed generation offline, 10A load. 20% power factor (X/R = 4.9)

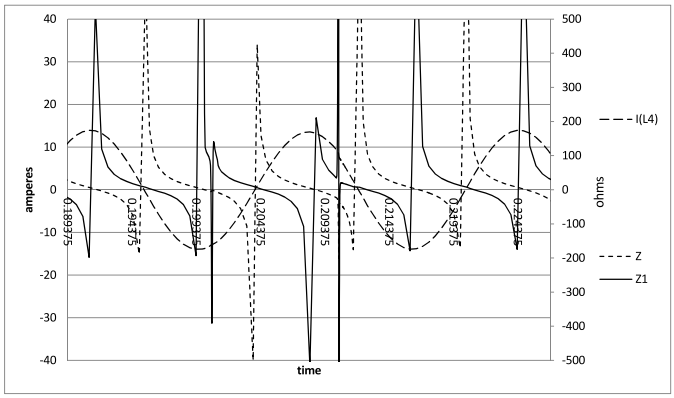

Figure 82: Test 5, upstream fault, no DG connected (based on schematic shown in figure 81)

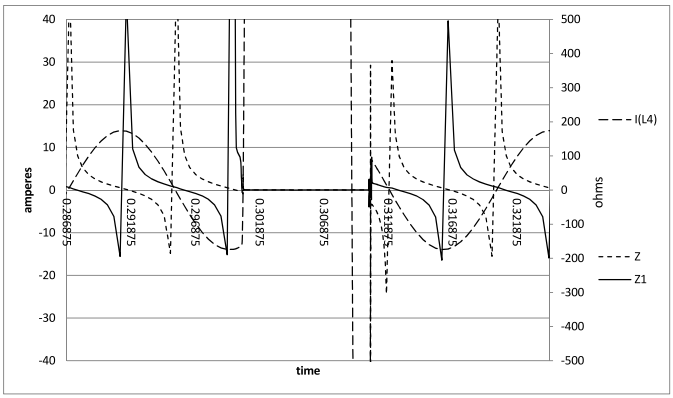

Figure 83: Test 6, downstream fault, no DG connected (based on schematic shown in figure 81)

Examination of figures 82 shows the same clearly identifiable patterns of no change in the shape of the $z1(t)$ plot for the upstream fault, whereas figure 83 shows the same dramatic change representative of a downstream fault earlier characterized in tests 2 and 4.

A.3.3 Power Factor Correction

Since this method for resolving fault location relies on examination of the slope (first derivative) of this calculated pseudo-impedance over time (which to the eye creates a particular "shape"), factors that distort this slope must be considered and analyzed. One factor is resonance. While capacitors sized for kvar correction typically do not induce resonance at fundamental power frequencies (otherwise they would self-excite), they frequently do excite resonance at harmonic frequencies. In micro-grid systems with variable sources, the parallel inductive reactance changes over time, changing the system resonance frequency. This is important since faults inject non-linear currents and the Fourier decomposition of both unit step (due to mechanical or electronic switching) or an arc, naturally produces excitation frequencies that may approach the system resonance frequency. Once a resonance near one of these frequencies is excited, oscillations between the system inductance and the power factor correction capacitors occur causing a change to the instantaneous slope of the measured current. This results in the same frequency oscillations being superimposed on the calculated pseudo-impedance $z1(t)$. Recalling our goal to develop an algorithm that detects fault

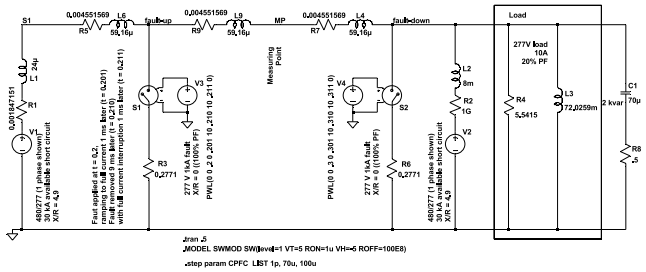

Figure 84: Tests 7 and 8: Distributed generation offline, 10A load. 20% power factor (X/R = 4.9) with 2 kvar power factor correction capacitor

location while minimizing the processing required, the question must be asked "what minimum level of filtering (if any) must be applied to deal with these oscillations?"

To test this problem, the simulation was modified to include a power factor correction capacitor in parallel to the load.

While the capacitor does introduce substantial oscillations at each point of the transition (fault applied, fault removed), the resultant information within the $z1(t)$ signal remains sufficiently visible to clearly identify the location of the fault.

A.3.4 Real world event

On 14-Nov-2014 a digital event recorder tracking energy feeding into the office where one of the authors' works (Loucks) captured a transient event. When the COMTRADE waveform file was decoded, it appeared as figure 87. While this this capture included much more "noise" due to the complicated switching pattern of loads within this large facility (260 000 ft^2 / 24 150 m^2), at the moment of the disturbance in the B-phase current plot, the $z1(t)$ plot shows a clear drop in impedance, remaining low for the duration of the event. This lends proof to our assertion that this algorithm is a simple, though accurate, method that is able to show that the disturbance was caused by a downstream event.

Figure 88 shows the average $z1(t)$ before and after the event, clearly showing the reduction in magnitude after the event, thus indicating a downstream event.

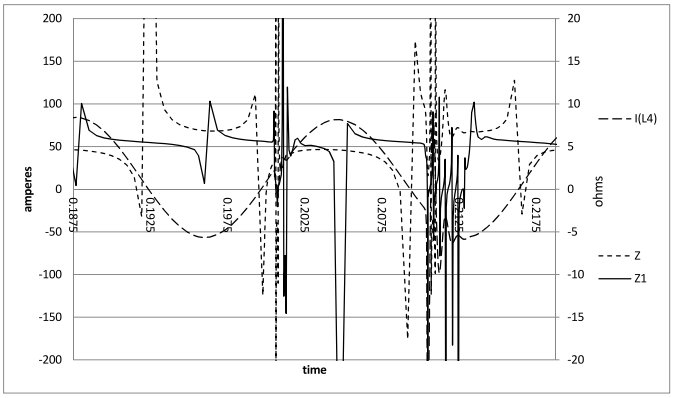

Figure 85: Test 7: 30 kA utility, 10A load at 20% PF load with 2 kvar capacitor added . Upstream fault

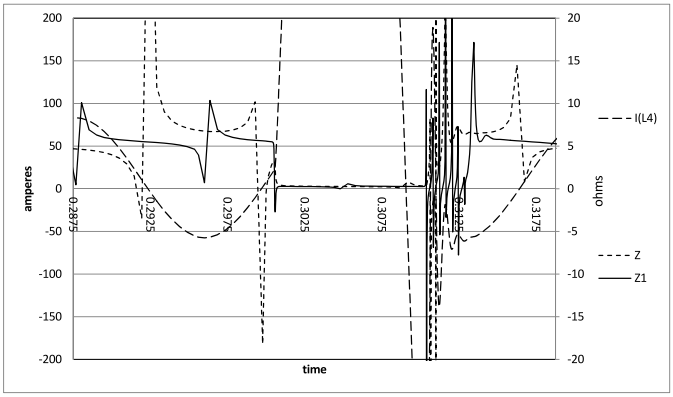

Figure 86: Test 7: 30 kA utility, 10A load at 20% PF load with 2 kvar capacitor added . Downstream fault

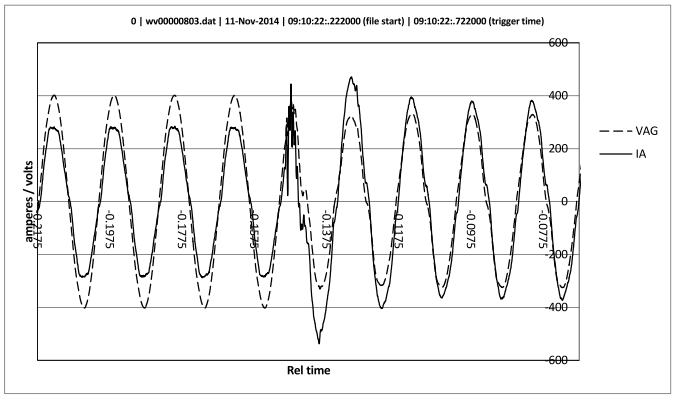

Figure 87: Voltage and Current waveforms of transient event captured at the service entrance of the author's facility

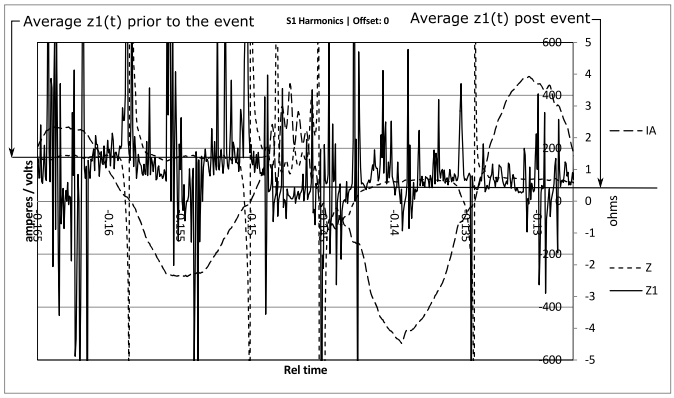

Figure 88: $z1(t)$ calculated for event shown in figure 87

A.4 ANALYTIC PROCESSING METHODOLOGY

To process this waveform, the algorithm must be fast – ideally detecting the change in impedance within a fraction of a cycle – while at the same time must be insensitive to the non-linear events characteristic of this pseudo-impedance calculation. Since fixed low-pass filters introduce delay (added zeros in FIR filters or poles and zeros in IIR filters adds additional delay elements z^{-1}, not to mention with IIR filters additional stages can reduce stability), a faster, more reliable filter is desired. The method proposed here is to use a 2-stage, switchable mode LP filter. The first stage is used to compute the long term average, while the second, faster filter monitors deviations to this average. One representation proposed to provide fast detection is for both filters to operate as "mode" LP filters, but each with different "gains" (see figure 89). Also, for the second, faster filter it will be important to differentiate between signal level changes due to faults and due to non-linear events. Referring again to figure 89, one solution proposed is to pass the input through a limiter – remapping any input signal greater than a chosen multiple M (greater than $|M * x_2(t)|$) of this previously computed average to be this computed average value.

In the first of the two stages, operation occurs at a lower value of gain G_n (where gain acts similarly to a Kalman gain [39]) until a predetermined number of samples k_{max} has been reached or when the standard deviation of the computed signal drops to an acceptable (for the user) minimum. At this point the loop stores the final steady-state value as x_1. The smaller values of G (shown as G_n, where $n = 2$) produces a computed value x_2 that approaches the mean of the sampled values. The mode algorithm is chosen to approximate the mean due to the non-linear aspects of the $z(t)$ input. Very large spikes approaching measurement limits (metering displayed as $\pm\infty$) skew an average but would not affect a mode (most common value) calculation in the same manner.

So, with a higher gain, the second stage mode filter responds more rapidly to changes in calculated pseudo-impedance but still ignores non-linear transient events.

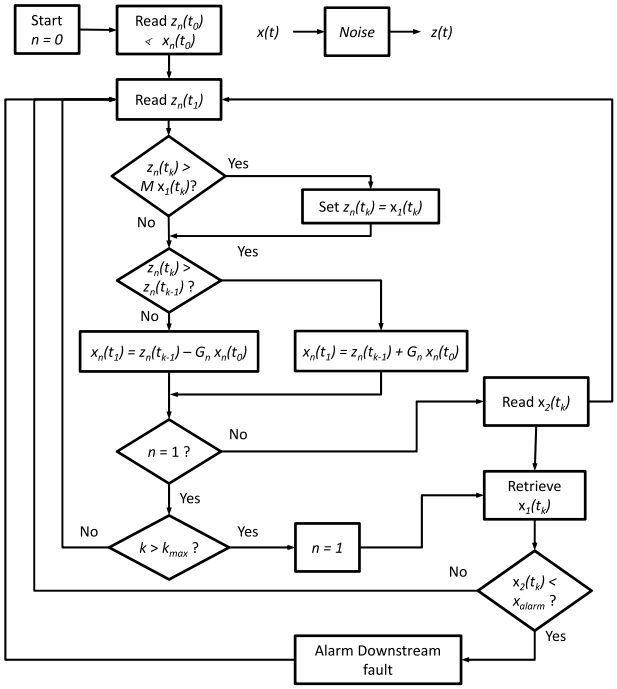

Figure 89: Simplified mode filter algorithm. Actual state (process variable $x(t)$) is corrupted by zero mean, uncorrelated noise.

A.5 CONCLUSION

While commonly used in distributed generation systems, directional current or distance relaying methods are made more complicated when the distributed energy resources are switched on or off or when they output different amounts of power. In particular, without a downstream source able to back-feed energy into an upstream fault, there is no reversal of current with which to trigger a reverse current relay. This renders directional current relay sensing methods less useful in those applications. Likewise, the well-known problem of injected current downstream from a distance relay causing errors in the calculation of the fault location must be addressed. While there are many methods that can overcome both of these limitations, many of these require advanced computation capability that may not be available on DG or micro-grid scale systems. Therefore, a different method of isolating faults is desirable. Such a method would ideally be simple to implement, even on hardware with limited compute resources (which is a typical restriction in cost constrained alternative energy controllers). To address that problem, this article demonstrated a reliable method of detecting fault direction that does not rely on current direction. This reduces the cost to implement, helping to insure wider acceptance. With wider acceptance the potential exists to meter a micro-grid with finer granularity. This can decrease the time to locate a fault, allowing the faster restoration of power to the remaining unfaulted sections and ultimately reducing outages to the minimum number of loads.

APPENDIX B

IEEE COMTRADE DECODING

B.1 INTRODUCTION

This IEEE standard, first introduced in 1992 [74] and, as of the date of this publication updated to a 2013 revision, defines a common format for the data files and exchange medium needed the interchange of various types of fault, test, and simulation data. IEEE believed, at that time, that since each source of data may use a different proprietary format, a common data format was necessary to facilitate the exchange of such data between applications.

To produce the data used in this research data was collected from IEDs and analyzed. To assist in this effort, a program was written that imported each waveform (stored in the IEEE COMTRADE file format) and allowed advanced analytics, processing and graphing. More information on this program can found at [58](including links to download a free copy and other links to video tutorials on how to use the program).

B.2 FILE TYPES

As background, there are two important file types used with the IEEE COMTRADE standard [6].

- .cfg (configuration file)
- .dat (data file)

Additionally, an optional file type, .hdr, is sometimes used for storing descriptions of the event type, captured parameters and other information beside trended waveform data.

B.2.1 File Format: *.cfg

The .cfg file is a text file that is created in the following format for every waveform set captured. The primary role of the .cfg file is provide information necessary to interpret the data stored in the .dat file. Since the .dat file only stores data in raw 16-bit binary values, reading only the .dat file will not provide information regarding scaling, nor will it provide information regarding the type of signal (V, I, etc.), or any time stamping.

A line-by-line explanation for the *.cfg files follows:

- Station_ID,Device_ID,1999<CR/LF> [Line 1 in PX version of this file]
- Total_Number_of_Channels,Number_of_Analog_Channels<A>, Number_of_Status_Channels<D> <CR/LF> [Line 2 in PX version of this file]
- Analog Channel Information:
- Channel_Number, Channel_Name,Phase_ID, Component_Name, Channel_Units, Multiplier, Offset, Skew_Microseconds, Minimum_Value, Maximum_Value, Primary_Ratio, Secondary_Ratio, Primary_or_Secondary<CR/LF> [Lines 3 through 14 in PX version of this file. Note: in the PX4/6/8K, the values for Minimum_Value and Maximum_Value are reversed]
- Repeat the above line for all analog channels.
- Status (Digital) Channel Information:
- Digital_Channel_Number, Digital_Channel_Name, Digital_Phase_ID,Digital_Channel_Source,Normal_Status <CR/LF> [Lines 15 through 21 in PX version of this file]
- Repeat the above line for all digital channels.
- Frequency<CR/LF> [Line 22 in PX version of this file]
- Number_of_Sample_Sets<CR/LF> [Line 23 in PX version of this file]
- Sampling_Rate,Number_of_Samples<CR/LF> [Line 24 in PX version of this file]
- Start_Time<CR/LF> [Line 25 in PX version of this file]
- Trigger_Time<CR/LF> [Line 26 in PX version of this file]

```
,One,1999
24,16A,8D
1,VBG,VB, ,V,0.036000,0,0,32767,-32767,120.000000,120.000000,S
2,VAG,VA, ,V,0.036000,0,0,32767,-32767,120.000000,120.000000,S
3,VNG,VN, ,V,0.036000,0,0,32767,-32767,120.000000,120.000000,S
4,VCG,VC, ,V,0.036000,0,0,32767,-32767,120.000000,120.000000,S
5,VAGAUX,VA2, ,V,0.036000,0,0,32767,-32767,120.000000,120.000000,S
6,VRG,VR, ,V,0.036000,0,0,32767,-32767,120.000000,120.000000,S
7,VCGAUX,VC2, ,V,0.036000,0,0,32767,-32767,120.000000,120.000000,S
8,VBGAUX,VB2, ,V,0.036000,0,0,32767,-32767,120.000000,120.000000,S
9,RESERVEDB,RSVDB, ,A,0.980000,0,0,32767,-32767,5000.000000,5.000000,S
10,RESERVEDC,RSVDC, ,A,0.980000,0,0,32767,-32767,5000.000000,5.000000,S
11,IG,IG, ,A,0.078400,0,0,32767,-32767,400.000000,5.000000,S
12,RESERVEDA,RSVDA, ,A,0.980000,0,0,32767,-32767,5000.000000,5.000000,S
13,IC,IC, ,A,0.078400,0,0,32767,-32767,400.000000,5.000000,S
14,IN,IN, ,A,0.078400,0,0,32767,-32767,400.000000,5.000000,S
15,IA,IA, ,A,0.078400,0,0,32767,-32767,400.000000,5.000000,S
16,IB,IB, ,A,0.078400,0,0,32767,-32767,400.000000,5.000000,S
1,DI1:Input One,??,DI1:Input One,0
2,DI2:Input Two,??,DI2:Input Two,0
3,DI3:Input Three,??,DI3:Input Three,0
4,DI4:Input Four,??,DI4:Input Four,0
5,DI5:Input Five,??,DI5:Input Five,0
6,DI6:Input Six,??,DI6:Input Six,0
7,DI7:Input Seven,??,DI7:Input Seven,0
8,DI8:Input Eight,??,DI8:Input Eight,0
59.988522
1
30720.000000,30720
19/05/2015,14:07:40.838000
19/05/2015,14:07:41.338000
BINARY
1
```

Figure 90: IEEE COMTRADE .cfg file. Data stored in comma-separated values (CSV) format

```
                Three           1999
20              12A             8D
1               VCGAUX          ??                      V  0.031250  0  0  32767  -32767  120.000000  120.000000  S
2               VAG             VA                      V  0.031250  0  0  32767  -32767  120.000000  120.000000  S
3               IA              IA                      A  0.582400  0  0  32767  -32767  1600.00000(5.000000     S
4               VBG             VB                      V  0.031250  0  0  32767  -32767  120.000000  120.000000  S
5               IB              IB                      A  0.582400  0  0  32767  -32767  1600.00000(5.000000     S
6               VCG             VC                      V  0.031250  0  0  32767  -32767  120.000000  120.000000  S
7               IC              IC                      A  0.582400  0  0  32767  -32767  1600.00000(5.000000     S
8               VNG             VN                      V  0.031250  0  0  32767  -32767  120.000000  120.000000  S
9               IN              IN                      A  0.436800  0  0  32767  -32767  1200.00000(5.000000     S
10              VAGAUX          ??                      V  0.031250  0  0  32767  -32767  120.000000  120.000000  S
11              IG              IG                      A  0.436800  0  0  32767  -32767  1200.00000(5.000000     S
12              VBGAUX          ??                      V  0.031250  0  0  32767  -32767  120.000000  120.000000  S
1               DI1:Input One   ??   DI1:Input One      0
2               DI2:Input Two   ??   DI2:Input Two      0
3               DI3:Input Three ??   DI3:Input Three    0
4               DI4:Input Four  ??   DI4:Input Four     0
5               DI5:Input Five  ??   DI5:Input Five     0
6               DI6:Input Six   ??   DI6:Input Six      0
7               DI7:Input Seven ??   DI7:Input Seven    0
8               DI8:Input Eight ??   DI8:Input Eight    0
60.000000
1
15360.000000    15360
11/11/2014      09:10:22.222000
11/11/2014      09:10:22.722000
BINARY
1
```

Figure 91: Same .cfg file as shown in figure 90, but decoded to show column spacing

- Data_Type<CR/LF> [Line 27 in PX version of this file]
- Time_Multiplier<CR/LF> [Line 28 in PX version of this file]

See PXM version of an example COMTRADE file immediately below.

B.2.2 File Format: *.dat

Data file contains captured waveform data from all channels. A new data file with the following format is created for every waveform captured. Unlike the .cfg where where information was saved in ASCII characters, the numbers stored in the *.dat file are stored as binary numbers.

- All binary values are stored with least significant byte (LSB) first and most significant byte last.
- <Sample_Number> <Timestamp> <A1> <A2> ..... <Ak> <D1> <D2> ..... <Dm> < Sample_Number>.....

COMTRADE .CFG File Decode

30720

Station ID	Device ID	
Three	1999	
Total	**Analog**	**Digital**
20	12A	8D

Analog Channels

Ch. Num	Ch. Name	Phase ID	Comp Name	Ch. Units	Multiplier	Offset	Skew	Min Value	Max Value	Pri Ratio	Sec Ratio	Pri or Sec
1	VCGAUX	??		V	0.03125	0	0	32767	-32767	120	120	S
2	VAG	VA		V	0.03125	0	0	32767	-32767	120	120	S
3	IA	IA		A	0.5824	0	0	32767	-32767	1600	5	S
4	VBG	VB		V	0.03125	0	0	32767	-32767	120	120	S
5	IB	IB		A	0.5824	0	0	32767	-32767	1600	5	S
6	VCG	VC		V	0.03125	0	0	32767	-32767	120	120	S
7	IC	IC		A	0.5824	0	0	32767	-32767	1600	5	S
8	VNG	VN		V	0.03125	0	0	32767	-32767	120	120	S
9	IN	IN		A	0.4368	0	0	32767	-32767	1200	5	S
10	VAGAUX	??		V	0.03125	0	0	32767	-32767	120	120	S
11	IG	IG		A	0.4368	0	0	32767	-32767	1200	5	S
12	VBGAUX	??		V	0.03125	0	0	32767	-32767	120	120	S

Ch. Num	Ch. Name	Phase ID	Ch. Source	Norm. Status
1	DI1:Input One	??	DI1:Input One	0
2	DI2:Input Two	??	DI2:Input Two	0
3	DI3:Input Three	??	DI3:Input Three	0
4	DI4:Input Four	??	DI4:Input Four	0
5	DI5:Input Five	??	DI5:Input Five	0
6	DI6:Input Six	??	DI6:Input Six	0
7	DI7:Input Seven	??	DI7:Input Seven	0
8	DI8:Input Eight	??	DI8:Input Eight	0

			Month	Day	Year	Date	Hr	Min	Sec	uSec	Time
Frequency	60										
# samp. sets	1	**Start Time:**	11	11	2014	11/11/2014	9	10	22	222000	9:10:22.222
samp. Rate	15360	**Trigger Time:**	11	11	2014	11/11/2014	9	10	22	722000	9:10:22.722
# samples	15360										
data type	BINARY	sample period	1 sec								9:10:22.489
time mult.	1	ms / sample	0.06510 ms								
		µs / sample	65.10417 µs								
		samples/cycle	256								

Figure 92: Same .cfg file as shown in figures 90 and 91, but further decoded to show meaning of each entry

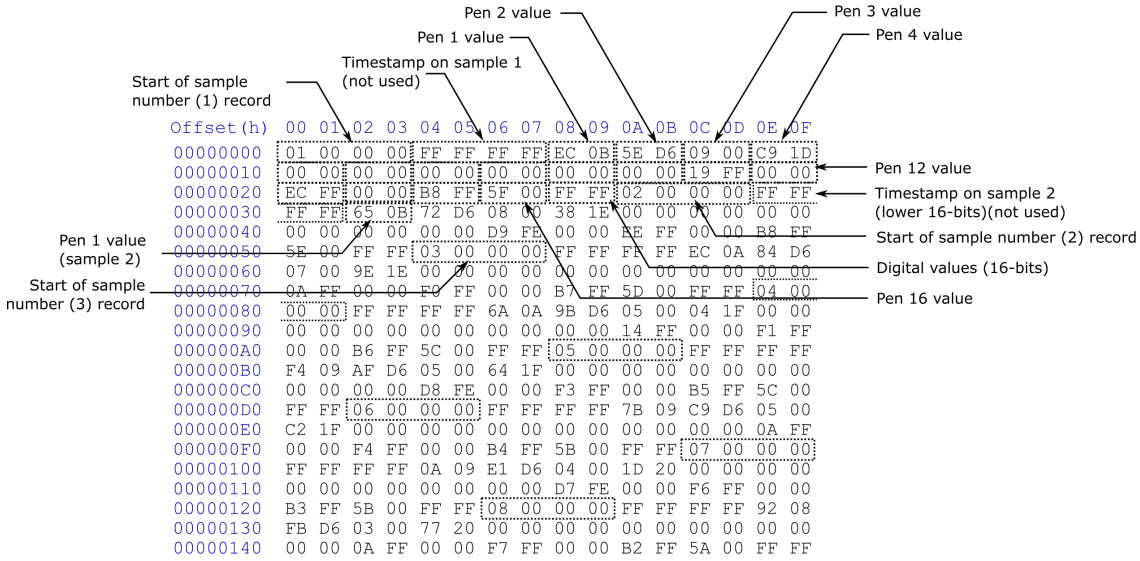

Figure 93: IEEE COMTRADE .dat file decoding

- Referring to line 2 in the example *.CFG shown above, the values on that line of "20, 12A, 8D", are translated to mean a total of 20 channels, 12 analog and 8 digital are present in the *.dat file. In the PXM, sets of digital channels are 16-bits, although current implementations of the PXIO card only support 8 inputs. However, the *.dat file reserves 16 bits (2 bytes) for digital data.

- Referring to lines 3 - 14, the range of the value stored in those first 12 analog values is -32768 $\leq$ x $\leq$ 32367 which is a range of 16 bits

- Therefore, in the current version of Eaton Power Xpert meters, each of the separate time stamped entries in the COMTRADE file requires 34 bytes as shown here:

4 byte sample number +

4 byte time (always FFFF) +

24 bytes (2 bytes/value x 12 values) 16-bit (2 byte) signed integer values[1] +

2 bytes for digital (16 bits are reserved even though only the first 8 are used in current versions of the PXIO card)

= 34 bytes

- Note that in the Eaton implementation of the COMTRADE *.dat file, a time value is not supplied for each sample. However, since lines 25 defines the start time and line 24 defines the sample rate in samples per second, the time of each sample can be calculated.

Some of the waveforms displayed in this document were captured in the IEEE COMTRADE file format. An Excel program was developed in VBA ([63]). The entire program can be downloaded from [58]. By writing this program the task of creating publication quality images was simplified by allowing the export of the COMTRADE file converted into an Excel plot into a scalable vector file format (PDF). This PDF file was then imported into Inkscape™[29], converted to an encapsulated Postscript file and then imported into LyX by inserting a Graphics... image into a Float Figure box.

While the program itself has thousands of lines of code, the two main routines for parsing the .cfg and .dat files are highlighted in the code samples below:

B.3 EXAMPLE CODE

B.3.1 readCFGCSV:

The function readCFGSV opens the .cfg file, decodes the COMTRADE values and stores them in an Excel spreadsheet "CFG-Decode". The data stored in CFG-Decode is then accessed by the "open_dat" routine. The .cfg file decodes:

- Total number of channels (pens) recorded in the associated .dat event file
- Number of the total channels that are analog

[1] ($-32768 \leq x \leq 32367$)

- Number of the total channels that are digital
- Names of each of the analog and digital channels (Vab, Ia, etc.)
- Units names for each channel (V, A, kV, etc.)
- Scaling multiplier by channel/pen (16-bit binary value stored in .dat file is multiplied by this value before being written to the spreadsheet)
- Time offset or time skew per channel in microseconds
- Minimum and maximum binary values stored for each channel/pen
- Primary and secondary turns ratios
- Nominal frequency of power system
- Number of distinct sample sets
- Sample rate (samples/sec)
- Number of samples
- Data type (this version of the program only works with binary .dat files)
- Time multipliers
- Trigger start time
- Sample period (duration of the waveform capture)
- ms and μs per sample
- Samples per cycle

```
Function readCFGCSV(gstrFilename As String, sFilePath As String) As Boolean
    Dim FileContents As String, vFF As Long, vFile As String
    Dim vRecords() As String, vTempArr() As Variant, vFileRecords() As String
    Dim RecordCount As Long, FieldCount As Long, i As Long, j As Long

    Dim intFileNum, intTemp As Integer, intCellRow As Long, intCellCol As Integer, NumCols As
        Integer
    Dim intHiTemp, sTemp1, sTemp2 As Integer
    Dim lFilePointer As Long
    Dim data As Long
    Dim FileName As String, fileNamePath As String
    Dim objsheet, multArray() As String, resolutionArray() As String
    Dim lWord As Long, nameArray() As String
    Dim fileReader, temp1, sFileNoExten As String, sExten As String, temp2 As String, value As
        Integer
    Dim ckBoxes() As Object
    Dim bValidExtension As Boolean

    bValidExtension = False      'preset

    If (UCase(Right(gstrFilename, 3)) = "CFG") Then
        'proper file extension
        bValidExtension = True
        Update ("User␣entered␣.cfg␣as␣COMTRADE␣filename.␣␣Accepted")
    Else
        If (UCase(Right(gstrFilename, 3)) = "DAT") Then
```

```
        'proper file extension
        bValidExtension = True
        Update ("User␣entered␣.dat␣as␣COMTRADE␣filename.␣␣Accepted")
        Else
            If (UCase(Right(gstrFilename, 3)) = "HDR") Then
                'proper file extension
                bValidExtension = True
                Update ("User␣entered␣.hdr␣as␣COMTRADE␣filename.␣␣Accepted")
            Else
                Update ("User␣entered␣COMTRADE␣filename␣with␣unrecognizable␣extension.␣␣COMTRADE␣
                    file␣not␣parsed.")
            End If
        End If
    End If

    'if not valid extension, no need to open the file
    If (bValidExtension) Then
        'check to see if we have .cfg, .dat, .hdr or no extension
        sTemp1 = Len(gstrFilename)    'find length of filename
        sTemp2 = InStrRev(gstrFilename, ".") 'position of .
        sExten = Mid(gstrFilename, sTemp2 + 1, sTemp1 - sTemp2)
        gsFileNoExten = Mid(gstrFilename, 1, sTemp2 - 1) 'filename without the extension
        fileNamePath = sFilePath + gsFileNoExten + ".cfg"
        'fileNamePath = gsFileNoExten + ".cfg"
        'fileNamePath = gsFileNoExten + ".cfg"

        formStatus.Show
        displayStatusForm "Attempting␣to␣open␣" + fileNamePath + "␣to␣read␣.cfg␣configuration␣
            file"
        Update "Attempting␣to␣open␣" + fileNamePath + "␣to␣read␣COMTRADE␣.cfg␣configuration␣file"

        Set objsheet = ActiveWorkbook.Worksheets("CFG-raw") 'point back to CFG sheet
        Worksheets("CFG-raw").UsedRange.Clear
        'clear out the decoded CFG file data from the variable length tables
        Worksheets("CFG-Decode").Range("A9:M24") = ""
        Worksheets("CFG-Decode").Range("A28:E35") = ""
        Worksheets("CFG-Decode").Range("B45:B50") = ""
        Worksheets("CFG-Decode").Range("E46:G47") = ""
        Worksheets("CFG-Decode").Range("I46:L47") = ""

        If FileThere(fileNamePath) Then
            'pull entire text file into FileContents variable
            vFile = fileNamePath
            vFF = FreeFile
            Open vFile For Binary Access Read As #vFF
            FileContents = Space$(LOF(vFF))
            Get #vFF, , FileContents
            Close #vFF

             'split by record-delimiter
            vRecords = Split(FileContents, vbCrLf)

             'Create overall array to store entire text file's fields and records
             ' Note that this step is not necessary, just speeds up overall processing time

             'Split each record by field delimiter
            RecordCount = UBound(vRecords)
            ReDim vTempArr(RecordCount)
            For i = 0 To RecordCount
                vTempArr(i) = Split(vRecords(i), ",")
            Next

             'determine max number of fields
            FieldCount = 0
            For i = 0 To RecordCount
                If UBound(vTempArr(i)) > FieldCount Then FieldCount = UBound(vTempArr(i))
            Next
```

```
            'create 2 dimensional array to store all data
            ReDim vFileRecords(RecordCount, FieldCount)
            For i = 0 To RecordCount
                For j = 0 To UBound(vTempArr(i))
                    vFileRecords(i, j) = vTempArr(i)(j)
                Next
            Next

            'Transfer array data onto spreadsheet
            'Workbooks.Add
            Set objsheet = ActiveWorkbook.Worksheets("CFG-raw")

            With objsheet.Cells(1, 1).Resize(RecordCount + 1, FieldCount + 1)
                .NumberFormat = "@" 'make text format
                .value = vFileRecords
            End With

            displayStatusForm gsFileNoExten + ".cfg" + " read and parsed"
            readCFGCSV = True

            'validate if CFG file is formatted correctly
            bCFGIssueFound = False  'clear flag to initialize
            If ValidateCFG Then
                'CFG file has problems!
                Update ("Total number of channels found in .cfg file does not match sum of analog
                    + digital channels")
                bCFGIssueFound = True   'set flag
            Else
            'CFG file appears valid (although not every entry checked, so could still blow up...)
                MoveCFGdata 'transfer data from CFG-raw to CFG-Decode worksheet
                FoundLineGroundVoltage  'look for Vag, Vbg and Vcg to determine if able to
                    calculate Vab, Vbc and Vca
            End If

            bCompleteCFGParse = True    'finished parsing

        Else
            Update ("COMTRADE configuration (*.cfg) file not found (" & fileNamePath & ")")
            readCFGCSV = False
        End If
    Else
        'invalid file extension
        Update ("Invalid file name: " & gstrFilename)
        readCFGCSV = False
        bCFGIssueFound = True

    End If

    hideStatusForm  'remove status form

End Function
```

B.3.2 open_dat:

The function open_dat opens the binary .dat file containing the waveform time series data and writes it to the spreadsheet in the "COMTRADE Data" worksheet. To work properly, open_dat calls the function readCFGCSV to open the .cfg file associated with this event (will have the same file name as the .dat file, just with a .cfg extension) prior to opening the .dat file. The data stored

in the .cfg file will instruct open_dat how to properly decode, scale and time stamp the binary waveform data. If the .cfg file is corrupted, the open_dat routine terminates with an error.

```
Sub open_dat(gstrFilename As String, sFilePath As String)
    'Read COMTRADE data and write each new time to new row, each new value to column

    'Input:
    'gstrFilename    = filename of COMTRADE file to open and process
    'sFilePath       = path to COMTRADE file

    'Note:
    'COMTRADE data is stored in a minimum of two files
    '.dat   - binary waveform data stored as an 16-bit value
    '.cfg   - text file that provides scaling, range, name, etc. for each variable captured

    'This subroutine also calls a routine that opens the .cfg file and reads this information
    'and places the coded data into the "CFG-Decode" spreadsheet tab. open_dat uses this to
    'determine how to scale the raw binary data from the .dat file prior to placing it in
    'the COMTRADE Data spreadsheet tab

    'Output:
    'Each entry placed in "COMTRADE Data" tab of spreadsheet

    Dim intFileNum, intTemp As Integer, intCellRow As Long, intCellCol As Integer, NumCols As
        Integer
    Dim intHiTemp As Integer
    Dim lFilePointer As Long
    Dim data As Long
    Dim FileName As String, fileNamePath As String
    Dim objsheet, multArray() As String, resolutionArray() As String
    Dim lWord As Long, nameArray() As String, i As Integer, name
    Dim temp1 As String, temp2 As String, value As Integer
    Dim ckBoxes() As Object
    Dim iNumAnalogs As Integer, iNumDigitals As Integer
    Dim iSampleRate As Long
    Dim dabs_time As Double
    Dim ldeltaTime As Double
    Dim lsampleNumber As Long
    Dim istartCol As Integer
    Dim lendRow As Long
    Dim start_time As Double
    Dim abs_time As Double
    Dim bValid As Boolean
    Dim asCD(65536, 36) As Variant
    Dim iMaxCol As Integer

    'Determine at what row and column the first data should be written
    intCellRow = 3  'starting row where to place data (3- skip paste top title lines)
    intCellCol = 1  'starting column (1=leftmost)

    lWord = 0
    intFileNum = FreeFile
    bDATIssueFound = False  'initialize error flag (if problems this is set true)

    'Read the .cfg file to see how many columns will be in our COMTRADE output (1 col per
        variable trended)
    bValid = readCFGCSV(gstrFilename, sFilePath)

    If (bValid) Then
        'If the data found in the .cfg file looks valid, proceed

        'Point to the .dat and open that filename
        formStatus.Show 'display a status message alert box

        'Write a message to the alert box
        displayStatusForm "Opening " & gsFileNoExten & ".data" & " from " & " to read contents"
```

```
'Write a message to the log
Update "Opening " + gsFileNoExten & ".dat" & " from " + " to read contents"

'Clear out the COMTRADE Data spreadsheet.  We do this in case the .dat file we open is
'corrupted. We don't want to carry any left-over values from the previous calculation
Worksheets("COMTRADE Data").UsedRange.Clear

'Look up sample rate (samples/second) from the decoded .cfg file data
'(now stored in the CFG-Decode sheet
iSampleRate = Worksheets("CFG-Decode").Cells(47, 2).value

'Look up waveform capture start time
start_time = Worksheets("CFG-Decode").Cells(46, 13).value

'Read the file name and IP address and add to graph title
'Note: we discovered with VBA that it is a faster operation to write all data to an
'array, and then write the array to the sheet rather than writing each new value to the
'spreadsheet.  Therefore, in the next line where we are reading the file name and writing
'this to the sheet, we first just write it to a 2-dimensional array variable.  The
'first dimension is the offset from the first row and the second is the offset from the
'first column
asCD(0, 0) = gsFileNoExten & ".dat"    'tell us which filename we are displaying
asCD(0, 3) = frmFTPParams.sIPAddress.value

'Note: present version limits up to 16 analog and 16 digital channels (PX meters today
    have 12 analog + 8 dig)
'These global variables were updated when the .cfg file was decoded
If giNumAnalog > 16 Then giNumAnalog = 16
If giNumDigital > 16 Then giNumDigital = 16

i = 1    'starting column where to place titles on COMTRADE Data worksheet

'Place the "Sample" and "Time" columns (note PX 4/6/8K stores -1 in the time column
'meaning that column isn't used by the 4/6/8K at the time this code was written)
asCD(1, 0) = "Sample"
asCD(1, 1) = "Time"

'Now read the analog names from the .cfg file and write the the COMTRADE Data worksheet
'These names are written across the top columns of on the COMTRADE Data sheet
For i = 1 To giNumAnalog
    asCD(1, 1 + i) = Worksheets("CFG-Decode").Cells(8 + i, 2).value
Next

'Now read the digital names from the .cfg file and do the same thing
For i = 1 To giNumDigital
    asCD(1, i + giNumAnalog + 1) = Worksheets("CFG-Decode").Cells(27 + i, 2).value
Next

'Now add two columns for absolute time and relative time
'relative time: absolute time - trigger time
asCD(1, giNumAnalog + giNumDigital + 2) = "Abs time"
asCD(1, giNumAnalog + giNumDigital + 3) = "Rel time"

If gbFoundLineGroundVoltage Then
    asCD(1, giNumAnalog + giNumDigital + 4) = "Vab"
    asCD(1, giNumAnalog + giNumDigital + 5) = "Vbc"
    asCD(1, giNumAnalog + giNumDigital + 6) = "Vca"
    'Load warning about vendor specific columns
    'The 4/6/8K meters don't save line-to-line voltages so these are calculated from
    'line-to-neutral voltages
    asCD(0, giNumAnalog + giNumDigital + 4) = "NOTE: Vab, Vbc & Vca were calculated from
        columns named Vag, Vbg and Vcg"

    'since we have line to ground voltages, we can calculate Z per phase by dividing by I
         per phase
    asCD(1, giNumAnalog + giNumDigital + 7) = "Za"
    asCD(1, giNumAnalog + giNumDigital + 8) = "Zb"
```

```
    asCD(1, giNumAnalog + giNumDigital + 9) = "Zc"
    asCD(1, giNumAnalog + giNumDigital + 10) = "delta Za"
    asCD(1, giNumAnalog + giNumDigital + 11) = "delta Zb"
    asCD(1, giNumAnalog + giNumDigital + 12) = "delta Zc"
End If

lFilePointer = 0     'keeps track of file location
fileNamePath = sFilePath + gsFileNoExten & ".dat"
'-------------------------------------------------------------
'now we get to business and begin parsing the COMTRADE data and placing the results into
    COMTRADE Data worksheet
'-------------------------------------------------------------
Open fileNamePath For Binary Access Read As intFileNum
Do While Not EOF(intFileNum)
    'Each COMTRADE record starts with 4-byte sequence and 4-byte time
    'Start by processing the analog data
    If intCellCol < giNumAnalog + 3 Then
        Get intFileNum, , intTemp
        'Stay on same row, increment intCellCol
        'Data is stored as 2-byte, 2's complement integers
        If (intCellCol <= 2) Then
            'Store a 4-byte value in spreadsheet cell
            Get intFileNum, , intHiTemp
            temp1 = Hex$(intTemp)
            temp2 = Hex$(intHiTemp)
            data = Val("&h" + temp2 + temp1)
            asCD(intCellRow - 1, intCellCol - 1) = data
        Else
            'Store a 2-byte value in spreadsheet cell
            asCD(intCellRow - 1, intCellCol - 1) = intTemp * Worksheets("CFG-Decode").
                Cells(intCellCol + 6, 6).value
        End If
        intCellCol = intCellCol + 1
    Else
        'Reached end of analog columns - begin processing digital values
        If giNumDigital > 0 Then
            Get intFileNum, , intTemp    'fetch 2 bytes (16 bits ... the max supported
                right now)
        End If

        For i = 1 To giNumDigital
            'intTemp now has a 16-bit word.  Write 1's and/or 0's into appropriate
                columns of COMTRADE Data worksheet
            asCD(intCellRow - 1, intCellCol - 1) = (intTemp And (2 ^ (i - 1))) / (2 ^ (i
                - 1))
            intCellCol = intCellCol + 1
        Next

        'Add a column for the absolute time
        lsampleNumber = intCellRow - 2
        abs_time = start_time + (1 / iSampleRate) * lsampleNumber

        'Excel time where 1 = 1 day = 86400 seconds
        ldeltaTime = (1 / (iSampleRate)) * (lsampleNumber - 1)    'seconds past start of
            file
        ldeltaTime = ldeltaTime / 86400      'convert seconds into fractions of days
        dabs_time = Worksheets("CFG-Decode").Cells(46, 13) + ldeltaTime
        asCD(intCellRow - 1, intCellCol - 1) = dabs_time
        intCellCol = intCellCol + 1

        asCD(intCellRow - 1, intCellCol - 1) = (dabs_time - Worksheets("CFG-Decode").
            Cells(47, 13)) * 86400
        intCellCol = intCellCol + 1

        If gbFoundLineGroundVoltage Then
            'Write Vab (Vag - Vbg), Vbc (Vbg - Vcg), Vca (Vcg - Vag)
            '*** NOTE *** this will be PX specific code since other devices will have
                different values in different columns
```

```
        asCD(intCellRow - 1, intCellCol - 1) = asCD(intCellRow - 1, giVagCol - 1) -
            asCD(intCellRow - 1, giVbgCol - 1) 'Vab
        asCD(intCellRow - 1, intCellCol) = asCD(intCellRow - 1, giVbgCol - 1) - asCD(
            intCellRow - 1, giVcgCol - 1) 'Vbc
        asCD(intCellRow - 1, intCellCol + 1) = asCD(intCellRow - 1, giVcgCol - 1) -
            asCD(intCellRow - 1, giVagCol - 1) 'Vca

        'Write Z values (put dummy value in if current is zero
        If (asCD(intCellRow - 1, giIa - 1) <> 0) Then
            asCD(intCellRow - 1, intCellCol + 2) = asCD(intCellRow - 1, giVagCol - 1)
                / asCD(intCellRow - 1, giIa - 1) 'Za
        Else
            asCD(intCellRow - 1, intCellCol + 2) = 1000
        End If

        If (asCD(intCellRow - 1, giIb - 1) <> 0) Then
            asCD(intCellRow - 1, intCellCol + 3) = asCD(intCellRow - 1, giVbgCol - 1)
                / asCD(intCellRow - 1, giIb - 1) 'Zb
        Else
            asCD(intCellRow - 1, intCellCol + 3) = 1000
        End If

        If (asCD(intCellRow - 1, giIc - 1) <> 0) Then
            asCD(intCellRow - 1, intCellCol + 4) = asCD(intCellRow - 1, giVcgCol - 1)
                / asCD(intCellRow - 1, giIc - 1) 'Zc
         Else
            asCD(intCellRow - 1, intCellCol + 4) = 1000
        End If

        'Now write sample to sample delta Z
        If intCellRow > 3 Then
            'To measure a difference we need to have at least be on the second row of
                data
            'Za = (V(n) - V(n-1))/(I(n) - I(n-1))
            If ((asCD(intCellRow - 1, giIa - 1) - asCD(intCellRow - 2, giIa - 1)) <>
                0) Then
                asCD(intCellRow - 1, intCellCol + 5) = (asCD(intCellRow - 1, giVagCol
                    - 1) - asCD(intCellRow - 2, giVagCol - 1)) / (asCD(intCellRow -
                    1, giIa - 1) - asCD(intCellRow - 2, giIa - 1))
            Else
                asCD(intCellRow - 1, intCellCol + 5) = 1000
            End If
            If ((asCD(intCellRow - 1, giIb - 1) - asCD(intCellRow - 2, giIb - 1)) <>
                0) Then
                asCD(intCellRow - 1, intCellCol + 6) = (asCD(intCellRow - 1, giVbgCol
                    - 1) - asCD(intCellRow - 2, giVbgCol - 1)) / (asCD(intCellRow -
                    1, giIb - 1) - asCD(intCellRow - 2, giIb - 1))
            Else
                asCD(intCellRow - 1, intCellCol + 6) = 1000
            End If
            If ((asCD(intCellRow - 1, giIc - 1) - asCD(intCellRow - 2, giIc - 1)) <>
                0) Then
                asCD(intCellRow - 1, intCellCol + 7) = (asCD(intCellRow - 1, giVcgCol
                    - 1) - asCD(intCellRow - 2, giVcgCol - 1)) / (asCD(intCellRow -
                    1, giIc - 1) - asCD(intCellRow - 2, giIc - 1))
            Else
                asCD(intCellRow - 1, intCellCol + 7) = 1000
            End If
        End If
    End If

    'Save this column count for later
    iMaxCol = intCellCol + 8    '+1 since start with zero, +1 since Vca column 1
        greater than intcellcol

    'Finished processing digital values, skip to next row
    intCellCol = 1
    intCellRow = intCellRow + 1
```

```
        If (intCellRow Mod 500 = 0) Then
            displayStatusForm "... parsed " & CStr(intCellRow) & " records (out of " &
                Worksheets("CFG-Decode").Cells(48, 2).value & ")"
        End If

    End If

    DoEvents    'provide time to process interrupt service routines
    If gintCancelFlag = 1 Then  'cancel button pressed?
        Update ".dat file processing cancelled by user"
        bDATIssueFound = True
        Exit Do
    End If

Loop
Close intFileNum
'Check to see if intCellRow matches number of samples from .cfg file
If intCellRow - 3 <> frmStart.lblSamples.caption Then
    'Problem: write message to log file and set error flag
    Update ("Mismatch between number of samples found (" & intCellRow & ") and number
        specified in .cfg file (" & frmStart.lblSamples.caption & ")")
    bDATIssueFound = True
End If
displayStatusForm "... parsed " & CStr(intCellRow) & " records (out of " & Worksheets("
    CFG-Decode").Cells(48, 2).value & ")"

'Copy array variable asCD() to COMTRADE Data worksheet
'Found that for this Resize statement was the fastest method of writing data stored
'in an array to a sheet
Worksheets("COMTRADE Data").Cells(1, 1).Resize(intCellRow, iMaxCol) = asCD

'Change the format of the abs_time column to Excel time format
Sheets("COMTRADE Data").Activate
'Locate the abs_time column
istartCol = giNumDigital + giNumAnalog + 3  'this is its column

'Determine the number of records in the .dat file by reading the answer from the
'decoded data read from the .cfg file (and stored in the CFG-Decode sheet)
lendRow = Worksheets("CFG-Decode").Cells(48, 2).value + 2   'this is the last row

ActiveSheet.Range(Cells(3, istartCol), Cells(lendRow, istartCol)).NumberFormat = "h:mm:ss
    .000"

Update "Completed parsing " + gstrFilename  'write to Log sheet
hideStatusForm
bCompleteDATParse = True

'Display a final pop up depending on whether the conversion process was interrupted by
    the user or not.
If gintCancelFlag = 1 Then
    frmParseInterrupt.Show
    bCompleteDATParse = False
Else
    frmComplete.Show
    bCompleteDATParse = True
End If

Set objsheet = Nothing

'The next few lines deal with setting up the Graphing sheet to show the names of the
'available data.
'Once the data is parsed, write the available channels (C2 - AH2) to R3 and to C12
Worksheets("COMTRADE Data").Range("C2:AH2").Copy

'Write the names as available x-axis values
Worksheets("Graphing").Range("t3").PasteSpecial (xlPasteValues), Transpose:=True

'Write the names as available pen names
```

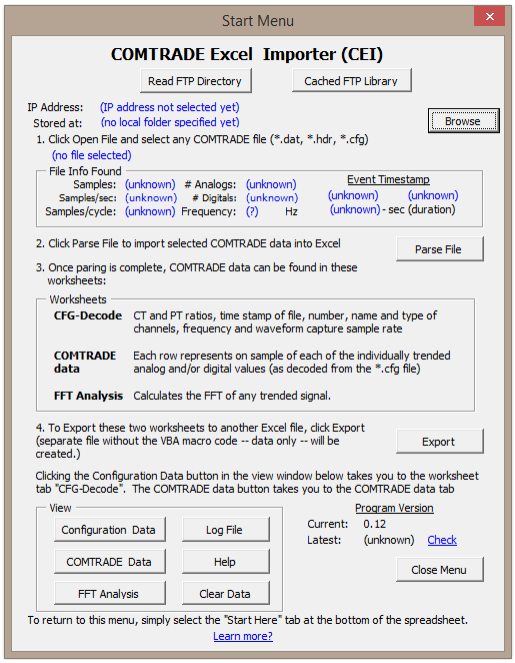

Figure 94: COMTRADE Excel Importer opening menu

```
        Worksheets("Graphing").Range("C12").PasteSpecial (xlPasteValues), Transpose:=True

        'Determine column numbers for time values (abs time and/or rel time)
        findTimes

    Else
        Update ("Invalid or unavailable COMTRADE files. File not parsed")
        hideStatusForm
        frmInvalid.Show
    End If

End Sub
```

B.3.3 Other techniques:

Many other technique were necessary to create a usable tool that could manipulate graphical output (e.g. zoom, pan, separate scaling, offsetting, etc.). Figures 94 and 95 are example screenshots of the program in operation. The interested reader is encouraged to follow this referenced link [58] to download the complete Excel application and experiment on their own. The web site is updated as new version of the program are released, but previous versions can also be downloaded.

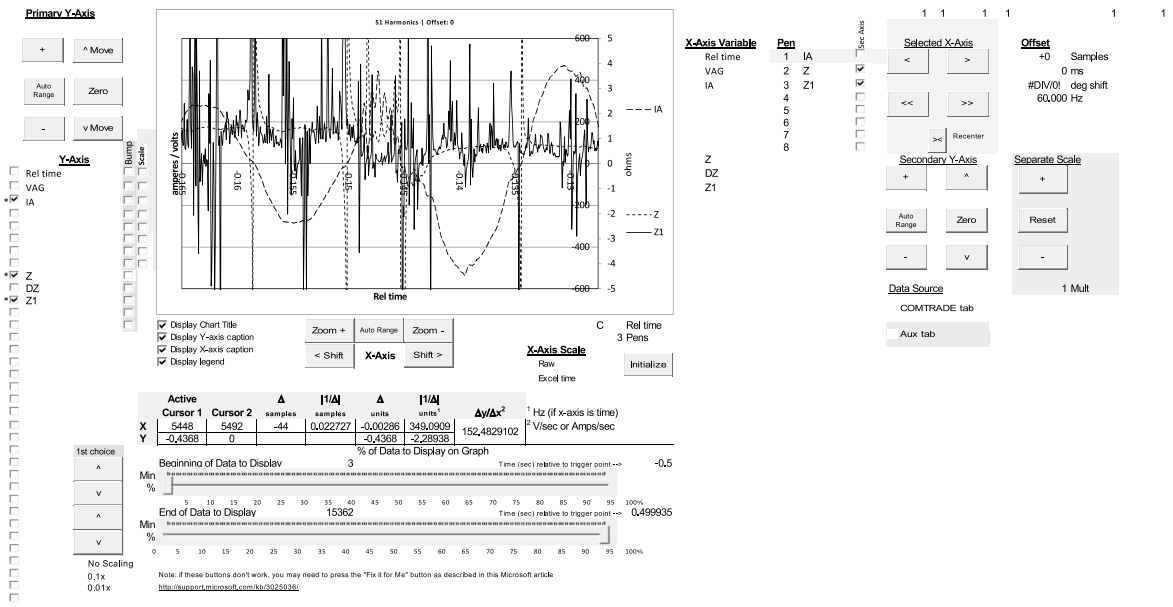

Figure 95: COMTRADE Excel Importer graphing manipulation and measurement screen

As of the date of this document, the most recent version (V0.13a) includes the ability to append multiple COMTRADE captures into one long waveform. This was useful since while the PXM meters used to capture much of the data used in this research only allowed 1 second captures, it could be programmed to re-trigger at the end of sample to capture another 1 second sample. This process could continue until an arbitrary limit was reached, but capture files of 15 or more seconds of 30 kHz sampled data could be captured and combined into one file.

B.3.4 Coding Practices

While documenting the algorithm will help users write COMTRADE decoding routines on their own, as the author was writing these algorithms, it became obvious that other issues were important too if a program was going to operate successfully. Due to the size of these files (half a million rows for a COMTRADE file sampling at 30 kHz over 16 seconds, with each row having 20 or more columns) it is important to include a word about coding technique used to write these particular programs – Visual Basic for Applications (VBA) found inside Excel.

B.3.4.1 Optimizing for Speed

One technique is to switch off all background processing. This technique is documented at a Microsoft blog ([72]). I found that this was necessary to allow the program to operate at anywhere near acceptable update rates.

Being an interpreted language, VBA code does not operate at the same speed as a compiled program, even a compiled Visual Basic program. One solution for increasing speed is to compile those portions of the code that require the most time. Microsoft offers compilers for C# and Visual Basic, with both able to create a VSTO (Visual Studio Tools for Office) add-in [64].

B.3.4.2 Eliminate Need for Plug-In

As the reality of program hijacking (embedded viruses, worms, Trojans, etc.), computers used in corporate environments are being locked by IT departments. Users no longer have administrator rights and therefore, cannot install programs. That said, a method of greatly increasing the speed of the COMTRADE parsing routines is to take that code (open_dat) and compile it, then link it using a add-in using listed above. So the relatively slow processing speed of this program (~30 seconds needed to import a 1.2 MB COMTRADE file with 20 variables and 30720 samples for each variable on 2010 vintage laptop) is a function of the interpreted language used.

BIBLIOGRAPHY

[1] IEEE recommended practice for electric power distribution for industrial plants (IEEE Red Book). *IEEE Std 141-1993*, pages 1–768, April 1994.

[2] Ieee recommended practice for electric systems in health care facilities. *IEEE Std 602-1996 [The White Book]*, pages 1–446, Jan 1997.

[3] IEEE recommended practice for industrial and commercial power systems analysis (IEEE Brown Book). *IEEE Std 399-1997*, pages 1–488, Aug 1998.

[4] IEEE recommended practice for protection and coordination of industrial and commercial power systems (IEEE Buff Book). *IEEE Std 242-2001 (Revision of IEEE Std 242-1986) [IEEE Buff Book]*, pages 1–710, Dec 2001.

[5] IEEE standard profile for use of IEEE 1588 Precision Time Protocol in power system applications. *IEEE Std C37.238-2011*, pages 1–66, July 2011.

[6] IEEE / IEC measuring relays and protection equipment part 24: Common format for transient data exchange (comtrade) for power systems. *IEEE Std C37.111-2013 (IEC 60255-24 Edition 2.0 2013-04)*, pages 1–73, April 2013.

[7] *NFPA 70 - National Electrical Code*. National Fire Protection Association, 2014.

[8] Underwriters Laboratories. 2015. ul.com.

[9] MM Al-Asadi, AP Duffy, AJ Willis, K Hodge, and TM Benson. A simple formula for calculating the frequency-dependent resistance of a round wire. *Microwave and Optical Technology Letters*, 19(2):84–87, 1998.

[10] M Sanjeev Arulampalam, Simon Maskell, Neil Gordon, and Tim Clapp. A tutorial on particle filters for online nonlinear/non-gaussian bayesian tracking. *Signal Processing, IEEE Transactions on*, 50(2):174–188, 2002.

[11] National Fire Protection Association. *NFPA 70 - National Electrical Code*. National Fire Protection Association, 2014 edition, 2014.

[12] National Fire Protection Association and National Fire Protection Association. Technical Committee on Electrical Safety Requirements for Employee Workplaces. *NFPA 70E: Standard for Electrical Safety in the Workplace*. NFPA, 2004.

[13] ATIS. Synchronization Interface Standard, ANSI/ATIS-0900101.2013 (formerly T1.101-1999), 2013.

[14] Kola Venkataramana Babu, Manoj Tripathy, and Asheesh K Singh. Recent techniques used in transmission line protection: a review. *International Journal of Engineering, Science and Technology*, 3(3), 2011.

[15] Sklar Bernard. Digital communications fundamentals and applications. *Prentice Hall, USA*, 2001.

[16] Holy Bible. New international version. *Grand Rapids: Zondervan*, 1984.

[17] Cem Bila. Power system dynamic state estimation and load modeling. *Northeastern University*, 2013. Masters theses.

[18] E.A. Blood, M.D. Ilic, and B.H. Krogh. A kalman filter approach to quasi-static state estimation in electric power systems. In *Power Symposium, 2006. NAPS 2006. 38th North American*, pages 417–422, Sept 2006.

[19] JW Brown, SP Nowlen, and FJ Wyant. High energy arcing fault fires in switchgear equipment, a literature review, 2009.

[20] Wei Chen, OP Malik, Xianggen Yin, Deshu Chen, and Zhe Zhang. Study of wavelet-based ultra high speed directional transmission line protection. *Power Delivery, IEEE Transactions on*, 18(4):1134–1139, 2003.

[21] RE Cuthrell and DW Tipping. Electric contacts. ii. mechanics of closure for gold contacts. *Journal of Applied Physics*, 44(10):4360–4365, 1973.

[22] Thomas Dalstein and Bernd Kulicke. Neural network approach to fault classification for high speed protective relaying. *Power Delivery, IEEE Transactions on*, 10(2):1002–1011, 1995.

[23] TM Dauphinee and H Preston-Thomas. A copper resistance temperature scale. *Review of scientific instruments*, 25(9):884–886, 1954.

[24] A.S. Debs and R. E Larson. A dynamic estimtor for tracking the state of a power system. *IEEE Transactions on Power*, PAS-89(7):1670–1678, Sept-Oct 1970.

[25] David L Dickmander. Methods and apparatus for detection of fault direction, August 18 1998. US Patent 5,796,259.

[26] Eaton. *Consulting Application Guide - Medium Voltage Switchgear - Power Distribution and Control Assemblies*. Eaton, October 2011. Pages V3-T7-2.

[27] Schneider Electric. Technical specification for remote racking system for medium voltage switchgear / specification number: 26 01 10.14. http://static.schneider-electric.us/docs/csi-specifications/26%2001%2010.14.doc.pdf.

[28] M Engelhardt. LTSpice IV. *Linear Technology Corporation, Sept*, 2011.

[29] Bilgin Esme. Kalman filter for dummies, 2009. http://bilgin.esme.org/BitsBytes/KalmanFilterforDummies.aspx.

[30] Donald G Fink and H Wayne Beaty. *Standard handbook for electrical engineers*. McGraw-Hill, 1987.

[31] Janos Gertler. *Fault detection and diagnosis in engineering systems*. CRC press, 1998.

[32] Hans Glavitsch and Michael Vitins. Method for locating a fault on a line near to a measuring location with the aid of substitute signals, December 13 1977. US Patent 4,063,166.

[33] Nimmersjo Gunnar. Arrangement for detecting the direction of a fault from a measuring point, April 15 1975. US Patent 3,878,460.

[34] Ronald E Helmick, Dale W Blair, Scott Hoffman, et al. Fixed-interval smoothing for markovian switching systems. *Information Theory, IEEE Transactions on*, 41(6):1845–1855, 1995.

[35] IEEE. Arc flash research project. 2015. https://standards.ieee.org/about/arcflash/.

[36] Electrical Safety Foundation International. Nonfatal electrical injuries involving days away from work, private industry, by event, 1992-2010, January 2015.

[37] Joe-Air Jiang, Ching-Shan Chen, and Chih-Wen Liu. A new protection scheme for fault detection, direction discrimination, classification, and location in transmission lines. *Power Delivery, IEEE Transactions on*, 18(1):34–42, 2003.

[38] Allan T Johns. Methods and apparatus for fault detection, September 28 1982. US Patent 4,352,137.

[39] Rudolph Emil Kalman. A new approach to linear filtering and prediction problems. *Journal of Fluids Engineering*, 82(1):35–45, 1960.

[40] Christopher D Karlgaard, Roger E Beck, Brett R Starr, Stephen D Derry, Jay M Brandon, and Aaron D Olds. Ares IX best estimated trajectory analysis and results. *JANNAF Paper*, 1961.

[41] Steven Kay. *Intuitive probability and random processes using MATLAB®*. Springer Science & Business Media, 2006. pp. 513-514.

[42] M Kezunović, Igor Rikalo, and DJ Šobajić. High-speed fault detection and classification with neural nets. *Electric Power Systems Research*, 34(2):109–116, 1995.

[43] Genshiro Kitagawa and Will Gersch. *Smoothness priors analysis of time series*, volume 116. Springer Science & Business Media, 2012.

[44] Lindsay Kleeman. Understanding and applying Kalman filtering. In *Proceedings of the Second Workshop on Perceptive Systems, Curtin University of Technology, Perth Western Australia (25-26 January 1996)*, 1996.

[45] V. Kounev, D. Tipper, A.A. Yavuz, B.M. Grainger, and G.F. Reed. A secure communication architecture for distributed microgrid control. *Smart Grid, IEEE Transactions on*, 6(5):2484–2492, Sept 2015.

[46] Underwriters Laboratories. Ul489 molded-case circuit breakers, molded-case switches, and circuit-breaker enclosures. *Underwriters Laboratories*, 1980. http://ulstandards.ul.com/standard/?id=489.

[47] Underwriters Laboratories. Ul1558 standard for metal-enclosed low-voltage power circuit breaker switchgear. *Underwriters Laboratories*, 1999. http://ulstandards.ul.com/standard/?id=1558.

[48] Underwriters Laboratories. Ul891 switchboards. *Underwriters Laboratories*, 2007. http://ulstandards.ul.com/standard/?id=891.

[49] Underwriters Laboratories. Ul 1449 standard for surge protective devices. *Underwriters Laboratories*, September 2009. http://ulstandards.ul.com/standard/?id=1449.

[50] Underwriters Laboratories. UL/IEC low-voltage switchgear and controlgear - part 7-1: Ancillary equipment - terminal blocks for copper conductors. *Underwriters Laboratories*, 2009. https://webstore.iec.ch/publication/4005 http://ulstandards.ul.com/standard/?id=60947-7-1.

[51] Underwriters Laboratories. Ul1066 standard for low-voltage ac and dc power circuit breakers used in enclosures. *Underwriters Laboratories*, 2012. http://ulstandards.ul.com/standard/?id=1066.

[52] Bhagawandas Pannalal Lathi. Signals, systems and communication. 1965.

[53] R. Lee. The other electrical hazard: electrical arc blast burns. *IEEE Transactions on Industry Applications*, 1A-18(3):246, May/June 1982.

[54] R Lee and J. R. Dunki-Jacobs. Pressures developed by arcs. *IEEE Transactions on Industry Applications*, 1A-23:760–764, 1987.

[55] Reiner Lichtenecker. Terrestrial time signal dissemination. *Real-Time Systems*, 12(1):41–61, 1997.

[56] David R Lide. *CRC handbook of chemistry and physics*. CRC press, 2004.

[57] D. Loucks. Calculating incident energy released with varying ground fault magnitudes on solidly grounded systems. *IEEE Transactions on Industry Applications*, 46(2):761–769, 2010.

[58] D. G. Loucks. Excel IEEE COMTRADE file importer, 2015. http://pps2.com/smf/index.php/topic,27.0.html.

[59] David G Loucks. Method and apparatus for measuring impedance across pressure joints in a power distribution system, April 25 2006. US Patent 7,034,554.

[60] K.E. Martin, G. Benmouyal, M.G. Adamiak, M. Begovic, A. Cobb, J.A. Kusters, S.H. Horowitz, G.L. Michel, R.J. Murphy, A.G. Phadke, M.S. Sachdev, and J.S. Thorp. Ieee standard for synchrophasors for power systems. *Power Delivery, IEEE Transactions on*, 13(1):73–77, Jan 1998.

[61] Peter Matisko and Vladimir Havlena. Optimality tests and adaptive kalman filter. In *System Identification*, volume 16, pages 1523–1528, 2012.

[62] A. D. McNaught and A. Wilkinson. Compendium of chemical terminology, 2nd ed. (the "gold book"). *IUPAC*, 1997. XML on-line corrected version: http://goldbook.iupac.org (2006-) created by M. Nic, J. Jirat, B. Kosata; updates compiled by A. Jenkins. ISBN 0-9678550-9-8.

[63] Microsoft. Excel vba reference. Online, 2013. https://msdn.microsoft.com/en-us/library/office/ee861528.aspx.

[64] Microsoft. Walkthrough: Calling code in a vsto add-in from vba, 2015. https://msdn.microsoft.com/en-us/library/bb608614.aspx.

[65] D.L. Mills. Internet time synchronization: the network time protocol. *Communications, IEEE Transactions on*, 39(10):1482–1493, Oct 1991.

[66] Shigeki Minegishi, Hiroshi Echigo, and Risaburo Sato. Frequency spectra of the arc current due to opening electric contracts in air. *Electromagnetic Compatibility, IEEE Transactions on*, 31(4):342–345, 1989.

[67] Luis Montalvo, Gäel Macé, Claude Chapel, Serge Defrance, Thierry Tapie, and Jean Le Roux. Implementation of a tv studio based on ethernet and the ip protocol stack. In *Broadband Multimedia Systems and Broadcasting, 2009. BMSB'09. IEEE International Symposium on*, pages 1–7. IEEE, 2009.

[68] R Nave. RLC Parallel Circuit - Complex Impedance Method, Feb 2008. http://hyperphysics.phy-astr.gsu.edu/hbase/electric/rlcpar.html.

[69] NEMA. Nema standard ab 4-2001 guidelines for inspection and preventive maintenance of molded case circuit breakers used in commercial and industrial applications, 2002.

[70] Gunnar Nimmersjo. Method and device for determining the direction to a fault on a power transmission line, November 5 1996. US Patent 5,572,138.

[71] Alan V Oppenheim, Ronald W Schafer, John R Buck, et al. *Discrete-time signal processing*, volume 2. Prentice-hall Englewood Cliffs, 1989. pp. 201-210.

[72] Diego Oppenheimer. Excel vba performance coding best practices. Online, March 2009. https://blogs.office.com/2009/03/12/excel-vba-performance-coding-best-practices/.

[73] T.S. Perraju, S.P. Rana, and S.P. Sarkar. Specifying fault tolerance in mission critical systems. In *High-Assurance Systems Engineering Workshop, 1996. Proceedings., IEEE*, pages 24–31, Oct 1996.

[74] AG Phadke, JA Jodice, MG Adamiak, JD Brandt, JA Bright, RO Burnett Jr, CH Castro, TW Cease, DM Clark, and G Clough. Comtrade; a new standard for common format for transient data exchange. *IEEE Transactions on Power Delivery (Institute of Electrical and Electronics Engineers);(United States)*, 7(4), 1992.

[75] AK Pradhan, A Routray, and S Madhan Gudipalli. Fault direction estimation in radial distribution system using phase change in sequence current. *Power Delivery, IEEE Transactions on*, 22(4):2065–2071, 2007.

[76] Stephen Roberts. Lecture notes: Signal processing and filter design. Online, 2006. http://www.robots.ox.ac.uk/~sjrob/Teaching/SP/l6.pdf, other lectures available http://www.robots.ox.ac.uk/~sjrob/Teaching/B14_SP/sigproc.pdf.

[77] Alireza Rouhani. Robust dynamic state estimator accounting for load changes. *Master of Science Thesis, Northeastern University*, 2014.

[78] B Don Russell, B Michael Aucoin, and Carl L Benner. Arc burst pattern analysis fault detection system, August 19 1997. US Patent 5,659,453.

[79] Edmund O Schweitzer Jr. Direction indicating fault indicators, June 15 1993. US Patent 5,220,311.

[80] Cyber Sciences. Technical Note: Overview of DCF77 Time Protocol. http://www.cyber-sciences.com/documents/TN-103_DCF77.pdf.

[81] John J Shea, John Bindas, et al. Measuring molded case circuit breaker resistance. *Components, Hybrids, and Manufacturing Technology, IEEE Transactions on*, 16(2):196–202, 1993.

[82] Peter M Shearer. *Introduction to seismology*. Cambridge University Press, 2009.

[83] Kuang-Rong Shih and Shyh-Jier Huang. Application of a robust algorithm for dynamic state estimation of a power system. *Power Systems, IEEE Transactions on*, 17(1):141–147, 2002.

[84] TS Sidhu, H Singh, and MS Sachdev. Design, implementation and testing of an artificial neural network based fault direction discriminator for protecting transmission lines. *Power Delivery, IEEE Transactions on*, 10(2):697–706, 1995.

[85] Paul G Slade. *Electrical contacts: principles and applications*. CRC Press, 2013.

[86] IEEE Industry Applications Society. *1584-2002 - IEEE Guide for Performing Arc Flash Hazard Calculations*. IEEE, 2002.

[87] Michel Souillard. Method and apparatus for determining the direction of a fault on a power transmission line, February 17 1981. US Patent 4,251,766.

[88] Petre Stoica and Randolph L Moses. *Spectral analysis of signals*. Pearson/Prentice Hall Upper Saddle River, NJ, 2005.

[89] Michael Vitins. Method and apparatus for fault and/or fault direction detection, September 1 1981. US Patent 4,287,547.

[90] Mitsuru Yamaura. Method and system for identifying the direction of a fault in a power line, May 27 1986. US Patent 4,591,992.

[91] Eric R Ziegel. Bayesian forecasting and dynamic models. *Technometrics*, 39(4):433, 1997.